EFFECT OF HOT EXTRUSION, ANNEALING AND WARM ROLLING ON THE FUNCTIONAL FATIGUE BEHAVIORS OF NITIHF HIGH TEMPERATURE SHAPE MEMORY ALLOYS

SICAK EKSTRÜZYON, TAVLAMA VE SICAK HADDELEMENİN NITIHF YÜKSEK SICAKLIK ŞEKİL HAFIZALI ALAŞIMLARIN FONKSİYONEL YORULMA DAVRANIŞLARI ÜZERİNDEKİ ETKİSİ

ERHAN AKIN

PROF. DR. BENAT KOÇKAR

Supervisor

Submitted to

Graduate School of Science and Engineering of Hacettepe University

as a Partial Fulfillment to the Requirements

for the Award of the Degree of Doctor of Philosophy

in Mechanical Engineering

2023

To my family:

my mother Melike Akın, my father Yaşar Akın,

my wife Begüm Görgülü Akın

and

my little daughter Ecem Akın

ABSTRACT

EFFECT OF HOT EXTRUSION, ANNEALING AND WARM ROLLING ON THE FUNCTIONAL FATIGUE BEHAVIORS OF NITIHF HIGH TEMPERATURE SHAPE MEMORY ALLOYS

Erhan AKIN

Doctor of Philosophy, Department of Mechanical Engineering

Supervisor: Prof. Dr. Benat KOÇKAR

January 2023, 130 pages

High temperature shape memory alloys (HTSMAs) have a wide range of application in aerospace, automotive and petroleum industries as high temperature actuators. NiTiHf HTSMAs are the most potential alloys compared to the other HTSMAs due to being cost friendly, having very high transformation temperatures and their ability to show high work output. Since exposure time of the alloy to high temperatures is dictated by heating-cooling rate of thermo-mechanical cycling, clarifying the effect of this rate to the functional fatigue life and the stability of the shape memory properties with the number of thermal cycles is crucial to offer a solution for enhancing these properties. The time spent at high temperatures may lead to observe higher plastic deformation since the strength of the metal alloys decreases and dislocation formation during phase transformation becomes easier. The cyclic instability of shape memory behaviors such as the shift of transformation temperatures, the increase or decrease of thermal hysteresis, actuation and accumulated irrecoverable strains stemming from lattice incompatibility between low temperature and high temperature phases and the phase transformation induced dislocations is also a substantial problem, which needs to tackle

with. Besides the precipitation and deformation strengthening treatments that are conducted to increase the strength of these alloys, medium temperature rolling operation is another possible thermo-mechanical processing method in equiatomic NiTiHf alloys since they are known as hard-to-deform materials and precipitation formation is not possible in these materials.

In the light of the information presented above, the aims of the present study can be summarized as to characterize the actuation fatigue properties till failure and the effect of heating-cooling rate during thermal cycling to the actuation/functional fatigue life and the shape memory properties with the number of cycles. Moreover, enhancing the cyclic stability of the alloy by increasing the critical shear stress for slip and decreasing the plastic deformation during phase transformation under stress for equiatomic $Ni_{50}Ti_{30}Hf_{20}$ (at.%) HTSMAs are among the desired aims of this study as well.

Actuation fatigue behaviors of the hot extruded material, the influences of annealing heat treatment and warm rolling at different temperatures on the thermal cycling stability and functional fatigue properties of the equiatomic $Ni_{50}Ti_{30}Hf_{20}$ (at.%) HTSMAs were revealed in the present study. First of all, thermal cycling under constant stress experiments were performed on the randomly selected samples from the hot extruded billet with different heating and cooling rates such as 5, 10, 15, 20 and 25°C/s. Not only the different rates but also the same rates displayed variation in the shape memory properties and fatigue lives. For instance, the specimens tested with 15°C/s rate exhibited 580, 754 and 1738 thermal fatigue cycles under 200 MPa constant stress level via heating the samples to an identical upper cycle temperature. Temperature distribution through the length of the test samples during heating-cooling cycles were analyzed and almost similar temperature gradient was observed for the different rates. To investigate the reason of the discrepancy in the shape memory properties, six fatigue test specimens were cut along the cross section of another virgin piece of the hot extruded billet and enumerated for futher fatigue experiments. Additionally, edges through the gage sections of the enumerated samples were ground and in order to mitigate the surface roughness and micro surface cracks for test standardization. The 15°C/s heating-cooling rate was utilized on all enumerated and edge ground samples

during functional fatigue experiments as an average rate. Even though the actuation fatigue life were increased to almost 8500 thermal cycles for hot extruded samples after edge grinding, the discrepancy in the shape memory behaviors were still oberved. This different behavior was attributed to microstructural nonuniformity and deformation variation induced by hot extrusion process. Annealing heat treatment at 550°C-3h was utilized following hot extrusion on the samples obtained from different regions of bulk material in order to overcome deformation variation problem. The similar transformation temperatures, thermal hysteresis, actuation and irrecoverable strains magnitudes were observed for both of the annealed samples due to relieving the internal stress and removing the microstructural nonuniformity via annealing treatment. More importantly, the stable transformation temperatures were measured and actuation fatigue life time was reached to about 12000 cycles. To increase thermal cycling stability, warm rolling at 600°C and 700°C with 5% thickness reduction were conducted on hot extruded-annealed alloy. The stability of all shape memory properties with the increase in the number of cycles was almost attained with the warm rolling at 600°C process, however, less fatigue lives were obtained for both warm rolled samples compared to annealed ones due to possible microcrack formations, which were induced during rolling operations.

Keywords: High temperature shape memory alloys, NiTiHf, hot extrusion, annealing, warm rolling, functional fatigue

ÖZET

SICAK EKSTRÜZYON, TAVLAMA VE SICAK HADDELEMENİN NITIHF YÜKSEK SICAKLIK ŞEKİL HAFIZALI ALAŞIMLARIN FONKSİYONEL YORULMA DAVRANIŞLARI ÜZERİNDEKİ ETKİSİ

Erhan AKIN

Doktora, Makina Mühendisliği Bölümü

Tez Danışmanı: Prof. Dr. Benat Koçkar

OCAK 2023, 130 sayfa

Yüksek sıcaklık şekil hafızalı alaşımlar (YSŞHA'lar) havacılık, otomotiv ve petrol sanayisinde yüksek sıcaklık aktüatörü olarak geniş kapsamlı uygulamalara sahiptir. NiTiHf YSŞHA'lar uygun fiyatlı olmasından, çok yüksek dönüşüm sıcaklıklarına sahip olmasından ve yüksek iş çıktısı gösterme kabiliyetlerinden dolayı diğer YSŞHA'lara kıyasla kullanım potansiyelleri en fazla olan alaşımlardır. Alaşımın yüksek sıcaklıklara maruz kalma süresi termomekanik çevrimin ısıtma-soğutma hızı tarafından belirlendiği için, bu hızın artan termal çevrim sayısı ile fonksiyonel yorulma ömrü ve şekil hafıza özelliklerine etkisinin açıklanması bu özelliklerin geliştirilmesine bir çözüm sunulması için çok önemlidir. Metal alaşımlarının dayanımı azalacağı ve faz dönüşümü sırasında dislokasyon oluşumu kolaylaşacağı için yüksek sıcaklıklarda geçirilen süre daha yüksek kalıcı şekil değişimi görülmesine öncülük edebilir. Düşük sıcaklık ve yüksek sıcaklık fazları arasındaki kafes uyuşmazlığından ve faz dönüşümüyle endüklenmiş dislokasyonlardan kaynaklanan dönüşüm sıcaklıklarının değişimi, thermal histerezis, aktivasyon ve birikimli geri kazanılamayan gerinimlerin artması veya azalması gibi

şekil hafıza özelliklerinin çevrim kararsızlığı üstesinden gelinmesi gereken önemli bir sorundur. Bu alaşımların dayanımının arttırılması için uygulanan çökelimli ve deformasyonla dayanım arttırma işlemlerinin yanı sıra, deforme edilmesi zor malzemeler olarak bilindikleri ve bu alaşımlarda çökelti oluşumu mümkün olmadığı için orta sıcaklık haddeleme işlemi eşit atomlu NiTiHf alaşımlardaki bir diğer olası termomekanik proses metodudur.

Yukarıda sunulan bu bilgiler göz önüne alınarak, bu çalışmanın amaçları, kırılmaya kadarki aktivasyon yorulma özelliklerinin ve termal çevrim boyunca ısıtma-soğutma hızının aktivasyon/fonksiyonel yorulma ömrüne ve artan çevrim sayısı ile şekil hafıza özelliklerine etkisinin karakterize edilmesi olarak özetlenebilir. Ayrıca, eşit atomlu $Ni_{50}Ti_{30}Hf_{20}$ (at.%) YSŞHA'lar için kayma için kritik kayma gerilmesi arttırılarak ve stress altındaki faz dönüşümü sırasındaki kalıcı deformasyon azaltılarak bu alaşımın çevrim kararlılığının arttırılması da bu çalışmanın arzu edilen amaçları arasındadır.

Bu çalışmada, sıcak ekstrüde malzemenin aktivasyon yorulma davranışları, tavlama ısıl işleminin ve farklı sıcaklıklardaki sıcak haddelemenin eşit atomlu $Ni_{50}Ti_{30}Hf_{20}$ (at.%) YSŞHA'ların termal çevrim kararlılığı ve fonsiyonel yorulma özellikleri üzerindeki etkileri gösterildi. İlk olarak, sıcak ektrüde çubuktan rastgele seçilmiş numunelerde 5, 10, 15, 20 and 25°C/sn gibi farklı ısıtma-soğutma hızlarında sabit gerilim altında termal çevrimler gerşekleştirildi. Sadece farklı hızlarda değil aynı hızlarda da şekil hafıza özelliklerinde ve yorulma ömürlerinde farklılık sergiledi. Örnek olarak, 200 MPa sabit gerilim seviyesi altında aynı en yüksek çevrim sıcaklığına ısıtılarak 15°C/sn hız ile test edilen numuneler 580, 754 ve 1738 termal yorulma çevrimleri gösterdi. Isıtma-soğutma çevrimleri sırasında test numunesinin ölçüm açıklığı boyunca sıcaklık dağılımı analiz edildi ve farklı hızlar için hemen hemen aynı sıcaklık gradyanı gözlemlendi. Şekil hafıza özelliklerindeki farklılığın sebebini araştırmak için, sıcak ekstrüze çubukğun işlem görmemiş bir diğer parçasından kesit alanı boyunca altı yorulma test numunesi kesildi ve ileriki yorulma testleri için numaralandırıldı. Ek olarak, test standardizasyonu için mikro yüzey çatlaklarının ve yüzey pürüzlülüğünün azaltılması için numaralandırılmış numunelerin ölçüm açıklığı boyuncaki kenarları zımparalandı. Kenarları zımparalanmış ve numaralandırılmış tüm numunelerin fonksiyonel yorulma

testlerinde ortalama hız olarak 15°C/sn ısıtma-soğutma hızı uygulandı. Kenar zımparalamadan sonra sıcak ekstrüze edilmiş numuneler için aktivasyon yorulma ömrü yaklaşık 8500 termal çevrime arttırılmasına rağmen, hala şekil hafıza davranışlarındaki farklılık gözlemlendi. Bu farklı davranış sıcak ekstrüzyon işlemi tarafından indüklenen mikro yapısal faklılık ve deformasyon varyasyonuna dayandırıldı. Deformasyon varyasyon sorununun ortadan kaldırılması için sıcak ekstrüze edilmiş kaba malzemenin farklı bölgelerinden elde edilen numunelere 550°C'de 3 saat tavlama ısıl işlemi uygulandı. Tavlama işlemi ile iç gerilimin düşürülmesi ve mikro yapısal farklılığın ortadan kaldırılmasından dolayı her iki tavlanmış numune için benzer dönüşüm sıcaklıkları, termal histerezis, aktivasyon ve geri kazanılamayan gerinim değerleri gözlemlendi. Daha da önemlisi, sabit dönüşüm sıcaklıkları ölçüldü ve aktivasyon yorulma ömrü yaklaşık 12000 çevrime ulaştı. Termal çevrim kararlılığını arttırmak için, sıcak ektrüde edimiş-tavlanmış alaşıma 600°C'de ve 700°C'de %5 kalınlık azalması ile sıcak haddeleme uygulandı. 600°C sıcak haddeleme işlemi ile artan çevrim sayısındaki tüm şekil hafıza özelliklerinin kararlılığı hemen hemen elde edildi ama haddeleme işlemi sırasında indüklenen olası mikro çatlak yapılarından dolayı tavlanmış numunelere kıyasla her iki sıcak haddelenmiş numune için de daha az yorulma ömrü elde edildi.

Anahtar Kelimeler: Yüksek sıcaklık şekil hafızalı alaşımlar, NiTiHf, sıcak ekstrüzyon, tavlama, sıcak haddeleme, fonksiyonel yorulma

ACKNOWLEDGEMENTS

First and foremost, I would like to thank my advisor Prof. Dr. Benat Koçkar for her encouragement, guidance and support throughout my graduate course and research. I would like to express my gratitude for having the opportunity to work with you, your trust and patience for the present study.

I am also grateful to Prof. Dr. Arcan Dericioğlu and Prof. Dr. Bora Maviş for serving my committee, offering valuable suggestions and contribution throughout the study. Additionally, I would like to thank to jury members Prof. Dr. Kadri Aydınol and Assist. Prof. Mehmet Nurullah Balcı for their precious contribution and comments.

I am thankful to my labmates Oğulcan Akgül, Meriç Ekiciler, Halil Onat Tuğrul, Hasan Hüseyin Saygılı and Günce Dugan for their valuable friendship, support and useful discussions.

I would like to thank Turkish Aerospace Industries and Defence Industry Agency for their support under the project no: DKTM/2015/10.

Lastly, I would like to thank to my parents, lovely wife and daughter for their never ending patience and believe in me during this study. I would like to dedicate this study to my wife and my dear daughter, Ecem Akın, who will be my motivation and support all my life.

Erhan AKIN

January 2023, Ankara

TABLE OF CONTENTS

LIST OF FIGURES

LIST OF TABLES

SYMBOLS AND ABBREVIATIONS

Symbols

Au	Gold
Cd	Cadmium
Cu	Copper
Fe	Iron
Hf	Hafnium
Ni	Nickel
Pd	Palladium
Pt	Platinum
Ti	Titanium
Zr	Zirconium
ΔH	Transformation Enthalpy
ΔT	Thermal Hysteresis
ε_{act}	Actuation Strain
$\varepsilon_{austenite}$	Accumulated Irrecoverable Strain

Abbreviations

A_f	Austenite Finish Temperature
A_s	Austenite Start Temperature
DSC	Differential Scanning Calorimeter
ECAE	Equal Channel Angular Extrusion

EDS	Energy Dispersive X-ray Spectrometry
H/C	Heating/Cooling
HTSMA	High Temperature Shape Memory Alloy
M_f	Martensite Finish Temperature
M_s	Martensite Start Temperature
SE	Superelasticity
SEM	Scanning Electron Microscopy
SMA	Shape Memory Alloy
SME	Shape Memory Effect
TT	Transformation Temperature
UCT	Upper Cycle Temperature
WEDM	Wire Electrical Discharge Machining
WR	Warm Rolled

1. INTRODUCTION

1.1. Motivation

Shape memory alloys (SMAs) with the capability to recover shape changes upon heating by reversible martensitic phase transformation can be offered as an alternative for heavy-weight actuators which were used in aerospace, automotive and medical industries [1–3]. NiTi-based SMAs are the most studied alloys owing to good mechanical and SM properties, dimensional stability and corrosion resistivity. Nevertheless, the transformation temperatures (TTs) of binary NiTi alloys are below 100°C, and hence, this restricts their use in energy, automotive and aerospace industries at which the thermoelastic martensitic transformation should take place at the temperatures higher than 100°C [4,5]. Ternary alloying with Au, Pd, Pt, Zr and Hf is the most promising way to enhance the TTs and SM properties of these alloys. Hf addition is the most reasonable method due to having relatively lower initial material cost than that of Au, Pt and Pd and being more effective to increase transformation temperatures than that of Zr and Pd addition. Moreover, Hf addition leads better dimensional stability and ductility than those of Zr addition since Zr makes NiTi alloys so brittle due to its high oxygen affinity [4,6–9].

Ni-rich NiTiHf alloys were the most commonly studied HTSMAs in the literature due to the ability of formation nano-scale Ni-rich precipitates via appropriate heat treatments that enhance the stability of thermal and mechanical cycling of phase transformation [9–12]. These precipitates strengthen the material via precipitation hardening mechanism and increase TTs due to decrease of the Nickel content in the matrix. It has been also shown by Karaca et.al [11] that aging treatment at 550°C-3h of $Ni_{50.3}Ti_{29.7}Hf_{20}$ (at.%) HTSMA leads the formation of nanosize coherent precipitates, which provide optimum cyclic stability and highest TTs. Nevertheless, the TTs of the aged Ni-rich NiTiHf alloys are still less than that of equiatomic and relatively high Hf content NiTiHf alloys [13–17]. The influence of Ni and Hf contents of NiTiHf alloys on the TTs has been recently investigated by Umale et.al. [18]. Martensitic transformation

temperatures increase with more than 10at.% of Hf addition and reach to about 500°C with 30 at.%Hf. TTs are not influenced by the alteration of Ni content for less than 50 at.%Ni, however, they are so sensitive to Ni amount and drop below 0°C if the Ni content is higher than 50at%. Thus, equiatomic NiTiHf HTSMAs having high Hf content can be a good candidate for HT applications due to their high TTs.

HTSMAs can be used as solid state actuators to reduce the weight or size of actuators via replacing the hydraulic and pneumatic systems in airplanes and helicopters. A very substantial application of HTSMAs was published by Boeing that these alloys were utilized to decrease the noise and vibration on a jet engine [19]. Additionally, HTSMAs can endure high number of thermomechanical cycles for actuator applications, and structural and functional fatigue mechanisms are the primary failure reasons in these applications upon mechanical or thermo-mechanical cyclic loading of the materials [20]. Structural fatigue takes place upon cyclic loading of the material with the crack initiation due to increasing dislocation density and crack propagation until failure. However, functional fatigue occurs in SMAs due to the thermal cycling under constant stress of the alloys till the loss of shape memory effect or failure. TTs alter and actuation and accumulated irrecoverable stains decrease and increase, respectively, with the increase in the heating-cooling (H/C) cycle numbers during functional fatigue tests. Since stable actuation fatigue behaviors and long fatigue lifetimes are substantial for HT application, it is also necessary to improve the stability of thermal cyclic and functional fatigue properties of NiTiHf alloys. The functional fatigue behavior of SMAs is affected by the experiment conditions (service conditions), stress amplitudes, chemical compositions, applied heat treatments and surface roughness of the samples [21–26].

Additionally, Karakoc et. al. [13] investigated the influence of upper cycle temperature (UCT) on the functional fatigue behavior of nano-precipitation strengthened Ni-rich $Ni_{50.3}Ti_{29.7}Hf_{20}$ alloy. Actuation fatigue tests were performed under various constant stress values for 300°C - 350°C UCTs and it was observed that the fatigue life declined with increasing UCT under the same applied stress magnitude. The effect of chemical compositional and microstructural alteration of four batches of Nickel-rich NiTiHf alloy have been also examined recently [27]. The martensitic TTs and actuation fatigue

properties have been susceptible to a little change in the Nickel content and amount of inclusions from batch to batch variation of the alloy. The high cycle actuation fatigue lifetimes of the hot extruded and aging treated at 550°C for 3h Ni-rich NiTiHf alloy were analyzed by our research group. It was indicated that aging heat treatment improved the thermal cycling stability and increased the fatigue life more than 3 times [14].

In this study, hot extrusion following casting of the bulk material was utilized to homogenize the chemistry and the structure of the as-cast bulk material. It is known that different plastic deformation magnitudes are applied during extrusion process from surface to inner sections of the bulk material which lead to obtain deformation variation [28]. The temperature levels can be also different throughout the cross section during hot extrusion process which induces microstructural nonuniformity and flow lines [29–32]. The effect of microstructural nonuniformity upon the mechanical and fatigue properties throughout cross section of high strength aluminium alloys were studied by Ocenasek et al. [33]. They represented that coarse recrystallized layers on surface region and non-recrystallized structure in the inner section were observed after extrusion process. Non-recrystallized structure led to observe higher ultimate strength, fatigue lives and less ductility than that of recrystallized surface layers.

The machining process of NiTi-based alloys via conventional machining methods is a substantial problem because these alloys are classified as hard-to-deform and machine materials. Since wire electrical discharge machining (WEDM) has advantageous for the machining operations of high strength materials, it is generally conducted to cut these materials. However, surface integrity of WED machined samples noticeably influences fatigue performance of materials. The fatigue lifetimes and surface integrity relationship in binary NiTi alloys was studied by Liu et al. [26]. It was shown that the finish trim cut created negligible white layers and less surface roughness compared to the rough machined cut, and the finish cut provided almost 48% higher fatigue lifetime. Hence, it can be stated that the fatigue performance of the samples are highly effected by the surface integrity of WEDMed NiTi based SMAs.

Generally, annealing heat treatment at intermediate temperatures improves ductility and decreases strength of the metal alloys due to annihilation of dislocations. Nevertheless, there are some studies in the literature showing that annealing treatment can improve mechanical properties of alloys via annihilation of mobile dislocations and thermally rearrangement of remnant dislocations [34,35]. The annealing treatment induced hardening effect on ultrafine grained NiMo alloys was studied by Gubicza et.al. [35]. It was seen that the strengthening was obtained after annealing due to decrease in the mobile dislocation density via annihilation and rearrangement of the remaining defects into low energy configurations.

Moreover, the effect of H/C rate of thermal cyclic experiments on martensitic phase transformation behavior was rarely investigated in the literature [16,36,37]. The differential scanning calorimetry (DSC) and isobaric thermal cyclic tests were performed with various cooling rates on NiTiHf HTSMA [16]. It was shown that the TTs and thermal hysteresis were not susceptible to the alteration in the cooling-rate, however, increasing transformation enthalpy (ΔH) behavior was observed with increasing rate which was attributed to higher measuring precision at higher rates. The recoverable strain magnitudes during isobaric thermal cycling tests were not influenced by alteration on the cooling rates. It is also worth to mention that there has not been any study analyzing the effect of H/C rate on the actuation fatigue behavior of HTSMAs in the literature yet.

Thermal cyclic stability can be improved by enhancing the critical shear stress (CSS) for dislocation slip, and hence, the remnant martensite and plastic strain upon martensitic phase transformation decrease. It can be obtained via hardening methods such as precipitation strengthening, grain size refinement, texture formation and work hardening [6,24,38]. Among all these hardening methods, strain hardening by rolling is the simplest strengthening method to enhance the SM and mechanical responses of equiatomic NiTiHf HTSMAs. Babacan et.al. [15] analized the influence of cold-rolling (CR) following annealing heat treatment and warm-rolling (WR) at different temperatures on the SM properties of the equiatomic NiTiHf alloy. They observed that the rolling operation improved dimensional stability during thermal cycling experiments

and decreased defect generation upon martensitic transformation. The functional fatigue tests were utilized on extruded, CRed with post-annealed samples and the WRed sample in this study for only 100 cycles. The actuation fatigue response of equiatomic NiTiHf alloy until failure has not been studied yet in the literature up to now.

1.2. Objectives

In the view of the given information, one of the main aims of the this thesis is to reveal the actuation fatigue properties of the equiatomic $Ni_{50}Ti_{30}Hf_{20}$ (at.%) HTSMA up to failure and to obtain enhanced functional fatigue and thermal cyclic stability for the high temperature applications. Even though there have been many work on the influence of aging heat treatment on Ni-rich NiTiHf alloys, there has not been any study representing the full actuation fatigue life of $Ni_{50}Ti_{30}Hf_{20}$ (at.%) alloy. It has been already shown that increasing UCT decreases the fatigue life of the alloy for the same applied stress magnitude [13]. Since the material is exposed to higher temperatures for longer times during thermal cycles with lower heating/cooling (H/C) rates, the H/C rate may affect the SM properties and actuation fatigue life of the alloy. Hence, another goal of the present study is to evaluate the effect of heating and cooling rate during thermal cyclic under constant stress experiments on the properties and fatigue life.

The objectives of the first part of the present study can be summarized as;

- Investigate the full functional fatigue properties of the equiatomic $Ni_{50}Ti_{30}Hf_{20}$ (at.%) HTSMA such as TTs, thermal hysteresis, actuation and accumulated irrecoverable strains.
- Determine the optimum heating and cooling rate during the constant stress thermal cyclic tests with considering the limitations of the custom-made functional fatigue test setup.
- Investigate the repeatability of the functional fatigue experiments to be able to observe how consistent the actuation fatigue properties and functional fatigue lives of the alloys that have the same thermal and mechanical processing history and under the same testing parameters.

However, different shape memory properties and functional fatigue lives were observed when the samples were thermally cycled under the same stress magnitudes with the same heating-cooling rates and the study evolved and focused to clarify and rule out the reasons of this discrepancy. The goals of this section can be summed up as;

- Analyze elemental distribution, heat treatment and surface roughness of the test samples, which may influence the SM properties, cyclic stability and functional fatigue lives of the alloys.
- Identify the influence of the hot extrusion process on the microstructural evolution of the alloy which effects the SM properties and actuation fatigue life. The different regions of the bulk material are exposed to different plastic strains and temperature variation through the cross section of the billet may be possible during the hot extrusion process. The identification of the effect of hot extrusion process on the actuation fatigue properties of the samples obtained from the different regions of the bulk material became significant.
- Eliminate the induced stresses and microstructural variations due to hot extrusion and hence to obtain consistent behavior from extruded samples via applying a specific heat treatment.
- Standardize the surface conditions of the test samples to obtain consistent results.
- Enhance the thermal cycling stability and fatigue life of the alloy via heat treatment and characterize the influence of this treatment to microstructural evolution and SM properties of the alloy.
- Standardize the testing conditions via analyzing the temperature distribution through the gage length of the test sample during thermal cycling to clarify the heating homogeneity of the custom-made actuation fatigue test setup.

Since the martensitic phase transformation is experienced at HTs, the strength of these alloys decreases and plastic deformation becomes inevitable during martensite-austenite boundary movement which leads to a dimensional instability and early failure in heating-cooling cycles under constant stress. In order to overcome this problem,

deformation-hardening treatments via rolling are applied to equiatomic NiTi based SMAs. The objectives of the last section can be specified as;

- Identify the influence of warm rolling by changing rolling temperature to the structure of the alloy (microcrack formation after rolling processes).
- Investigate the effect of rolling on the stability of the TTs and the thermal hysteresis values, actuation and accumulated irrecoverable strains evolution with the cycle numbers under constant stress.

To be able to attain these objectives, the equiatomic $Ni_{50}Ti_{30}Hf_{20}$ (at.%) HTSMA was obtained as in hot extruded condition. Then, a comprehensive organized study was conducted to determine actuation fatigue properties up to failure for this alloy and to investigate the effect of H/C rate, annealing heat treatment and warm rolling operations on the SM properties, cycling stability, repeatability and functional fatigue life of equiatomic NiTiHf alloy.

2. BACKGROUND

2.1. Theory

Shape memory alloys display a unique property that depends on reversible thermoelastic phase transformation. After deforming the alloy at low temperature and in the low symmetry phase, it remembers the initial shape upon heating above critical temperature via transforming to high symmetry phase. Low temperature & low symmetry and high temperature & high symmetry phases are called as Martensite and Austenite, respectively. The martensitic transformation is a first order solid-to-solid phase transformation that occurs without diffusion, and atoms exhibit cooperative movement via shear-like mechanism [39]. The transformation can be seen schematically in Figure 2.1-1. The high temp. phase, austenite, usually has cubic structure and the low temp. phase, martensite, has lower symmetry and generally displays B19 or B19' superlattice structure. If the material is cooled down to martensite start (M_s) temperature, forward transformation starts by a shear-like mechanism and many variants can be formed from the same parent phase due to lower symmetry of martensite [39,40]. When the material is heated above austenite start (A_s) temperature, martensite becomes unstable and reverse transformation starts. The martensite reverts back to austenite with the original orientation if it is crystallographically reversible. Despite the fact that the atomic displacements are small compared to inter-atomic distance, martensitic transformation creates macroscopic shape change.

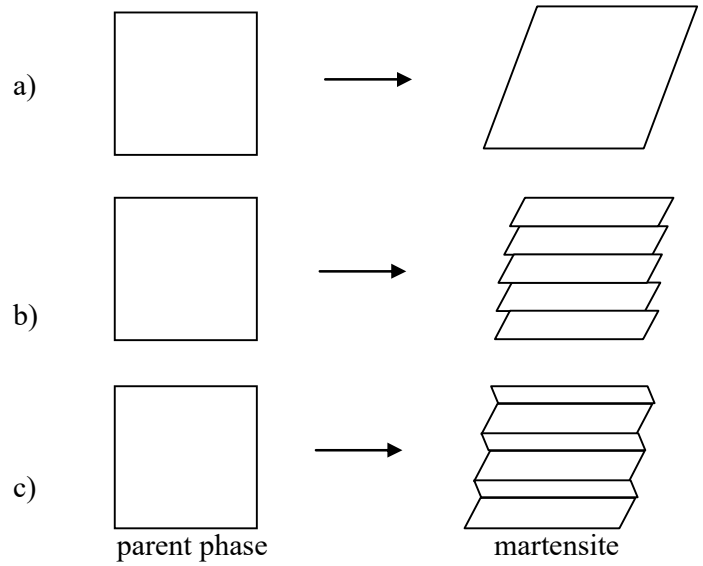

Figure 2.1-1. Schematic illustration of lattice invariant shear requiring upon martensitic transformation; (a) shape change by martensitic transformation, (b) accommodation of strain via slip, and (c) strain accommodation upon twinning [39].

Martensitic transformation creates shape change as exhibited in Figure 2.1-1.a and a large strain is induced around the martensite structure in the parent phase. The strain, which is created in the nucleation and growth processes, can be accommodated either by slip or twinning as presented in Figure 2.1-1.b and Fig. 2.1-1.c, respectively. Both processes do not change the crystal structure of martensite, so these are described as lattice invariant shear (LIS). It depends on the alloy to introduce slip or twinning, but strain is relieved with the twinning formation in shape memory alloys. The martensites in different regions have the same crystal structure but their orientations are different and twin related as shown in the Figure 2.1-1.c. They are called as the correspondence variants of the martensite [39–41].

The martensitic phase transformations are not related to compositional change, so the Gibbs free energy curves for parent and martensite phases can be represented as in Figure 2.1-2. G^m and G^p symbolize the Gibbs free energy of martensite and parent phases, respectively and T_0 symbolizes the thermodynamic equilibrium temperature at which the phase transformation takes place theoretically. The driving force for the nucleation of martensite can be written as [39]:

$$\Delta G^{p\rightarrow m}|M_s = G^m - G^P \quad (2.1.1)$$

and a Gibbs free energy change of a system for martensitic transformation may be written as [39]:

$$\Delta G = \Delta G_c + \Delta G_s + \Delta G_e = \Delta G_c + \Delta G_{nc} \quad (2.1.2)$$

Where ΔG_c represents the chemical energy change between parent and martensite phases, ΔG_s represents the surface energy which is relevant to frictional energy needed for the propogation of the interface between parent and martensite phases, ΔG_e represents the elastic energy around the martensite, and also ΔG_{nc} is the non-chemical energy which is the summation of surface energy and elastic energy. The non-chemical free energy is not zero due to the frictional energy that appears during phase boundary movement, so supercooling of ΔT_s is required for the nucleation of a martensite and superheating is also required for the reverse transformation as shown in Fig. 2.1-2. Similarly, due to the elastic energy around martensite and the friction at the martensite-austenite boundary overcooling is necessary to complete the martensite transformation, so martensite start and finish temperatures are not the same.

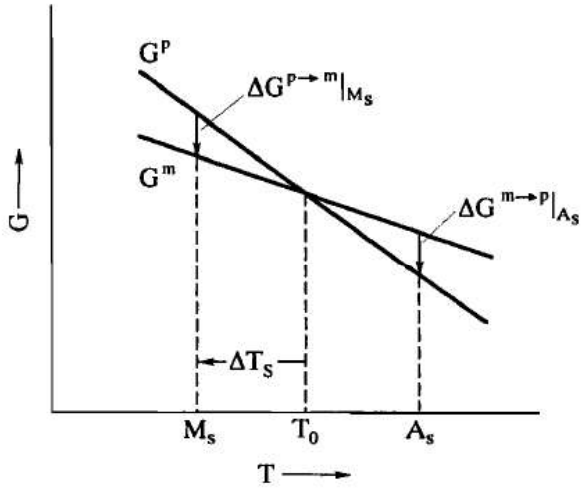

Figure 2.1-2. Schematic illustration of Gibbs free energy curves for both martensite and parent phases, and their relation to the martensite start and austenite start temperatures [39].

Martensitic transformations may be classified as thermoelastic and non-thermoelastic. In the thermoelastic transformation, small thermal hysteresis is observed as shown for the Au-Cd alloy in Figure 2.1-3 that means the driving force for the phase transformation is very small and the austenite and martensite interface is very mobile. While the martensite withdraws, the parent phase takes place in the original orientation that means the transformation is crystallographically reversible. However, in the non-thermoelastic transformation as shown for the Fe-Ni alloy in the same figure, large driving force is needed. The parent and martensite interface is immobile that results large frictional energy dissipation and large thermal hysteresis. Additionally, the reverse transformation arises by the re-nucleation of the austenite phase in martensite phase.

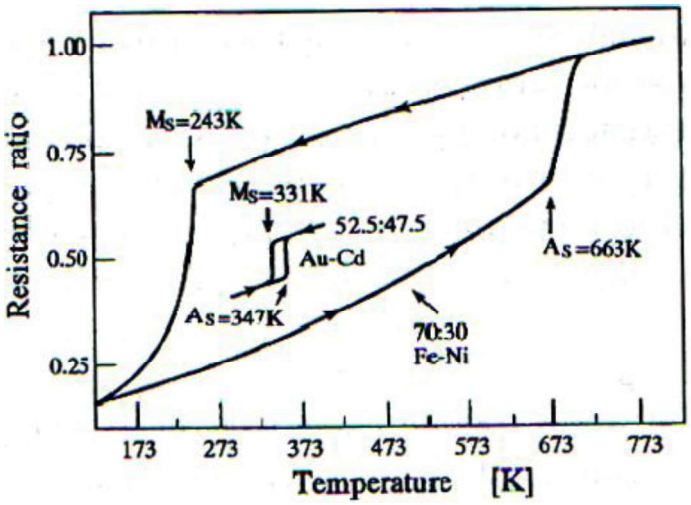

Figure 2.1-3. Electrical resistance vs temperature graphs during thermal cycling of Au-Cd and Fe-Ni alloys for thermoelasic and non-thermoelastic martensitic transformations, respectively [39].

Shape memory effect (SME) and superelasticity (SE) are two different mechanisms which are observed in SMAs and their existence depends on testing temperatures with respect to martensite-austenite transformation temperatures. Thermally induced martensitic transformation occurs in SME and stress induced martensitic (SIM) transformation is observed in SE. When the material is deformed in martensite state at a temperature below austenite start (A_s), it returns to its initial shape by heating it above austenite finish temperature (A_f) and called as SME. If it is cooled down to a temperature lower than martensite finish temperature (M_f) without applying any stress, the shape of the material does not change due to self accommodation of martensite variants to be able to minimize the internal energy alteration. So, this mechanism is also called as one-way SME. The number of martensite variants is determined by crystallographic structure of the phases. For instance, there are 12 correspondence variants for monoclinic B19' martensite and body centered cubic B2 austenite [4]. With applying external stress, energetically more favorable variants are formed at the expense of the others and this is named as detwinning or martensite reorientation. Large amount of external strain is obtained as a consequence of detwinning/reorientation. Since slip is irreversible process, the deformation of martensite takes place via twinning. If the external stress is applied while the alloy is kept in the parent phase, mechanical energy is used as the driving force for the transformation and stress induced/detwinned

martensite is formed with the most favorable single variant. The material transforms back to parent phase after unloading and the shape change is recovered. This effect is called as Superelastic (SE) behavior.

The stress-temperature relation to observe SME and SE behaviors with the critical stress to induce martensite and critical stress for slip can be seen in Figure 2.1-4. SME is observed below austenite start (A_s) by heating up the material above A_f. When the material is loaded and unloaded at a temperature lower than A_s, it can partially return to its initial shape and the full recovery can be achieved via heating above A_f temperature. The recovery of the initial shape via heating is related with SME as mentioned above. If the material is loaded above A_f temperature, SIM transformation occurs above critical stress to induce martensite line. The material returns to austenite phase and regains its original shape after unloading, which is called as SE, because martensite is unstable above A_f temperature in the absence of stress. Since the parent phase is stable at high temperatures, critical stress to induce martensite increases with increasing temperature, which is defined by the Clausius-Clapeyron relationship in the literature. In other words, transformation temperatures of SMAs increases with increasing applied stress level and results a constant $d\sigma/dT$. Both SME and SE happen partially in the temperature region between A_s and A_f temperatures. Since slip is irreversible process, the applied stress must be below critical stress for slip line to be able to obtain SME and SE. To improve shape memory characteristics, it is necessary to increase critical stress for slip via some strengthening methods such as solution hardening, precipitation hardening and work hardening. In addition, above a certain temperature which is known as M_d, slip occurs firstly instead of twinning as a deformation mode in the presence of external stress and stress induced martensitic transformation become impossible. Therefore, the material is initially heated to above A_f temp. and cooled-down just above M_s temp. for SE in applications.

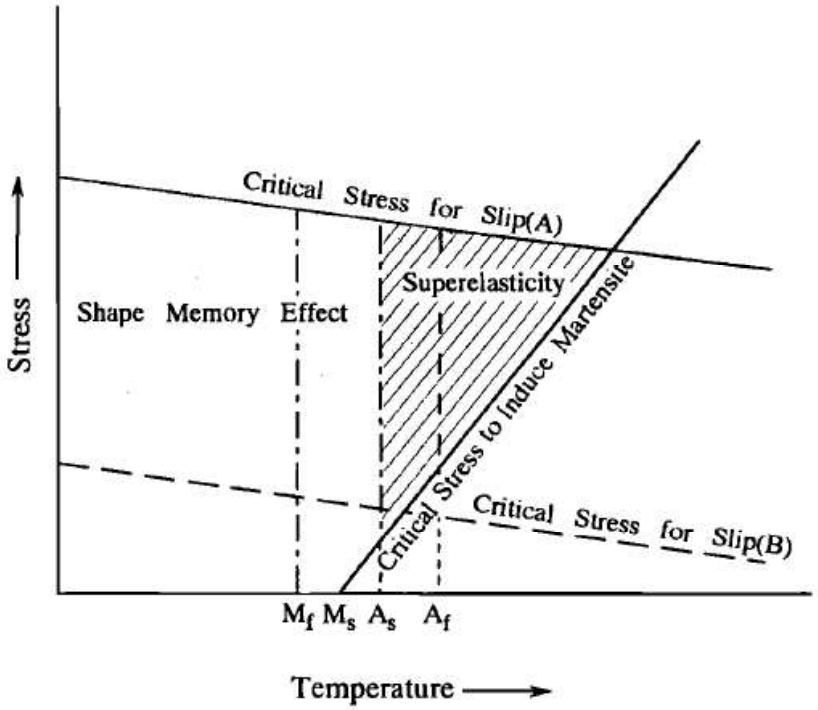

Figure 2.1-4. Schematic representation of shape memory effect and superelasticity regions in stress vs temperature diagram [39].

Figure 2.1-5 represents the SME mechanism by drawing the stress, strain and temperature coordinates. The material has self-accommodated/twinned martensite structure at point A which is below M_f temperature. When the stress is applied, martensite first deforms elastically and then the strain is accommodated by forming the most favorable single variant at the expense of the others, which is called as martensite detwinning/reorientation. With increasing applied stress level, detwinned martensite deforms elastically up to point B. After unloading from B to C, elastic recovery takes place and the material still stays in the reoriented/detwinned structure. If it is heated above A_f temperature, all martensite transforms to austenite and shape change is recovered at point D. As aforementioned above, this is called as SME. When it is cooled down from D to E, self-accommodated martensite is obtained.

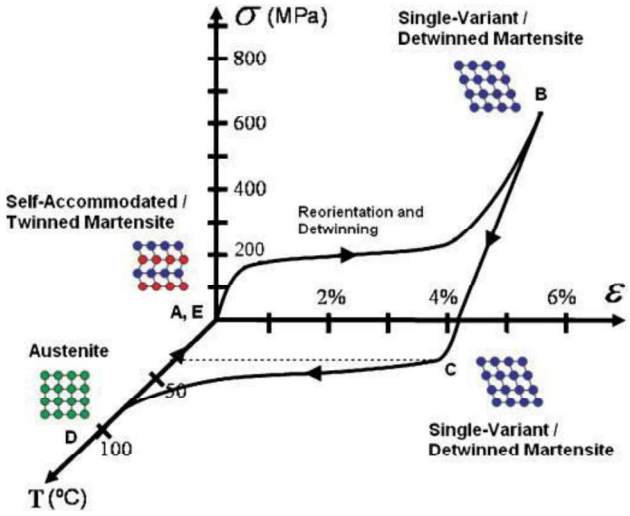

Figure 2.1-5. Demonstration of shape memory effect on stress-strain-temperature diagram [4].

Up to now, the material only recalls the form of austenite phase but the form of martensite phase can be also remembered under certain circumstances. If internal stress is induced by thermal and thermomechanical processing, the certain martensite variants are biased to minimize the internal energy. When the thermal cycle is repeated, the material also recalls the shape of the martensite via cooling and the shape change occurs between forward and reverse transformation without any applied stress. This phenomenon is called as the two-way SME (TWSME). The internal stress fields to bias certain martensite variants instead of self-accomodated martensite are created via dislocations or aligned coherent precipitates. The necessary process for TWSME are; introduction of plastic deformation [42,43], constrained aging [44], thermal cycling [6] and martensite aging [45].

2.2. Shape Memory Alloys

SME was first discovered in Au-47.5 at%Cd alloy in 1951 [46] but it was come into use in applications after finding in Ti-Ni alloys in Naval Ordinance Laboratory, 1963 [47]. After many investigations and developments in this field over the years, SMAs with higher work output values and by means of the ability to recover large deformations via

reversible phase transformation, can be utilized to reduce the required size or weight of actuators in automotive, aerospace and energy exploration industries as energy efficient and light weight alternatives of pneumatic or hydraulic systems nowadays.

The most commercially utilized SMAs are the near-equiatomic binary NiTi and Cu-based ternary alloys. Cu-based SMAs are inexpensive compare to NiTi, and they have been investigated due to their electrical-thermal conductivity advantages and deformation ability. Martensitic transformation occurs from body centered cubic ordered parent phase to a mixture of monoclinic and orthorhombic martensite phases in these alloys [48]. Cu-Zn and Cu-Al based SMAs are the main Cu-based alloys. TTs of the β phase Cu-Zn alloys are far below room temperature [49] while Cu-Al alloys have TTs above 100°C [50]. Therefore, Cu-Al is a potential candidate for HT applications because of their higher TTs and better microstructural stability than that of Cu-Zn. Ternary element addition such as Al, Ga, Si and Sn increases M_s temperature and stabilize the β phase. Among the other alloys, CuZnAl alloys are the most promising owing to better ductility. The optimum Ni concentration is about 3mass%Ni for the CuAlNi ternary alloy because the alloy become brittle with increasing Ni content [51].

Nevertheless, Cu-based SMAs are brittle and suffer from intergranular cracking which limits many potential applications of these alloys. The segregation of impurities at grain boundaries causes intergranular cracking that results from intergranular weakness in these alloys [51]. Due to the ordered structure of the parent phase, CuZnAl alloys have good ductility even in the polycrystalline structure and represent superelasticity even by applying 300 MPa or higher stress levels. The grain boundary fracture is the most serious problem in CuAlNi alloys in application. The formation of SIM throughout the grain boundaries upon quenching creates stress concentrations and causes intergranular cracking [52]. In conclusion, it is still necessary to improve the ductility of these alloys. Even if they can provide shape memory and superleasticity at the temperature range between 100°C and 200ºC, their usage in high temperature applications are desperate.

2.2.1. Binary NiTi

NiTi alloys are the most commonly used ones in many applications and studied by the reason of their great mechanical, SE and SM properties and good corrosion resistance and biocompatibility. The SME and SE occur in near-equiatomic NiTi alloys with thermo-elastic martensitic transformation from B2 cubic crystal structure parent phase to a monoclinic B19' martensitic phase [39,53]. The transformation may also takes place with two steps from B2 structure to R-phase, then from R-phase to B19' [54]. If the material has high internal stress due to thermal cycling or thermo mechanical treatment, two step transformations occur to minimize the energy of the system. Therefore, it transforms from B2-phase to R-phase and then to Martensite instead of transforming from B2 directly to Martensite-phase. R-phase has rhombohedral structure and it is a martensitic transformation, too. The transformation behavior is controlled by Ni content, addition of alloying element, aging and thermo-mechanical treatment.

The phase-diagram of binary Ni-Ti alloy by Massalski [55] and addition of phase equilibrium between the B2 and Ti_3Ni_4 phases by Otsuka and Kakeshita [56] can be seen in Figure 2.2-1. The diagram is crucial for the heat treatment of the alloys to enhance the shape memory characteristics. The solubility on Ti-rich side is vertical with Ti_2Ni second phase that replaces in the grain boundaries in the bulk NiTi alloy. Oxides mostly appear as Ti_4Ni_2O phase having the similar structure with Ti_2Ni in this alloy and deteriorates shape memory characteristics by decreasing fracture strength of the alloy. In Ni-rich side, Ti_3Ni_4 phase appears with aging at relatively lower temp. & shorter time, $TiNi_3$ phases appears at higher aging temp. & longer aging time and Ti_2Ni_3 phase appears at intermediate aging temp. & time. The Ti_3Ni_4 and Ti_2Ni_3 are metastable phases and the final product of decomposition is a mix of $TiNi_3$ and TiNi. To observe SME in NiTi alloys, the alloy should have the composition that stays in the TiNi phase region of the phase diagram.

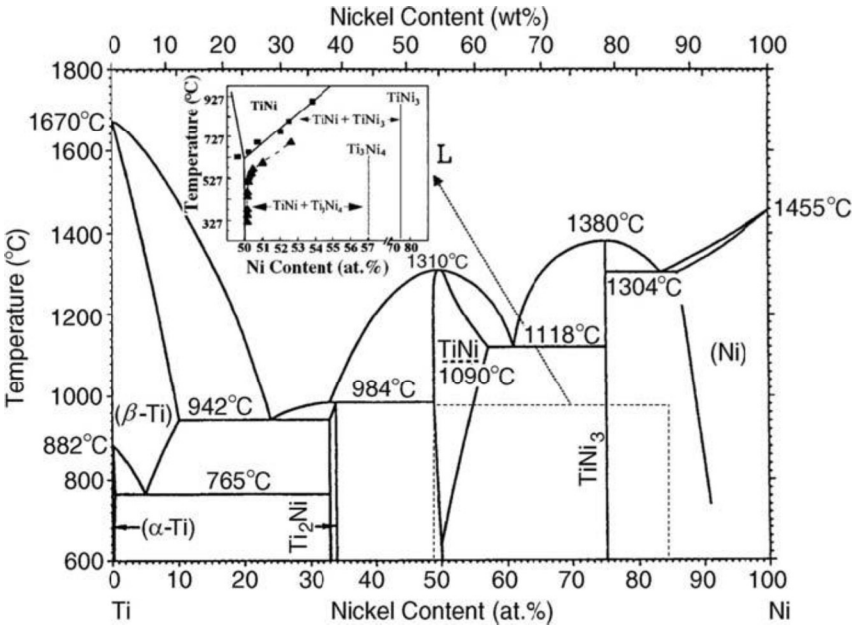

Figure 2.2-1. Phase diagram of a Ni-Ti alloy with addition of phase equilibrium between the B2 and Ti_3Ni_4 phases [55,56].

The transformation temperatures (TTs) of the martensitic transformation from B2 to B19' strongly depends on Ni concentration as shown in Figure 2.2-2 [57]. The TTs on Ti-rich side is almost constant at about 60ºC. However, TTs decrease drastically with increasing Ni concentration on Ni-rich side of the alloy. M_s temperature almost decreases to 0 K for the alloys that have 51.5at.% Ni content or higher. Elastic constant is intensely dependant on composition alteration in martensitic alloys because the alloying affects lattice dynamic parameters substantially. Thus, a small alteration on compositional difference must be compensated by a large alteration on TTs to be able to keep stability of elastic constant [53]. Nevertheless, TTs can be adjusted for these alloys with additional aging heat treatment which leads to create Ni-rich precipitates and decrease Nickel content of the matrix.

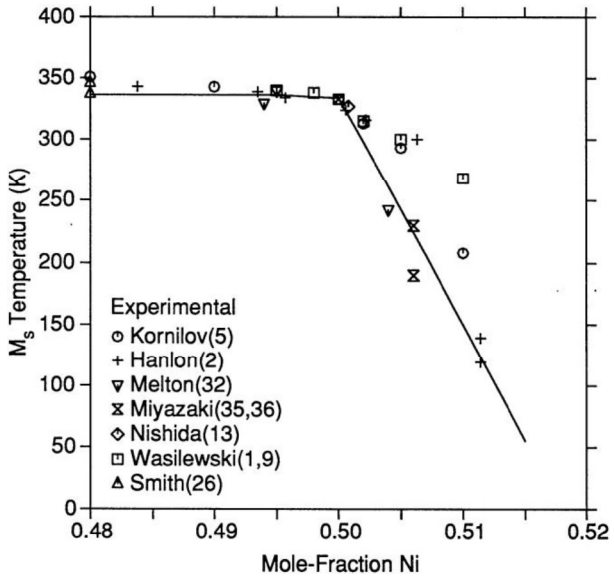

Figure 2.2-2. The relation between the martensite start temperature M_s and Ni-content [57].

Apart from the other phases, the formations of coherent and semi-coherent Ti_3Ni_4 precipitates are important to control martensitic transformation properties of Ni-rich alloys. These precipitates generate coherent stress fields throughout the microstructure that affect martensitic transformation characteristics, increase TTs by depleting Ni-content of the matrix and enhance fatigue life of the alloy via increasing CSS for slip due to precipitation hardening mechanism [58,59]. The coherent Ti_3Ni_4 precipitates also create strain fields in the matrix and lead to observe two-way SME.

Although the binary NiTi alloys have superior SM and mechanical properties and their TTs can be increased by aging heat treatment via obtaining Ni-rich precipitates, TTs are limited to 100°C and it is necessary to increase TTs of SMAs for high temperature applications with some other methods.

2.2.2. High temperature Shape Memory Alloys

The most common SMAs are the binary NiTi alloys due to having good shape memory properties, dimensional stability, workability and ductility as mentioned in section 2.2.1. Nevertheless, the TTs of these alloys are below 100°C and hence their HT applications are restricted [4,5]. Many applications in automotive, energy and aerospace industries require the thermoelastic martensitic transformation to take place above 100°C [4,39]. The most promising way to obtain HTSMAs is the addition of alloying elements which highly affects the TTs and SM properties of binary NiTi alloys. There are various alloying elements such as Au, Pt, Pd, Zr and Hf. The most favorable one is hafnium (Hf) because it is cost friendly, increases martensitic TTs more effectively than that of Zr and Pd, and also provides better dimensional stability and ductility than that of Zr addition to the NiTi alloys [4,6–9,60]. There are also other binary and ternary systems such as NiAl, NiMn, ZrRh, ZrCu, TiPd, TiAu, TaRu and NbRu etc. and these systems are briefly mentioned in the following paragraph.

The binary NiAl HTSMAs exhibit martensitic transformation near the Ni_2Al stoichiometric composition. The alloys suffer from phase instabilities and decomposition, poor tensile ductility and texture [61,62]. Martensitic transformation occurs only for equiatomic NiMn and Mn-rich alloys from B2 parent phase to tetragonal martensite in NiMn alloy. This alloy is exceedingly brittle especially it has Mn-rich composition [63]. Zr-Rh and Zr-Cu are two main Zr-based intermetallic HTSMAs which transform from B2-austenite to monoclinic B19'-martensite [64]. Zr-based alloys suffer from substantial plasticity upon martensitic transformation and exhibit noticeable irrecoverable strain. TiPd and TiAu alloys exhibit SME via martensitic transformation between 400°C and 700°C. Otsuka et al. [65] showed that SM properties of TiPd alloys deteriorate due to a rapid decline in σ_y which leads notable plastic deformation instead of SIM transformation and detwinning. TaRu and NbRu alloys have ultrahigh transformation temperatures above 900ºC-1000°C. The B2 ordered parent phase transforms to a tetragonal martensite at equiatomic composition for both systems [66]. These two alloys are stable and less affected by aging and cyclic effect because the transformation phases are entirely on equilibrium states [67].

As a consequence, the ternary alloying with the addition of Pd, Pt, Zr and Hf to the binary NiTi are the most common HTSMAs and studied in the transformation temperature range of 100ºC - 400 ºC. Pd, Pt and Au have limited commercial applications because of the high cost of the elements. High oxygen affinity of Zr makes the alloy brittle which is undesirable for applications. Hf addition increases TTs more effectively than that of Pd and Zr. These HTSMAs will be discussed in details in the following section.

2.2.2.1. NiTi HTSMAs with addition of Pd, Pt and Zr

In TiNiPd alloys, nickel is replaced with palladium for the alteration of shape memory and mechanical properties. At nearly constant 50 at%Ti concentration, minimum TTs is measured at approximately 10 at% Pd content. TTs increase with increasing Pd content with an increasing rate per at% of 15°C/at% and [68–70]. The parabolic dependence of the TTs on composition comes from the alteration in the martensite structure. The transformation occurs from B2 austenite to orthorhombic B19-martensite on the higher Pd-content side but the B2-austenite transforms to monoclinic B19'-martensite or R-phase when Pd concentration is less than 10at% [68].

The disadvantages of TiNiPd alloys are having low CSS for slip particularly at HTs that results plastic deformation during martensitic phase transformation and poor SM properties. Therefore, different strengthening mechanisms have been utilized on these alloys to enhance shape memory properties such as solid solution strengthening, alloying with a fourth element, thermomechanical treatment and precipitation hardening. Atli et al. [71] studied 0.5 at% scandium addition at the expense of titanium to $Ti_{50.5}Ni_{24.5}Pd_{25}$. It has been shown that the scandium especially improved dimensional stability under repeated thermomechanical cycles. Additionally, irrecoverable strain and thermal hysteresis decreased with Sc addition. The enhancement in the properties was based on the solid solution hardening effect.

The influence of thermo-mechanical treatment on the SM properties of $Ti_{50}Pd_{30}Ni_{20}$ was studied by Golberg et al. [72]. Cold-rolling with 24 – 25% thickness reduction and subsequent annealing treatment at 400°C-1h effectively increased CSS for slip levels of martensite. The optimal post annealing temperature after cold-rolling was proposed as to be higher than A_s but below the recrystallization temperature of the studied alloy. Bigelow et al [73] examined the isobaric thermal cycling responses of five $(Ni,Pd)_{49.5}Ti_{50.5}$ alloys with Pd content changing from 15 to 46 at%. They showed that TTs increase linearly with increasing the Pd concentration in the aforementioned range. Repeated thermal cycling at constant stress magnitude caused a saturation of the transformation strain and insignificant irrecoverable strain under certain conditions, and resulted stable shape memory behavior. The effect of severe plastic deformation on a $Ti_{50.3}Ni_{33.7}Pd_{16}$ alloy was investigated by Kockar et al [7]. They observed that the thermal cyclic stability under constant stress was enhanced by severe plastic deformation and the irrecoverable strain levels decreased after deformation due to increase in CSS for slip via microstructural refinement.

Because of high cost of the material, TiNiPt as well as TiNiAu HTSMAs have been studied less. Higher than 10-15at% of Pt addition at the expense of Ni leads to an increase in TTs and TTs can reach to 1000°C with 50 at%Pt addition. In a similar manner to TiNiPd alloys, the structure of the martensite is monoclinic B19' in the alloys having less than 10at%Pt content and TTs are not susceptible to Pt content alteration. On the other hand, the forward transformation occurs from B2 → B19 orthorhombic martensite for Pt content that is higher than 16at%. [68,74]. The thermal hysteresis is usually less than 20ºC for the alloys that have 25 or less at%Pt. It is worth to mention that small hysteresis is desirable for many applications, however, the thermal hysteresis is larger than 80 ºC in the alloy that contains 30 at%Pt [68]. Noebe et al. [75] examined the constant stress thermal cyclic behavior of the $Ti_{50.5}Ni_{29.5}Pt_{20}$ alloy that were in various forms such as rod and wire. They observed stable shape memory behavior after post-drawing and training, stable TTs upon repeated thermal cycling and narrow thermal hysteresis as on order of 11°C. It was also shown that recovery starts at 450°C and completes at about 600°C while grain growth and recrystallization starts at or near 700°C in this alloy. These alloys are useable for HT applications due to having high TTs, narrow hysteresis, good work output and mechanical properties but further

investigations are necessary for the optimization of the processing parameters and the microstructural improvements.

Since NiTiZr alloys have poor ductility and instable shape memory response, they are the least desired HTSMAs. Zirconium addition at the expense of Ti increases TTs of the alloys that have more than 10 at%Zr [76]. B2 cubic austenite phase transforms to monoclinic B19' martensite in the alloy with 10 at%Zr or less while transformation occurs to orthorhombic B19 martensite when the content of Zr is higher than 15 at% [77]. Pu et al. [77] also showed that the transformation strain decreases with increasing Zr content and NiTiZr alloys exhibit poor cyclic stability during thermal cycling. The thermal cyclic stability of Ni-rich NiTiZr alloys after low temperature aging were studied by Perez-Sierra et al. [78] and the TTs of the alloy considerably changed throughout thermal cycling which was extremely dependent upon initial microstructure. Evirgen et al. [79] investigated the microstructure and SM behaviors of $Ni_{50.3}Ti_{34.7}Zr$ with respect to aging heat treatments by forming nanosized precipitates. It was seen that the size of the precipitates greatly affected the interactions between the martensitic phase transformation and precipitates and thus, the SM properties. They also showed that the fine precipitates obtained by aging heat treatments did not hinder the motion of the martensite variants and resulted larger transformation strain, less thermal hysteresis, dimensional and thermal stability. However, the larger precipitates blocked the variants and restrained the martensitic transformation, and ultimately deteriorated the SM and mechanical properties.

2.2.2.2. NiTiHf High Temperature Shape Memory Alloys

NiTiHf and NiTiZr alloys are being preferred if compared to NiTiPd, NiTiPt and NiTiAu due to having relatively lower material costs of Hf and Zr. The NiTiZr alloys are brittle and have poor cyclic stability, and Hf addition increase TTs more efficiently. Hafnium is added with the expense of Titanium in NiTiHf HTSMA to increase TTs and tailor the SM properties. The martensitic transformation occurs from cubic-B2-austenite → monoclinic-B19'-martensite when the Hf content is less than 15 at.%, however, the martensite structure is orthorhombic B19 in the alloys having more than 15 at%Hf

[80,81]. While the TTs of the alloy is not susceptible to Hf content up to 10 at%Hf, they increase with almost the rate of 20°C/at%Hf when the Hf content is higher than 10 at% and TTs reach to 525°C when the Hf content is 30 at% [4,82–84]. The solubility of Hf in NiTi and NiHf limits the Hf addition to NiTi alloy [44].

In recent study, Umale et.al. [18] studied the effect of compositional changes in wide range on the martensitic transformation characteristics of NiTiHf alloys as shown in Figure 2.2-3.a and b. The TTs can be tailored from -170°C to 500°C by changing the chemical composition which is shown as the largest temperature range. The M_s temperatures initially drop when Ni content is higher but TTs increase significantly with increasing Hf content for all selected alloys when the Hf content is more than 10 at%. They state that the increase in local lattice distortions in conjunction with the redistribution of Ti and Hf is responsible for the initial drop of TTs. These defects hinder martensitic transformation and act as barriers for nucleation and growth of martensite, and so overcooling is needed for transformation and eventually M_s temperature decreases [18]. Nevertheless, Hf addition increases the lattice parameter of the A phase and results overall expansion of the unit cell for the alloys having higher than 10 at%Hf. The local lattice distortions generated by less Hf decrease due to expansion of the unit cell. Since the energy barriers for B2 to B19' transformation decline, TTs increase with increasing Hf content beyond 10 at%Hf [18,85].

As shown in the literature, TTs do not change if the Ni content is less than 50 at% but they decreases drastically down to below 0°C with increasing Ni content when Ni exceeds 50 at% for $Ni_xTi_{90-x}Hf_{10}$ [83]. Additionally, Umale et al. studied M_s temperature variation with Ni content for given Hf contents as seen in Figure 2.2-3.b [18]. The TTs decrease with increasing Ni content when the Ni content exceeds 50 at%Ni for all selected alloys which have different Hf contents. As explained in binary NiTi section, since alloying has significant impact on the lattice parameters, small compositional change creates large variations in TTs to keep stability of elastic constant [53].

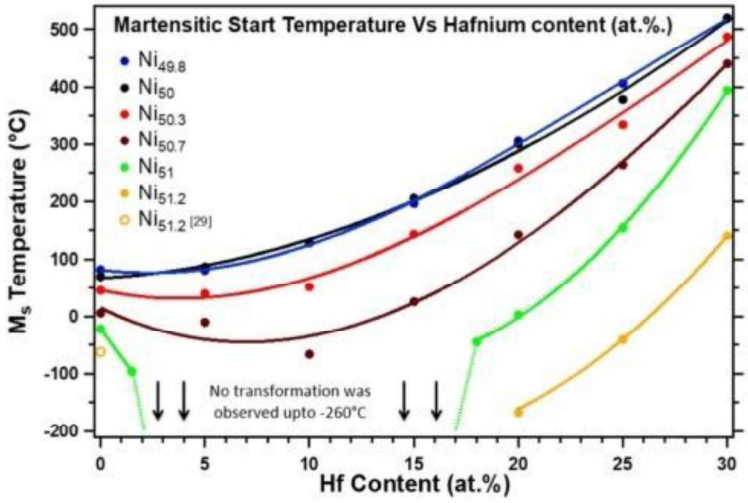

(a)

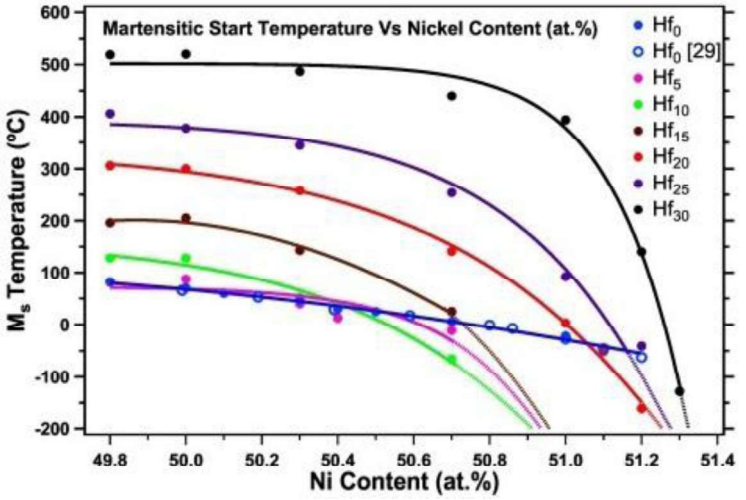

(b)

Figure 2.2-3. M_s temperature variation for different NiTiHf alloys (a) with Hf content for given Ni contents (b) with Ni content for given Hf contents [18].

The Hf addition to NiTi increases the TTs but also brings some disadvantages to these alloys such as poor ductility at room temperature [4,86,87], poor shape memory effect [86,88] and deterioration of thermal and mechanical cyclic upon reversible transformation [4,6,89]. The degradation of thermal cyclic during cyclic loading mostly occurs in Ni-lean NiTiHf alloys due to the decrement in the CSS for slip and the high stress for the reorientation of martensite and detwinning [6,86]. The reported second

phases for Ni-lean NiTiHf alloys are $Ti_2Ni(Hf)$, $HfNi(Ti)$, $(Ti,Hf)_2Ni$, $Hf_2Ni(Ti)$, $Ti_4Ni_2O_x$ ($x<1$) and HfO_2 [18,90–95]. Even the fine $Ti_2Ni(Hf)$ second phases strengthen the matrix and enhance SM & SE properties of the alloy, the size of the second phases is usually large and worsens the strength and properties of the alloys. These precipitates have the responsibilities for observing low transformation strain and high thermal hysteresis (>50°C), poor workability and poor ductility owing to the oxides, and lack of thermal and mechanical cyclic stability.

Solid solution hardening by adding quaternary alloying elements [96–99], strain hardening by severe plastic deformation, cold rolling with post-annealing and hot rolling [6,15,94,95,100–103] and precipitation hardening [8–12,14,104–107] have been studied to improve the SM and mechanical properties of the NiTiHf alloys. Karaca et al. [97] showed the SE behavior with 4.2% recoverable strain in NiTiHfPd alloys in the solutionized condition but they also concluded that the alloys are brittle and failed with limited plastic deformation. The influence of severely plastic deformation by Equal Channel Angular Extrusion (ECAE) process on the thermal cycling response of $Ni_{49.8}Ti_{42.2}Hf_8$ alloy was investigated by Kockar et al. [6]. After ECAE process, the stability of thermal cyclic of the alloy improved via microstructural refinement. Also, higher transformation strains under constant tensile stresses were obtained due to increase in favorable dislocation density which created local internal stress, and less total plastic strain was seen by increasing dislocation density which led to increment in CSS for slip and strengthen the material.

Precipitation hardening is the most promising strengthening mechanism to increase CSS for slip on the Ni-rich alloys. The nano-scale Ni-rich precipitates can be formed by appropriate heat treatments and strengthen the material by acting as barriers to the dislocation motion in the Nickel-rich NiTiHf alloys. The TTs decrease with increasing Nickel content for the alloys that have Ni content higher than 50 at% as explained previously. Nevertheless, it was reported that these nano-scale Ni-rich precipitates increase TTs by decreasing Ni-content of the matrix and also promote cyclic stability and mechanical properties of the alloys [9,10,109,11,12,14,84,105–108]. It was first stated by Meng et al.[104,110] that the second phases in Ni-rich NiTiHf alloys were

$Ni_4(Ti, Hf)_3$ precipitates likewise Ni_4Ti_3 precipitates in binary NiTi alloy. However, it has been later shown that the new precipitate has more complex crystal structure and called as 'H-phase' by Yang et al. [111]. The H-phase has a face-centered orthorhombic crystal structure. The Ni composition of H-phase is slightly higher than that of the nominal composition of Ni-rich alloy, so Nickel content of the matrix depletes and TTs increase via the formation of this phase [84].

The size and interparticle spacing of H-phase precipitates substantially affect the shape memory and superelastic properties. The aging time and temperature are essential to determine the size and interparticle spacing of H-phase. Karaca et al. [11] was examined the extruded and aged $Ni_{50.3}Ti_{29.7}Hf_{20}$ alloys to observe the aging parameters effects on the microstructure and SM properties. Figure 2.2-4 represents the stress free transformation curves for $Ni_{50.3}Ti_{29.7}Hf_{20}$ alloys extruded+aged for 3h at different temperatures [11]. The initial decrease in stress free TTs with aging treatment at 300°C and 400°C is attributed to the stress fields around the very small and finely spaced precipitates. The stress fields around these precipitates suppress martensitic transformation and overcooling is necessary for the transformation, so the TTs decrease. Since the volume fraction of precipitates is low, the stress fields around the precipitates are more effective than that of the compositional effect due to precipitate formation for lower aging temperatures. However, the precipitates grow with aging above 500°C and deplete the Nickel content in the matrix, and eventually TTs increase. The TTs decrease with aging above 650°C due to approaching the solvus temperature which leads to a decrease in volume fraction of precipitates and less Nickel reduction of the matrix.

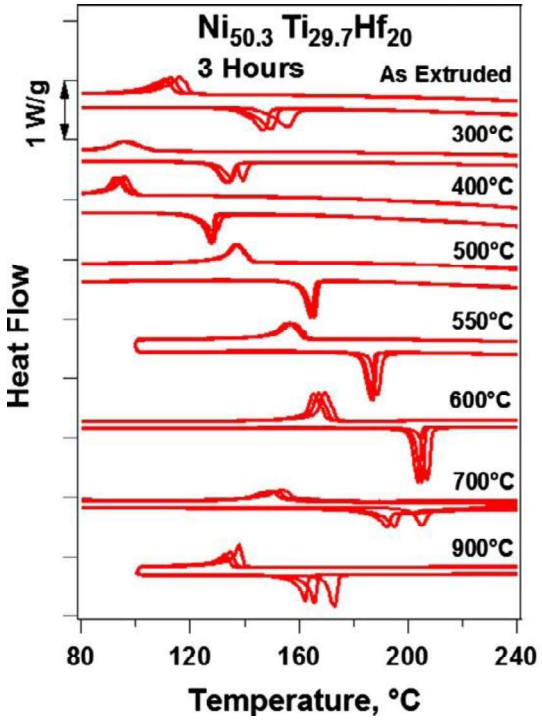

Figure 2.2-4. DSC, stress free transformation, curves for $Ni_{50.3}Ti_{29.7}Hf_{20}$ aged for 3h at different temperatures from 300 to 900°C [11].

Karaca et al. also observed in the same study that the size and interparticle distance of precipitates increased while the aging temperature increased from 500°C to 650°C. Aging at 550°C-3h caused the formation of nanosize, almost 20 nm, coherent precipitates that significantly enhanced mechanical and SM properties of $Ni_{50.3}Ti_{29.7}Hf_{20}$ alloy. Even, if the aging was conducted at 650°C-3h higher TTs can be attained compared to the TTs that were attained by aging at 550°C-3h but the sample showed poor cyclic stability, poor SM and SE behavior due to large sized precipitates as a result of overaging. They concluded that aging of $Ni_{50.3}Ti_{29.7}Hf_{20}$ at 550°C-3h resulted optimum TTs and cyclic stability.

The effect of aging treatment on the microstructure and TTs of a Ni-rich NiTiHf alloy were investigated by Evirgen et al. [9]. Aging at 550°C-3h resulted nanoscale coherent precipitates which increased TTs via diminishing Ni-content in the matrix. The thermal stability was enhanced and thermal hysteresis decreased with strengthening by the precipitation hardening mechanism. Saghaian et al. [112] examined the thermal cyclic

under stress and isothermal stress cyclic in tension mode and it was seen that aging at 550°C for 3h provided the perfect dimensional stability upon stress biased thermal cyclic with a 3.7% recoverable strain under 500 MPa and almost 18.5 Jcm^{-3} work output. The reasonably high TTs, almost perfect dimensional stability and a good work output upon load-biased thermal cycling experiments were observed for $Ni_{50.3}Ti_{29.7}Hf_{20}$ alloy that was aged at 550°C for 3h by Bigelow et al. [10].

Nevertheless, the precipitate formation and higher Nickel composition in Ni-rich alloys lead to brittleness of these alloys and difficulty of cold and warm processing below half of the melting temperature ($<0.5.T_m$). The precipitation characteristically reduces the accomplishable recoverable and superelastic strain levels because of reducing transforming volume. Moreover, equiatomic and relatively high Hf content NiTiHf alloys have still higher TTs than that of aging heat treated Ni-rich NiTiHf alloys [13–17].While the stress free TTs which are M_f,M_s,A_s and A_f of hot extruded and aged at 550°C-3h $Ni_{50.3}Ti_{29.7}Hf_{20}$ alloy are about 100, 141, 136, 169°C, respectively [14] and M_f,M_s,A_s and A_f temperatures of hot extuded and/or annealed at 550°C for 3h $Ni_{50}Ti_{30}Hf_{20}$ alloy are about 236, 282, 286, 330°C, respectively [17]. Since the precipitation strengthening mechanism is only applicable on the Ni-rich side of NiTiHf alloys, it is necessary to carry out other practical strengthening methods rather than precipitation hardening in equiatomic $Ni_{50}(Ti,Hf)_{50}$ alloys to increase CSS for slip and improve SM properties. Babacan et al. [15] investigated the effects of CR and WR on the SM behavior and thermomechanical cycling stability of $Ni_{50}Ti_{30}Hf_{20}$ HTSMA, which will be discussed in detail in the rolling effect section. The hot extruded with subsequent wire drawing of the $Ni_{50}Ti_{35}Hf_{15}$ has been studied via considering phase transformation and deformation response by Canadinc et al. [100]. The phase transformation temperatures decreased, material strength was enhanced and actuation cyclic stability was improved after wire drawing process. The decrease of TTs was attributed to the formation of dislocation substructures and stabilization of austenite phase. The decreased but more stable actuation strain values with the cycle numbers for the wire were associated with the microstructural refinement and possible crystallographic texture. Besides, smaller thermal hysteresis was observed due to the microstructural stabilization via ausforming upon hot extrusion and wire drawing which led to hinder dislocation generation in conjunction with the phase transformation.

2.3. Functional Fatigue on NiTiHf HTSMAs

The hydraulic and pneumatic systems of the essential reconfigurable elements for helicopters and airplanes consist of relatively heavy weight actuators and can be replaced by HTSMAs that can be utilized as solid state actuators. Boeing Researchers published a very significant and specific application of HTSMAs in 2006. These alloys were used to morph the chevrons shape on a jet engine exhaust nozzle to diminish the vibration and noise. These chevrons can operate against load for high cycles and were specifically called as 'Variable Geometry Chevrons' [19]. These alloys can stand a high number of repeated thermomechanical cycles for actuator applications. The major failure mechanisms in actuator applications are structural and functional fatigue upon cyclic loading of the material. Even if the applied stress magnitude is less than the σ_y of the material, it causes plastic deformation upon repeated phase transformation in these kind of applications [20].

Structural fatigue takes place because of cyclic loading with the accumulation of microstructural damages such as the crack initiation by the increase in the dislocation amount and crack propagation is observed up to fatigue failure of materials. However, functional fatigue in shape memory alloys corresponds to the thermal cycling, in other words repetitive H/C of the material, under constant applied stress until loss of shape memory effect or failure of the sample. Transformation temperatures shift, actuation strain values decrease and accumulated irrecoverable strain values increase with the thermal cycle numbers during the functional fatigue experiments. Stable actuation fatigue responses and high fatigue cycles are substantial for HT applications. Therefore, it is required to improve the functional fatigue properties and thermal cyclic responses of NiTiHf HTSMAs. There are some factors which influence the fatigue behavior of SMAs such as stress amplitude [22], composition of alloy [23], heat treatment [14,24], experiment environment [21] and surface roughness of test samples [25,26]. Additionally, the influence of UCT upon the thermal cycling stability and functional fatigue response of Nickel-rich NiTiHf alloys was studied in the literature [13]. It was observed that the fatigue life of these alloys decreased with increasing UCT due to the

plastic deformation with phase transformation and viscoplasticity at HT as represented in Figure 2.3-1.

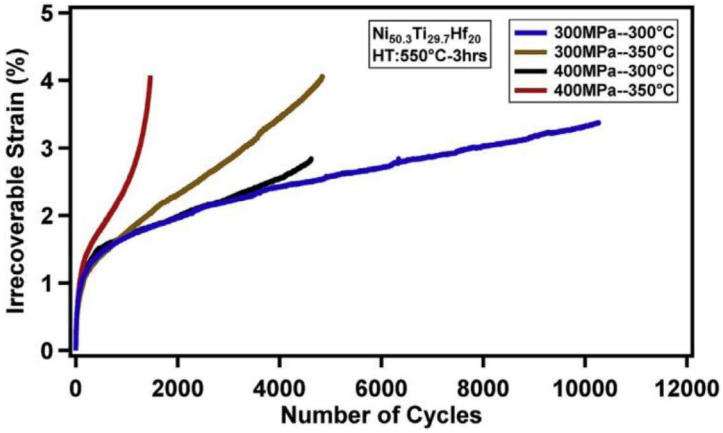

Figure 2.3-1. Irrecoverable strain evolution till failure upon actuation fatigue cycling of the aged at 550°C for 3h $Ni_{50.3}Ti_{29.7}Hf_{20}$ HTSMA for the different stress and UCT levels [13].

The effect of applied stress level and UCTs on the actuation fatigue behavior of nanoprecipitation strengthened $Ni_{50.3}Ti_{29.7}Hf_{20}$ alloys were investigated by Karakoc et al. [13,22,113]. The actuation fatigue experiments via thermal cycling were utilized under different stress levels and using dissimilar UCTs to mainly observe the variation of the actuation strain (ε_{act}), fatigue life and irrecoverable strain with the cycle numbers. Thermal cycling under 200 MPa resulted almost 21.000 cycles with 2.15% average ε_{act}, however, the material failed at about 2.100 cycles with the average ε_{act} of 3.22% under 500 MPa. While the actuation strain increased consistently with increasing stress level owing to the formation of more oriented martensite variants under higher stress levels, the functional fatigue life of the alloy decreased which was attributed to increasing the rates of crack formation. The irrecoverable strain increased continuously for all experiments up to failure and significant irrecoverable strain accumulation was observed upon thermal cycling. It was also seen that 350°C UCT led to achieve half of the fatigue lives compared to thermal cycling by using 300°C as UCT under the same stress levels as shown in Figure 2.3-1. The higher applied stress level & UCT led to obtain less fatigue lives and higher ε_{act}. The decreasing ε_{act} behavior with the increase in

the cycle numbers was observed in the 300°C UCT experiments due to partial transformation which caused to decrease in actuation strain with the number of cycles and impeded damage accumulation induced by phase transformation. On the other hand, first increasing and then almost constant actuation strain values were observed during the experiment which was held using 350°C as UCT. The increasing actuation strain behavior was attributed to acceleration of crack formation at higher UCTs. They stated that upon the complete reversible transformation between martensite and austenite, the opening and closing of the microcracks promoted ε_{act} at the expense of functional fatigue lives of the alloy. Fracture surfaces were also analyzed in these studies and it was observed that while higher UCT and applied stress levels resulted intergranular fracture with rough fracture surface and more intense microcracks, lower UCT and stress levels led to obtain transgranular fracture surface. The same research group studied the effect of microstructure on the actuation fatigue properties of the $Ni_{50.3}Ti_{29.7}Hf_{20}$ alloy [114]. It was reported that the various aging treatments led to the H-phase nanoprecipiates formation in different sizes and morphologies and these precipitates substantially influenced the actuation fatigue properties such as actuation and irrecoverable strain, actuation work-output and fatigue life of the alloy. Saygılı et al. [14] revealed and compared the high cycle fatigue life of the hot extruded & aged at 550°C-3h $Ni_{50.3}Ti_{29.7}Hf_{20}$ alloy. The fatigue life of the alloy was enhanced more than three times after aging heat treatment with achieving improved cyclic stability. While the aged sample failed at 20.337^{th} cycle, the extruded one lost its shape recovery properties at about 5000^{th} cycle. The actuation fatigue tests were utilized twice to examine the repeatability of the tests in this study. Karaman's group has compared the actuation fatigue behaviors of Ni-rich NiTiHf and NiTiZr HTSMAs [115]. The aged NiTiZr alloy represented lower irrecoverable strain and it also showed less ε_{act} and functional fatigue life compared to NiTiHf alloy due to a brittle manner of NiTiZr alloy.

It is known that the actuation fatigue properties of SMAs are so sensitive to compositional and microstructural characteristics. Demblon et al. [27] investigated four batches of Ni-rich NiTiHf alloy to analyze batch-to-batch variations in functional fatigue performance. The small changes in the Nickel-content and vol. fraction of non-metallic inclusions, which were formed in various batches, significantly altered the TTs and actuation fatigue response. Lower Nickel-content and less vol. fraction of inclusions

led to higher functional fatigue life at the expense of stability. The influence of hot extrusion and annealing on the actuation fatigue properties of $Ni_{50}Ti_{30}Hf_{20}$ HTSMA was reported by Kockar's group [17]. The hot extruded samples obtained from the same billet resulted different SM properties such as TTs, actuation and accumulated irrecoverable strains. This discrepancy was attributed to the deformation variation and the residual stress due to microstructural nonuniformity stemming from hot extrusion process. The annealing of the material led to observe the similar shape memory properties, stable TTs, and enhanced actuation fatigue life due to relieving of the stress and overcoming the microstructural uniformity. The same research group has also studied the crack growth rate upon thermal cyclic of extruded and annealed $Ni_{50}Ti_{30}Hf_{20}$ alloy [116]. The pre-notched annealed materials exhibited slower and consistent crack growth rate compared to hot extruded samples which was attributed to the possible stress relieving after annealing process. Babacan et al. [15] performed the actuation fatigue experiments just for 100 cycles on the hot extruded, cold rolled with post annealing and warm rolled $Ni_{50}Ti_{30}Hf_{20}$ alloy. Since the fatigue experiments were not conducted till failure in this study it is not possible to understand the effect of WR and CR process on the fatigue lifetime of these alloys.

2.4. The Effect of Heating/Cooling Rate on Actuation Fatigue Experiments

Since the material is thermally cycled in the functional fatigue experiments to attain thermally-induced martensitic transformation, the frequency of transformation cycles is determined by heating/cooling (H/C) rate. DSC tests are utilized to be able to obtain stress-free phase TTs with the H/C rate of 10°C/min but the different H/C rates were also analyzed for observation of the influence of this rate on the SM behavior of the alloys. Up to now, there is a limited study based upon the H/C rate effect in the functional fatigue experiments in the literature.

The influence of H/C rates on DSC analysis was investigated on the transformation properties of TiNiCu SMA by Wang et al. [36]. The finishing temperatures of martensitic and reverse transformation are highly sensitive to the scanning rates, and M_f declined and A_f increased with increment of rate. The start temperatures of martensite

and parent phases, M_s and A_s respectively, were not susceptible to the change of H/C rate. Nurveren et.al. [37] examined the influence of H/C rate on the transformation properties of heat treated near-equiatomic NiTi alloys via DSC measurements. It was seen that the H/C rate significantly influenced the TTs except M_s and A_s. The absorb heat upon reverse transformation and the released-heat upon forward transformation and also the energy dissipation was enhanced with increasing H/C rate. The various cooling rates with constant heating rate were conducted on the DSC and isobaric thermal cyclic tests by Akgul et al. [16]. The TTs and thermal hysteresis (ΔT) were not sensitive to the alteration of cooling rate but the transformation enthalpies increased with increasing cooling rate which was attributed to the improvement in the measurement precision with DSC at higher rates. The transforming volume and so recoverable strain upon isobaric thermal cyclic were not affected by the alteration of the cooling-rate. The impact of heating rate on a NiTi SMA wire as an actuator was investigated by Monteiro et al. [117]. They observed that even if small variations were obtained in the stress and strain, the heating rate had an influence on force and displacement of the actuator. However, it is worth the mention that, martensitic phase transformation are diffusionless transformations, therefore, the heating/cooling rate used in DSC should not affect the transformation temperatures. Nonetheless, rate can affect the actuation and irrecoverable strain values of HTSMAs due to the time spent at high temperature.

The impact of cooling-rate on the transformation, microstructure and mechanical properties of Nickel-rich NiTi alloys was studied via cooling the samples in furnace, water quenching and dry-ice bath quenching [118,119]. The cooling rate that is applied after heat treatment strongly affected the phase transformation characteristics due to the Ni_4Ti_3 and Ni_3Ti second phases formations that form with diffusion in these alloys. While the cooling rate slightly influenced the grain size of the alloy [118], the higher cooling rates resulted a brittle fracture mode due to higher Ni supersaturation [119].

2.5. The Influence of Hot Extrusion and WEDM

In the presented study, hot extrusion at 900°C with 4 to 1 area reduction was conducted on the as-cast bulk material to homogenize the chemistry and cast structure. It was

observed in the literature that the bulk material is exposed to various plastic deformations along the cross section during extrusion operation which may lead to observe deformation variation [28]. Kumar et al. [28] modeled and simulated the effect of friction on extrusion of non-ferrous alloys as shown in the Figure 2.5-1. The material was exposed to different plastic strain and temperature levels through the cross-section upon extrusion process.

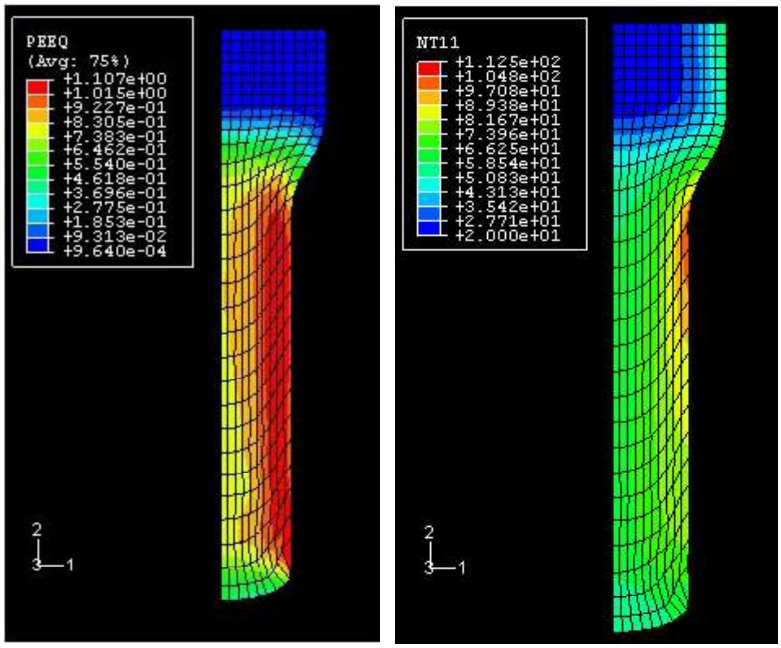

Figure 2.5-1. Plastic strain contours and temperature contours arising from frictional heat generation, respectively [28].

The temperature levels also changes from surface to mid cross section of the material which causes to observe flow variance and nonuniformity throughout microstructure [29–32,120]. Furu et al. [29] observed that the texture of the material varied from the surface to the mid-plane and the recrystallized grains at the surface layer exhibited almost a random texture. Increasing trend for the size of the recrystallized coarse grains from the surface through the midsection of the extruded material was reported by Van Geertruyden et al. in the indirect extrusion [31]. Jiang et al. [32] represented that the microstructure of Ni-based superalloy pipes was clearly associated with hot extrusion parameters. It was also shown by Ocenasek et.al [33] that the mechanical and fatigue

properties of the metals were affected by the microstructural nonuniformity throughout the cross section. They observed that coarse recrystallized surface layers and non-recrystallized structure were obtained after extrusion process. Recrystallized structure led to higher ductility, lower ultimate strength and fatigue lifetimes than those of non-recrystallized structure.

It has been already known that annealing heat treatment at moderate temperature enhances ductility and reduces strength of the metal alloys due to annihilation of dislocations. However, it was also observed in the literature that annealing treatment can increase the mechanical properties of metal alloys via the annihilation of mobile dislocations and thermally rearrangement of the remaining dislocations [34,35]. Gubicza et al. [35] studied the annealing induced strengthening in ultrafine grained NiMo alloys, and the hardening after annealing was attributed to reduction of the mobile dislocations due to annihilation which leads to more difficult plastic deformation. After annealing, the dislocation arrangement parameters substantially depleted due to recovery which caused a more rearranged dislocation configuration and resulted in a strengthening related with the reduction of the dislocation density.

Additionally, NiTi-based SMAs are hard-to-deform materials and so the machining process of these alloys is very difficult via conventional methods. Even though wire electrical discharge machining (WEDM) is usualy utilized for cutting process of these materials due to advantages of this method on high strength alloys, it was shown that surface integrity highly affects the fatigue performance of WED machined specimens. Liu et.al. [26] studied the surface integrity and fatigue lifetime relationship in binary NiTi SMAs. They observed that lower surface roughness and negligible white layers were obtained after the finish trim cut of Nitinol specimens compared to the machine cut samples, and also finish trim cut increased the fatigue performance of the material by 48%. Therefore, the fatigue life of WED machined NiTi SMAs is highly affected by the surface integrity of the sample [25,26].

2.6. Rolling Effect on NiTiHf HTSMAs

As mentioned in the previous sections, Hf addition to the binary NiTi alloy leads to a decrease in ductility because of oxygen and carbon affinity of Hf which causes the oxides and carbides formation [4,18,90]. Additionally, poor cyclic stability can be attributed to the adverse effect of the crystallographic compatibility between martensite and parent phases [60], and remnant strain due to the low CSS for slip [6]. Strengthening methods can be applied to increase the CSS for slip and enhance the shape memory properties of the alloy. Quaternary alloying to obtain solid-solution hardening is another method to enhance the properties but it brings brittleness and increases entropy of the system [97]. Precipitation hardening can also be conducted on alloys which are Ni-rich, however, it is not applicable in equiatomic and Ni-lean NiTiHf alloys [9–12,14,105]. As a consequence, work hardening and grain refinement via applying rolling as thermomechanical treatment are the potential strengthening mechanisms to improve SM and mechanical properties of equiatomic and Ni-lean NiTiHf HTSMAs.

Cold deformation of an equiatomic NiTi alloy at ambient temperature induced martensite stabilization and martensite pinning in conjunction with high dislocation density and decreased TTs and transformation enthalpy [121]. Hot rolling and cold deformation with subsequent heat treatment enhanced the cyclic stability of NiTi alloy which was attributed to increasing the dislocation density and critical stress for slip, and fine coherent precipitates [24,38,122]. The dimensional stability was improved and lower plastic strain was observed in NiTi alloy upon isobaric thermal cyclic experiments after cold deformation and annealing in another study [123]. The transformation strain levels were not susceptible to the amount of cold work and annealing temperature. Nevertheless, increasing cold working amount for the same annealing temperatures and reducing annealing temperature for the same cold working amount enhanced the CSS for slip which led to observe less plastic strain formation. NiTiHf alloys are hard to deform materials and they exhibits highly brittle behavior during cold deformation. Therefore, the impact of hot-rolling on the SM and mech. properties of NiTiHf alloys was studied in the literature [94,95,101,102]. Javadi et al.

[94] examined the role of aging upon the microstructure and SM properties of homogenized and hot-rolled $Ni_{49}Ti_{36}Hf_{15}$ alloy. Hot rolling improved the microstructural characteristics by annihilation of the microstructural voids and resulted uniform distribution of the $(Ti,Hf)_2Ni$ precipitates and eventually enhanced the recoverable strain. The microstructural evolution and texture of $Ni_{49.4}Ti_{38.6}Hf_{12}$ alloys upon hot rolling were investigated by Suresh et al. [95]. The partial dynamic recrystallization were exhibited during hot rolling and large strain heterogeneities around $(Ti,Hf)_2Ni$ second phases were relaxed via dynamic recovery upon further deformation of the material.

The influence of CR and WR on the SM behavior and thermal cycling stability of equiatomic NiTiHf alloy was studied by Babacan et al. [15]. Isobaric thermal cyclic experiments under different constant stresses were conducted on the samples that were cold rolled and subsequently annealed at 550°C for 30 mins and warm rolled at various temperatures and with thickness reductions. The cold rolled materials were exposed to annealing for the dislocation substructure recovery and internal stress relief. It was seen that the rolling improved the endurance against defect generation concomitant with martensitic phase transformation and substantially enhanced dimensional stability upon thermal cyclic experiments. The cold rolling with a 15% of thickness reduction and with subsequent annealing at 550°C for 30 mins provided the optimum actuation results with similar recovered transformation strains but less residual strains compared to the hot extruded condition. They conducted actuation fatigue experiments in this study but the actuation fatigue behaviors of extruded, cold rolled with post annealed and WRed at 600°C-55% thickness reduction samples were investigated for just 100 cycles. Kockar's group researched the transformation properties of the hot extruded and subsequently aged and solutionized and subsequently cold rolled and aged samples of $Ni_{50.3}Ti_{29.7}Hf_{20}$ alloy [103]. The enhanced dimensional stability with no residual strain were observed up to 500 MPa in both hot extruded-aged and solutionized-cold rolled-aged samples. The cold rolled and aged sample exhibited less actuation strain than that of extruded and aged one due to high dislocation amount and possible texture induced by cold rolling.

There are also strengthening mechanisms other than rolling process to improve SM and mechanical behavior of NiTiHf alloys. Belbasi et al. [124] studied hot compression of the $Ni_{49}Ti_{36}Hf_{15}$ alloy at various temperatures and strain rates. They showed that the alloy was not suitable for hot deformation owing to occurrence of flow localization at all temperatures and rates due to dynamic recrystallization. Karaman's group examined the influence of ECAE as severely plastic deformation on the thermal cyclic stability of $Ni_{49.8}Ti_{42.2}Hf_8$ alloy [6]. After extrusion process, thermal cyclic stability improved, transformation strain increased and residual strain decreased due to the microstructural refinement and the increase in the favorable dislocation formations. On the other hand, application of ECAE on these alloys is problematic because of limited ductility of the alloy and high flow strength of the parent phase. The thermal cyclic experiments were performed on hot extruded and wire drawn $Ni_{50}Ti_{35}Hf_{15}$ alloy [100]. The wire drawing process resulted to a decrease in the TTs and enhancement of the material strength and cyclic stability due to increasing the dislocation density and refining the microstructure.

3. EXPERIMENTAL METHODS

3.1. As-Extruded Material

Equiatomic $Ni_{50}Ti_{30}Hf_{20}$ (at.%) alloy was purchased from Sophisticated Alloys Inc. The alloy was produced by using Nickel, Titanium and Hafnium high-purity elements via vacuum induction melting and purging with high purity argon atmosphere. As-cast bulk material was hot extruded at 900°C in a mild steel can with an area reduction ratio of 4:1 for homogenizing the cast structure and chemistry and this condition will be called as 'extruded' throughout the text for this reason. Figure 3.1-1 represents the as-received $Ni_{50}Ti_{30}Hf_{20}$ (at.%) alloy material after hot extrusion process.

Figure 3.1-1. Hot extruded bulk $Ni_{50}Ti_{30}Hf_{20}$ (at.%) alloy [17].

3.2. Annealing Heat Treatment

The hot extruded samples were annealed by wrapping with Tantalum foil to avoid severe oxidation during annealing heat treatment process. The heat treatment was utilized at 550°C-3h under argon atmosphere in a vertical cylindrical furnace as shown in the Figure 3.2-1. At the end of the heat treatment, the samples were cooled at the top region of the vertical furnace to prevent the formation of thermal stresses that may be induced with quenching and so to enhance the fatigue life and the stability of the properties of the material. This region of the furnace is cooled with the water passing

through the copper tubes as shown in Figure 3.2-1. The reason of conducting heat treatment after extrusion process will be clarified later in the text in details. It was stated in the literature that the melting temperature (T_m) of $Ni_{50,3}Ti_{29,7}Hf_{20}$ HTSMA is 1255°C [125] and T_m of $Ni_{50}Ti_{30}Hf_{20}$ HTSMA is assumed to be similar. Therefore, the annealing heat treatment temperature was chosen as 550°C considering the melting temperature of the alloy and it is important to mention that 550°C is approximately half of T_m of the alloy which is used in this study.

Figure 3.2-1. Vertical Cylindrical Furnace.

3.3. Deformation Variation Analysis

The main aim of deformation variation analysis is to enlighten the influence of hot extrusion and following annealing treatment on the actuation fatigue behaviors of equiatomic $Ni_{50}Ti_{30}Hf_{20}$ alloy. The hot extruded bulk material was first cut into pieces to further cutting out the dog bone shape fatigue test specimens from these pieces. The

procedure followed for choosing the specimens from the same extrusion batch to perform the functional fatigue tests is represented in Figures 3.3-1.a-c.

(a) Cut and sliced functional fatigue test samples

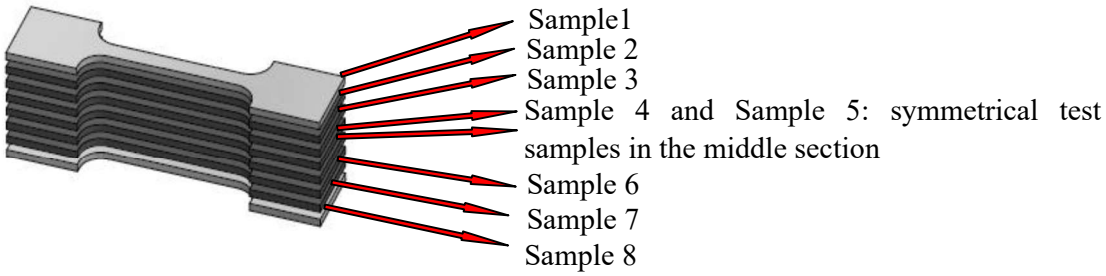

(b) Enumerated and tested 6 functional fatigue test samples from cut and sliced batch

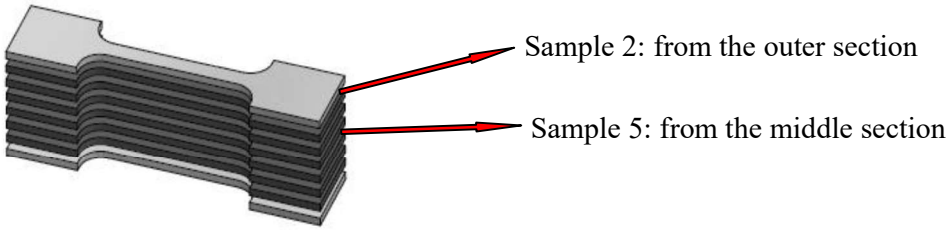

(c) Enumerated, annealed and test functional fatigue test samples

Figure 3.3-1. The procedure followed for the functional fatigue experiments of $Ni_{50}Ti_{30}Hf_{20}$ (at.%) alloy [17].

The pieces were cut and sliced by using WEDM and represented in Figure 3.3-1.a. At first, the samples were randomly selected from the hot extruded billet pieces and functional fatigue experiments were performed on these randomly selected samples with different heating cooling rates. Since the copper wire, which is used in WEDM has 0.5 mm diameter, 8 dog-bone specimens with 1 mm thickness along the cross section can only be obtained from the piece of the hot extruded billet having about 12 mm thickness. Therefore, another piece of the extruded billet were cut and sliced and 8 other specimens were obtained through the cross section of this piece, then six of them were chosen and enumerated for further investigation as shown in Figure 3.3-1.b. The samples with the numbers from 2 to 7 were functional fatigue tested under the same testing conditions. The samples enumerated with 1 and 8 were not suitable for examination. Since the cast billet was cased in steel can for the extrusion, both samples were still covered with the steel residue which may influence the experiment results. Finally, another eight specimens were cut from another piece of the hot extruded billet again. One of the outermost sample (sample 2) and one of the mid section sample (sample 5) were chosen, as exhibited in Figure 3.3-1.c, and annealed at 550°C for 3h for the experiment to single out the influence of annealing on the deformation variation. It is worth to mention that all the specimens in the presented work were obtained from the same batch of the alloy. This procedure was followed to clearly figure out the influence of hot-extrusion process and further annealing on the actuation fatigue behaviors.

3.4. Rolling Operation

Another piece of hot-extruded batch was cut and annealed at 550°C for 3h, and then rolling plates having 1.5mm thickness were cut by using WEDM from the annealed piece. The specimens were mechanically ground before and after rolling operation to remove oxide layer from the surface. The rolling samples were hold for 15 minutes in the Protherm PLF 100/3 cubic furnace to heat them up to desirable rolling temperature, then taken out and non-isothermally rolled directly through the laboratory sized rolling mills driven by electric motor. The cubic furnace and laboratory sized rolling machine are seen in Figure 3.4-1. Table 3.4-1 exhibits the rolling temperatures and thickness

reduction ratio value that was conducted on the extruded and annealed $Ni_{50}Ti_{30}Hf_{20}$ (at.%) alloy.

Figure 3.4-1. Cubic furnace and laboratory sized rolling setup.

Table 3.4-1. Rolling temperatures and thickness reduction ratio applied to the hot extruded and annealed $Ni_{50}Ti_{30}Hf_{20}$ (at.%) HTSMA.

Material Condition	Rolling Temperature (°C)	Thickness Reduction (%)
Hot-extruded and Annealed at 550°C for 3h	600	5
	700	5

Since NiTiHf alloys are hard-to-deform material with high Hafnium content, cold rolling is not so applicable. The material cannot be strengthened sufficiently by hot rolling at higher rolling temperatures due to the recrystallization. Therefore, warm rolling operations were performed at around recrystallization temperatures of the material. The rolling temperatures were chosen as 600°C and 700°C. The thickness reduction of 5% was achieved for both of the rolling temperatures until edge cracks begun to appear at the sample surface. Finally, surface grinding was mechanically

applied to the rolling samples to remove the surface cracks and oxides before functional fatigue experiments.

3.5. Differential Scanning Calorimetry

Stress-free TTs and transformation enthalpies (ΔH) of hot extruded, annealed and warm rolled $Ni_{50}Ti_{30}Hf_{20}$ (at.%) materials were measured by DSC experiments using Perkin Elmer DSC 8000. DSC samples were cut by diamond saw precision cutter at a very low speed and without applying load to avoid inducing internal stress to the material. The upper and lower cycle temperatures of functional fatigue experiments of these materials were determined based on the stress free TTs. Figure 3.5-1 exhibits the determinations of stress free TTs and ΔHs for the forward and reverse martensitic transformation from a heat flow vs temperature curve obtained from DSC experiment. The materials were cycled between 100°C and 400°C for three times to observe the cyclic effect and second cycles of each experiment were chosen to compare the TTs. The H/C rates of experiments were kept constant as 10°C/min for all specimens. The DSC analysis was also performed to atttain stress free TTs and ΔH after the functional fatigue tests with different H/C rates to enlighten the effect of test parameters on the TTs and ΔH magnitudes.

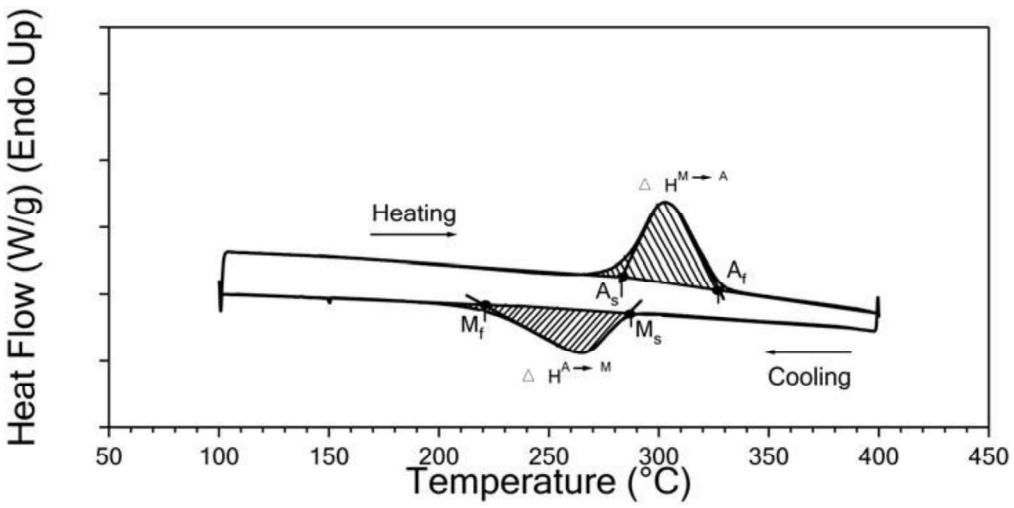

Figure 3.5-1. The schematic of a DSC cycle demonstrating the evaluation of stress free TTs and transformation enthalpies [16].

3.6. Functional Fatigue Experiments

The functional fatigue test samples having dog bone shape with 16.6 mm gage length, 2.25 mm width and about 1mm thickness were obtained from the piece of hot extruded batch via Wire Electrical Discharge Machine (WEDM) to utilize fatigue tests. The functional fatigue experiment sample is presented in Figure 3.6-1 schematically.

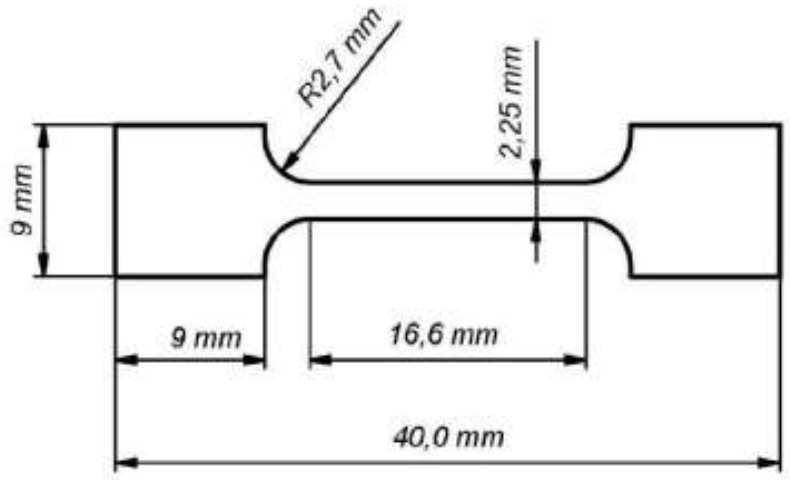

Figure 3.6-1. The schematic of functional fatigue test sample with 1 mm thickness [17].

It was shown in another study of our group that the load-biased experiments were performed on the NiTiHf HTSMA by increment in the applied load with 100 MPa increment [14]. The first irrecoverable strain was observed under 300 MPa stress level. Therefore, it was decided to conduct the functional fatigue tests under 200 MPa constant stress in this study. Thermal cycles were first conducted for different heating/cooling rates as 5, 10, 15, 20 and 25°C/s to observe the effect of H/C rate. It was seen that the SM properties were deteriorated for the lower heating cooling rates because the material was exposed the higher temperature levels during longer times and the test set up could not manage H/C of the sample properly during thermal cycling for the higher H/C rates than that of 20°C/s. Therefore, 15°C/s was determined as the H/C rate for the further experiments. The image and schematic of the custom-made

functional fatigue test setup are given in Figure 3.6-2. The test setup was built up with aluminum sigma profile chassis. The tensile test specimens were attached to upper and lower grips. Constant stress was applied by hanging the dead weights to the bottom grip of test set up. The negative and positive poles of Programmable DC power supply were attached to the grips. Joule heating method was utilized for heating by passing the electric current through the samples and cooling was generated via air cooling. Optris Ctlaser LTF-CF1 infrared thermometer was used to measure the temperature from the mid-sections of the gage length. All samples were sprayed with high temperature black paint to be able to set the emissivity value as a constant which is essential to measure the correct temperature values from the sample surface during the thermal cycling. Emissivity value of high temperature black paint is 0.95. Cooling was provided with compressed air which was blown to the specimen by an air nozzle for the 20°C/s and 25°C/s cooling rates. The amount of air flow was controlled via a digital electro-pneumatic regulator. Air cooling was utilized for the 5, 10 and 15°C/s cooling rates since there is no necessity for forced cooling of the samples with compressed air. A linear potentiometric displacement sensor was utilized to measure displacement of the samples during the thermal cycles. The data from the displacement and the temperature sensors were gathered by National Instruments USB-6003 data logger which was used as input and output device to control the proportional valves. The upper and lower cycle temperatures and the H/C rate were manually entered to the program which was scripted using National Instruments Lab-View Software. The electric current passing along the specimen during heating cycle was controlled by PI controller which was integrated to the system.

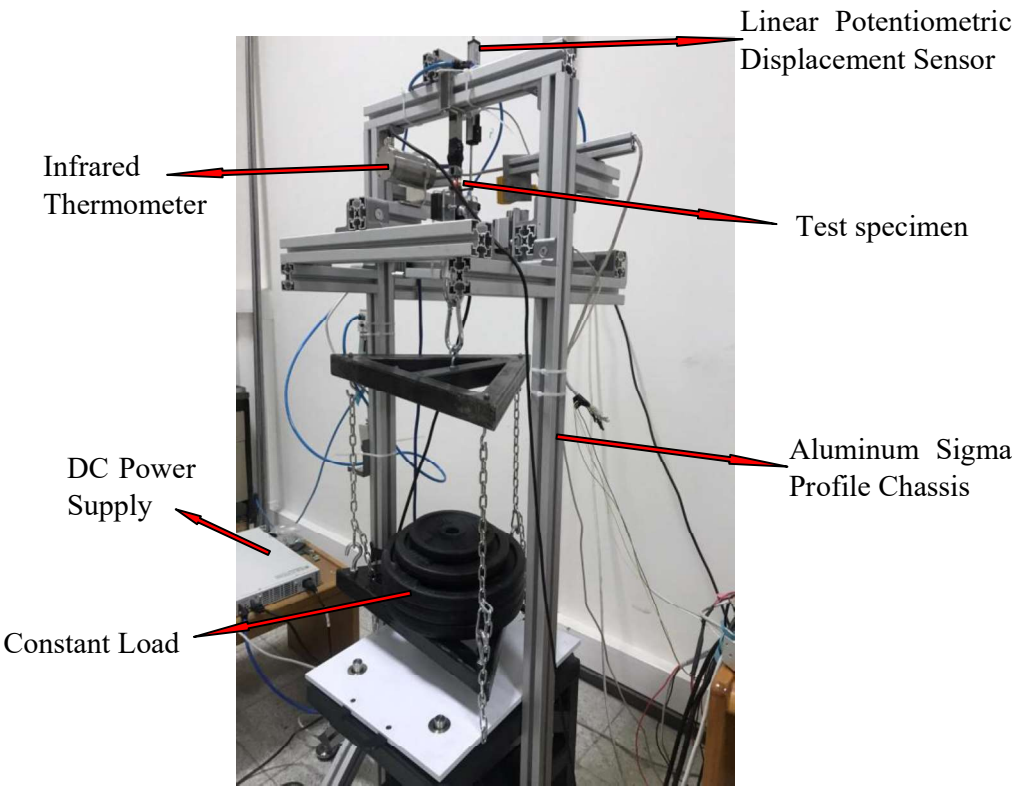

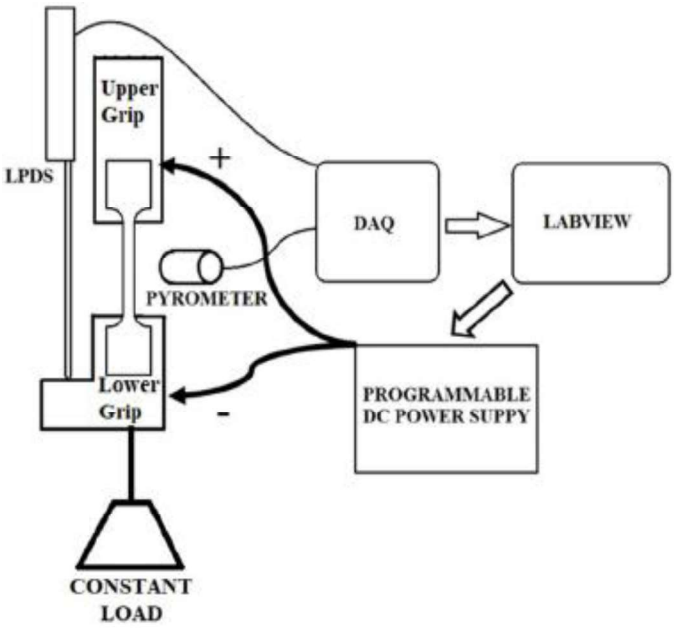

Figure 3.6-2. The image and schematic of custom-made functional fatigue test setup [126].

The method to determine the SM properties from the strain vs. temperature curves, which were attained from functional fatigue experiments, was described in the literature previously [13]. Figure 3.6-3 exhibits the method to draw the SM characteristics such as Martensite Start (M_s), Martensite Finish (M_f), Austenite Start (A_s), and Austenite Finish (A_f) temperatures, Thermal Hysteresis (ΔT), Actuation and Irrecoverable Strain, Martensite Strain and Austenite Strain which is also called as accumulated Irrecoverable Strain.

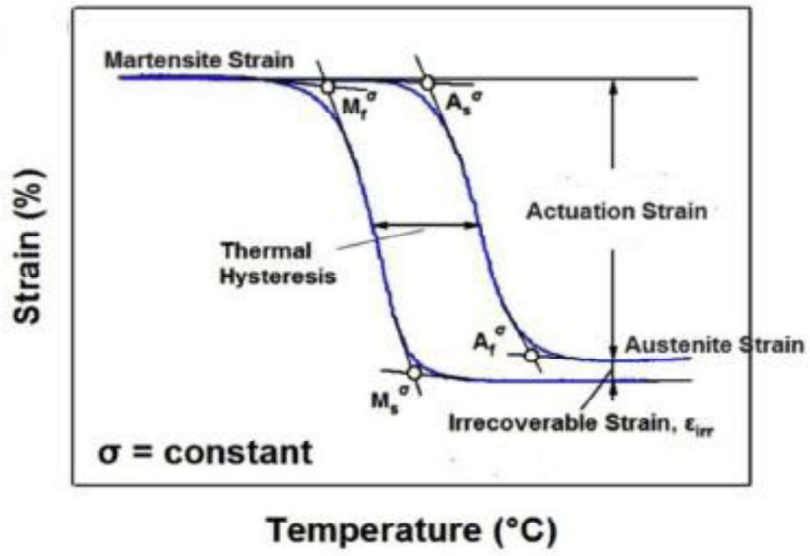

Figure 3.6-3. The schematic illustration of the constant-stress thermal cycling experiment for SMA showing important shape memory characteristics [13].

3.7. Roughness and Microstructural Analysis

It has been already known that the surface/edge roughness of any kind of fatigue test samples affects the fatigue lifetime of the alloys. In this study, the functional fatigue test samples were produced via WEDM method. Although WEDM is a suitable machining method to obtain an appropriate sample surface, possible microcrack formations, especially at the edges of the samples, were investigated under Optical Microscope (OM). The edge roughness and microstructural analyses of the functional fatigue test samples were performed via Nikon Optical Microscope. The specimens were mechanically ground and polished with increasing grid size from 400 up to 2500 papers,

and then polishing was conducted with 6 μm and 1 μm alumina polishing cloths, respectively. The side surfaces of gage section of the specimens were manually ground down to 1200 grid size grinding paper before functional fatigue experiments. For the microstructural analysis of the extruded and annealed materials, they were etched by the solution that includes 7% HF, 18% HNO_3 and 75% H_2O (at vol.).

3.8. Fracture Surface and Chemical Element Distribution Analysis

Post-fatigue fracture surface of failed samples tested for 5, 10, 15 and 25°C/s heating/cooling rates were analyzed using JEOL 6400 Scanning Electron Microscope in back scattered electron mode in Bilkent University National Nanotechnology and Research Center (UNAM). Crack formation and fracture surface structure were investigated for the samples, which were functional fatigue. Moreover, Energy Dispersive Spectrometry (EDS) which was attached to JEOL 6400 Scanning Electron Microscope was conducted to map the chemical element distribution of Ni, Ti and Hf elements to reveal the chemical homogeneity of the hot-extruded specimens.

3.9. Hardness Tests

Hardness tests were utilized on the hot extured, annealed at 550°C-3h, warm rolled at 600°C & 700°C materials to clarify the influence of annealing and warm rolling. Vickers Hardness measurements were conducted at room temperature via 100g applied load to the specimens. Ten hardness values were obtained for each sample; the average hardness values were calculated and recorded as the hardness of the materials.

4. EXPERIMENTAL RESULTS and DISCUSSION

4.1. The Effect of Heating/Cooling Rate on Randomly Selected Samples

As explained in the background section, the high number of fatigue lives and stable with reliable actuation fatigue properties are substantial for high temperature applications of NiTiHf HTSMA. It is known that SME is significantly related with the martensitic transformation and it is diffusionless military type phase transformation, so it means that the transformation is time independent. The rates of H/C during thermal cycling should not be effective on the martensitic transformation of the alloy. Nevertheless, the heating is provided by joule heating method via passing DC electric current through the material for the actuation fatigue experiments as mentioned in the experimental method section. The conductivity of the material may be changing for different heating and cooling rates due to microstructural evolution and thus, the functional fatigue lifetime and SM response of the alloy may be affected.

Actuation fatigue experiments with variable heating-cooling rates, such as 5, 10, 15, 20 and 25°C/s, were conducted on randomly selected hot-extruded $Ni_{50}Ti_{30}Hf_{20}$ (at.%) samples. The effect of aging, UCT and applied stress level were aforementioned on the functional fatigue properties of Ni-rich $Ni_{50.3}Ti_{29.7}Hf_{20}$ (at.%) alloy in the literature [13,14,22]. The low cycle fatigue tests (100 cycles) on $Ni_{50}Ti_{30}Hf_{20}$ (at.%) HTSMA were also utilized [15], however, there has been almost no study exhibiting the actuation fatigue cycles up to failure for stochiometric $Ni_{50}Ti_{30}Hf_{20}$ (at.%) alloy. Moreover, the fatigue tests were repeated for twice on the specimens obtained from the same batch and accepted as consistent repeatable results in the literature. Nevertheless, in the presented study, the functional fatigue experiments were repeated for three times for some heating/cooling rates on randomly selected WEDM cut specimens in the hot-extruded condition to show how consistent the SM properties and fatigue lives of the alloy.

4.1.1. DSC Comparison of Randomly Selected Extruded Samples

Figure 4.1-1 illustrates the change in TTs and ΔHs of the randomly selected specimens under stress free condition prior to the fatigue experiments and post fatigue experiments for different heating cooling rates. The aforementioned values were obtained from the DSC analysis and are summarized in Table 4.1-1. The DSC specimens of post fatigue samples were cut from the gage section of the specimens but slightly away from the failure surface. Transformation enthalpy decreases after functional fatigue experiments due to increasing dislocation density which leads to a decrease in the martensitic transformation volume due to inhibiting the martensite-austenite boundary motion. Also, M_s and M_f temperatures are not distinct in post-fatigue DSC curves. Additionally, M_f and A_s temperatures decrease noticeably after the fatigue experiments. The decrease in the M_s temperatures is not as much as that is observed for M_f and A_s temperatures. On the other hand, there is a minor change in the A_f temperature after fatigue cycles. The decrease in M_s and M_f temperatures can be attributed to the increase in overcooling for martensitic transformation. Postmortem DSC experiment that was conducted on the sample coded with 5°C/s_1, which was thermally cycled with 5°C/s heating/cooling (H/C) rate under 200MPa exhibits less distinct transformation curve and lowest transformation enthalpy compared to the results of the postmortem DSC tests conducted on the samples that were thermally cycled with different H/C rates. So, it was difficult to determine the transformation temperatures due to broad and shallow DSC curve of the sample coded with 5°C/s_1.

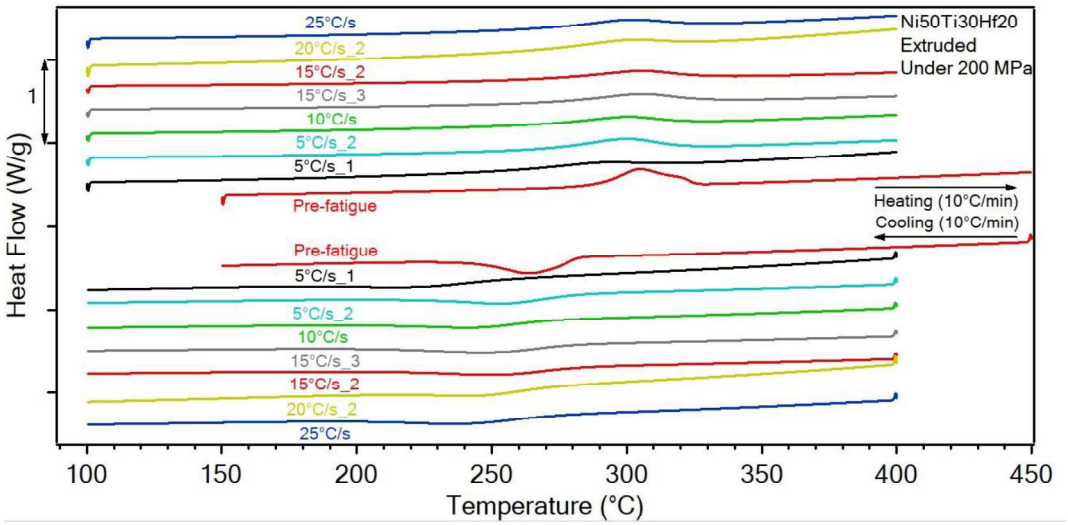

Figure 4.1-1. Pre-fatigue and post-fatigue DSC results of extruded $Ni_{50}Ti_{30}Hf_{20}$ (at.%) samples, which was not thermally cycled and thermal cycled with 5, 10, 15, 20 and 25°C/s.

Table 4.1-1. TTs, ΔT (°C) and ΔH which were drawn from the DSC curves that were shown in Figure 4.1-1.

Heating Cooling Rates	**Transformation Temperatures (°C)**				**Thermal Hysteresis (A_f-M_s)(°C)**	**Transformation Enthalpy (J/g) ($\Delta H_{cooling}$)**
	Mf	**Ms**	**As**	**Af**		
Pre-fatigue	236	282	286	330	48	26.72
5°C/s_1	177	256	252	320	65	12.25
5°C/s_2	214	283	270	322	39	22.74
10°C/s	200	274	266	324	50	17.15
15°C/s_3	203	281	268	331	50	20.75
15°C/s_2	205	284	266	331	47	19.95
20°C/s_2	208	274	263	328	54	15.93
25°C/s	198	274	265	328	54	17.91

4.1.2. Functional Fatigue Experiments of Randomly Selected Samples on Various H/C Rates

Functional fatigue experiments were conducted on the randomly selected hot-extruded $Ni_{50}Ti_{30}Hf_{20}$ (at%) samples with different heating-cooling rates, such as 5, 10, 15, 20 and 25°C/s, up to failure to analyze the effect of H/C rate on the SM behavior and the fatigue lifetime of the alloy. The experiments were repeated twice on 5°C/s and 20°C/s H/C rates and three times on 15°C/s rate to observe the consistency and reliability of the experiments. All the tests were performed under 200 MPa constant stress and the load was calculated by considering the initial cross sections of the test specimens. Strain vs temperature thermal cycles of the functional fatigue experiments are represented in Figures from 4.1-2 (a) to 4.1-2 (i) and the fatigue life results are tabulated in Table 4.1-2.

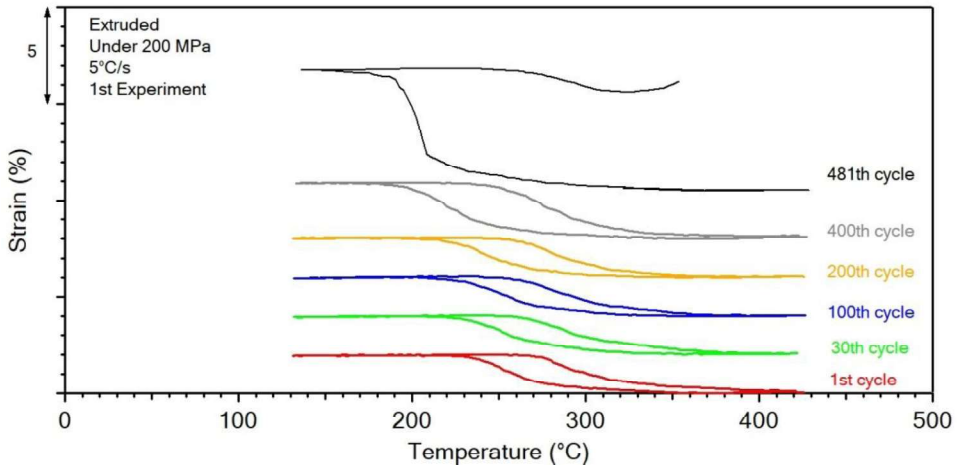

(a)

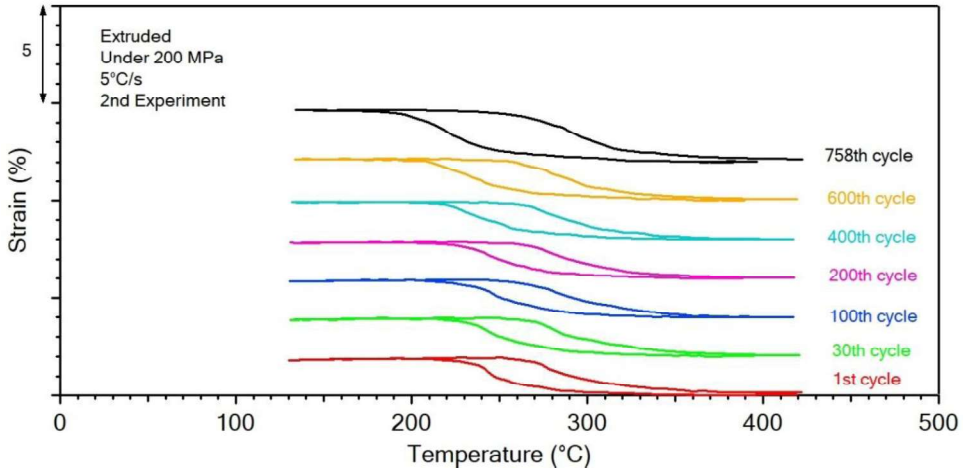
Extruded
Under 200 MPa
5°C/s
2nd Experiment
5
Strain (%)
758th cycle
600th cycle
400th cycle
200th cycle
100th cycle
30th cycle
1st cycle
0
100
200
300
400
500
Temperature (°C)

(b)

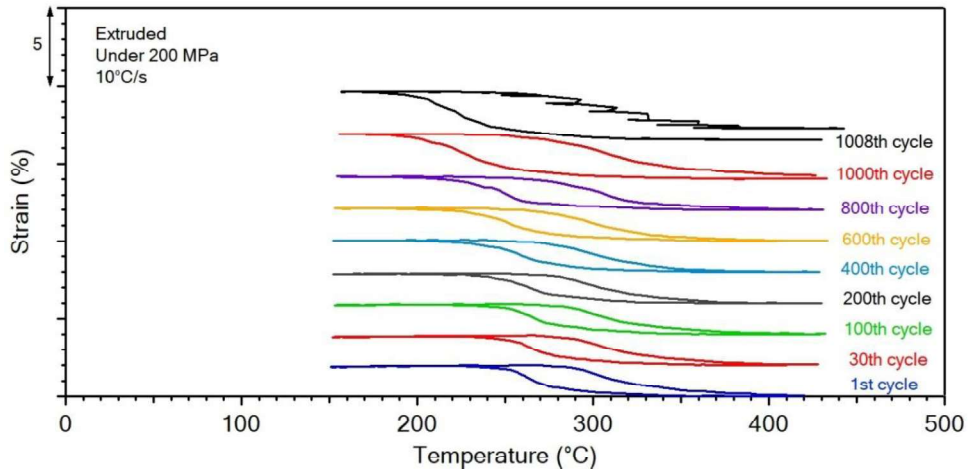
Extruded
Under 200 MPa
10°C/s
5
Strain (%)
1008th cycle
1000th cycle
800th cycle
600th cycle
400th cycle
200th cycle
100th cycle
30th cycle
1st cycle
0
100
200
300
400
500
Temperature (°C)

(c)

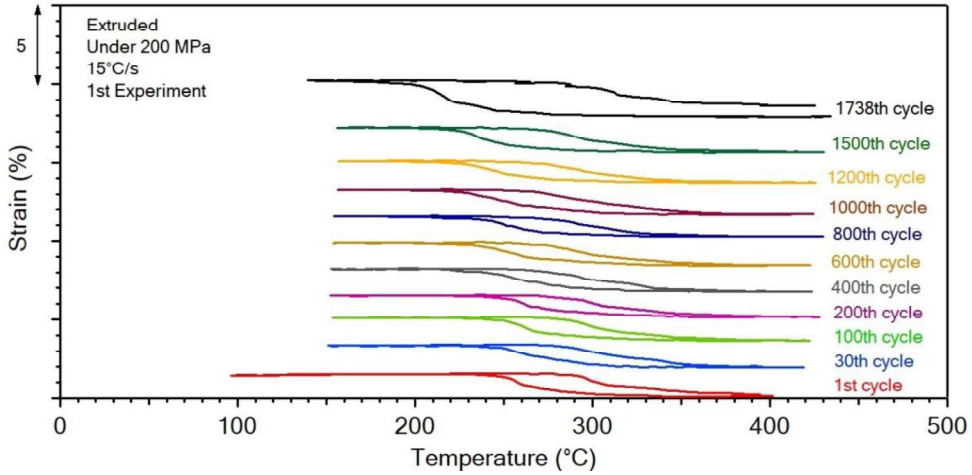
Extruded
Under 200 MPa
15°C/s
1st Experiment
5
Strain (%)
1738th cycle
1500th cycle
1200th cycle
1000th cycle
800th cycle
600th cycle
400th cycle
200th cycle
100th cycle
30th cycle
1st cycle
0
100
200
300
400
500
Temperature (°C)

(d)

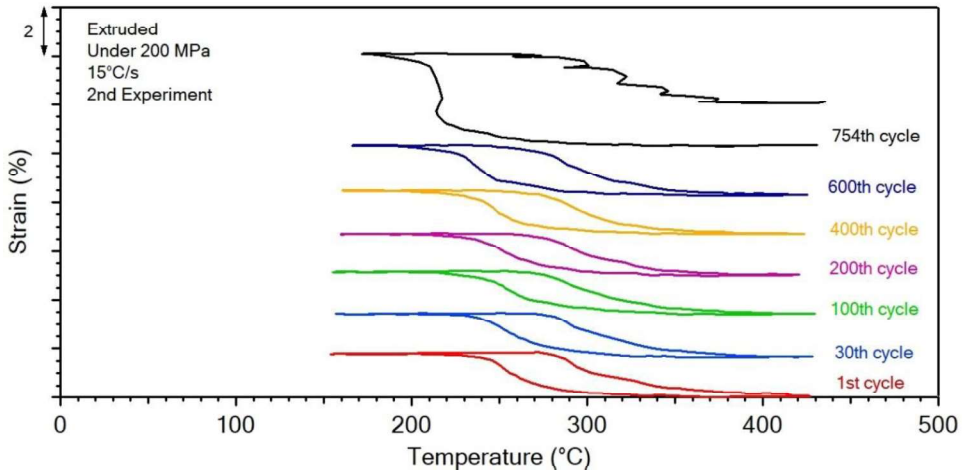
Extruded
Under 200 MPa
15°C/s
2nd Experiment
754th cycle
600th cycle
400th cycle
200th cycle
100th cycle
30th cycle
1st cycle
Strain (%)
Temperature (°C)
2
0
100
200
300
400
500

(e)

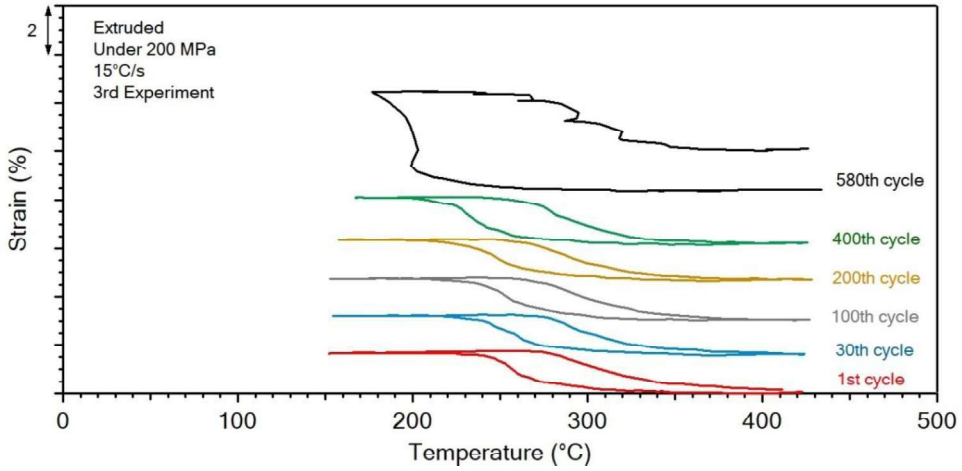
Extruded
Under 200 MPa
15°C/s
3rd Experiment
580th cycle
400th cycle
200th cycle
100th cycle
30th cycle
1st cycle
Strain (%)
Temperature (°C)
2
0
100
200
300
400
500

(f)

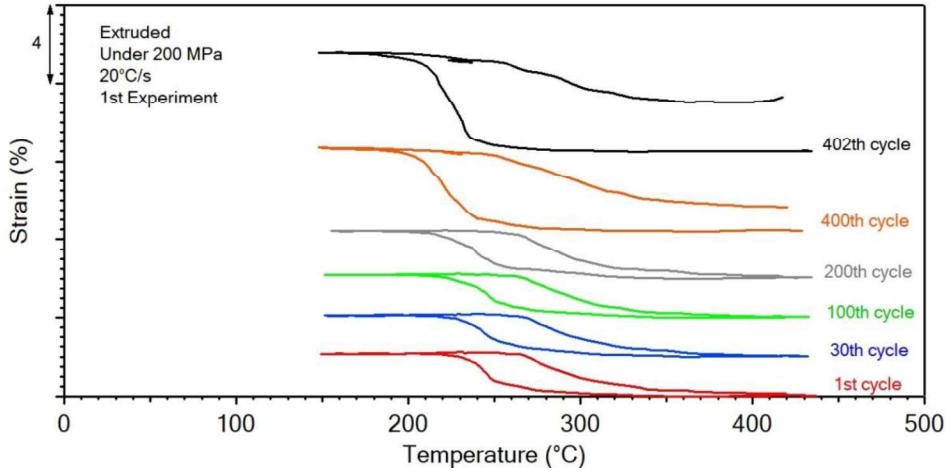
Extruded
Under 200 MPa
20°C/s
1st Experiment
402th cycle
400th cycle
200th cycle
100th cycle
30th cycle
1st cycle
Strain (%)
Temperature (°C)
4
0
100
200
300
400
500

(g)

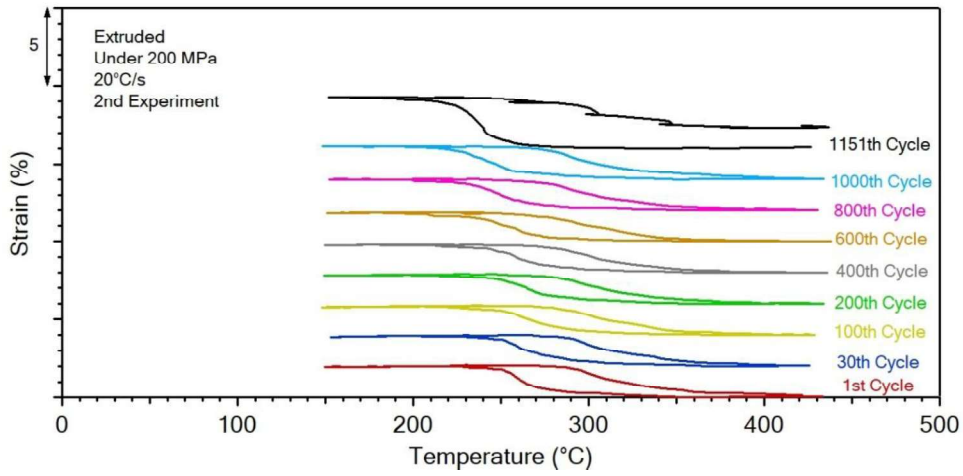

(h)

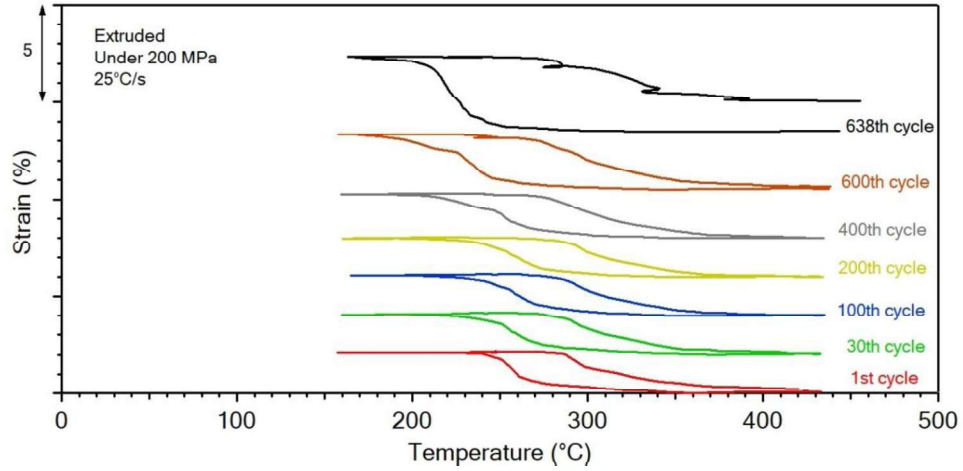

(i)

Figure 4.1-2. ε vs T responses of the randomly selected hot-extruded samples from the functional fatigue experiments under 200 MPa constant stress for different H/C rates; (a) 5°C/s first experiment, (b) 5°C/s second experiment, (c) 10°C/s, (d) 15°C/s first experiment, (e) 15°C/s second experiment, (f) 15°C/s third experiment, (g) 20°C/s first experiment, (h) 20°C/s second experiment and (i) 25°C/s.

Table 4.1-2. Functional fatigue life results for different H/C rates obtained from functional fatigue tests on the hot-extruded $Ni_{50}Ti_{30}Hf_{20}$ HTSMA samples.

Heating/Cooling Rates	**Functional Fatigue Life**
5°C/s_1st experiment	failed at 481st cycle
5°C/s_2nd experiment	failed at 758th cycle
10°C/s	failed at 1008th cycle
15°C/s_1st experiment	failed at 1738th cycle
15°C/s_2nd experiment	failed at 754th cycle
15°C/s_3rd experiment	failed at 580th cycle
20°C/s_1st experiment	failed at 402nd cycle
20°C/s_2nd experiment	failed at 1151st cycle
25°C/s	failed at 638th cycle

It was actually considered that actuation fatigue experiment would be conducted with 1°C/s heating-cooling rate as the lowest rate but it was realized that the minimum 5°C/s heating-cooling rate can be carried out accurately by the custom-made test setup and the materials failed at 481^{th} and 758^{th} cycles for 5°C/s heating-cooling rate as shown in Figure 4.1-2.a and Figure 4.1-2.b. To identify the impact of H/C rate on the fatigue life, the actuation fatigue experiment was conducted up to failure with 10°C/s heating-cooling rate on the randomly selected hot-extruded specimen and the sample failed at 1008^{th} cycle. The thermal cycles for this experiment are shown in Figure 4.1-2.c. Then, functional fatigue experiments were run and repeated for 15°C/s rate on the three randomly selected extruded specimens under the same constant stress level up to failure, and the samples failed at 1738^{th}, 754^{th} and 580^{th} cycles as exhibited in Figures 4.1-2.d, 4.1-2.e and 4.1-2.f, respectively. The fatigue experiments were also applied with 20°C/s H/C rate for twice to analyze the impact of rate on the SM behaviors and the failure was observed at 402^{th} and 1151^{th} cycles, as shown in Figures 4.1-2.g and 4.1-2.h, respectively. Finally, the actuation fatigue test was performed with 25°C/s as the maximum heating-cooling rate that is considered as the limitation of the test setup and the specimen failed at 638^{th} cycle represented in fig. 4.1-2.i.

The drawing procedure of shape memory properties from the functional fatigue curves was described previously in the experimental methods section. The TTs evolution, such as M_s, M_f, A_s and A_f, with respect to number of cycles for fatigue experiments conducted with 5, 10, 15, 20 and 25°C/s H/C rates are shown in Figures from 4.1-3.a to 4.1-3.d. It was observed that M_s and M_f temperatures decreased with increasing number of cycles as can be seen in Figures 4.1-3.c and 4.1-3.d because of the increment in dislocation density, so, relatively larger overcooling was necessary to complete martensitic transformation. The samples, which were thermally cycled with 10, 15 and 20°C/s H/C rates exhibited higher M_s than that of the second and third samples that were thermally cycled with 15°C/s, the second sample that was thermally cycled with 20°C/s tests and the samples that were thermally cycled with 5°C/s. All transformation temperature values were in close-range for the first 200th cycle for all samples that were thermally cycled with different H/C rates, and then they started to diverge with increasing number of cycle after 200th cycle shown in Figures 4.1-3.a-c.

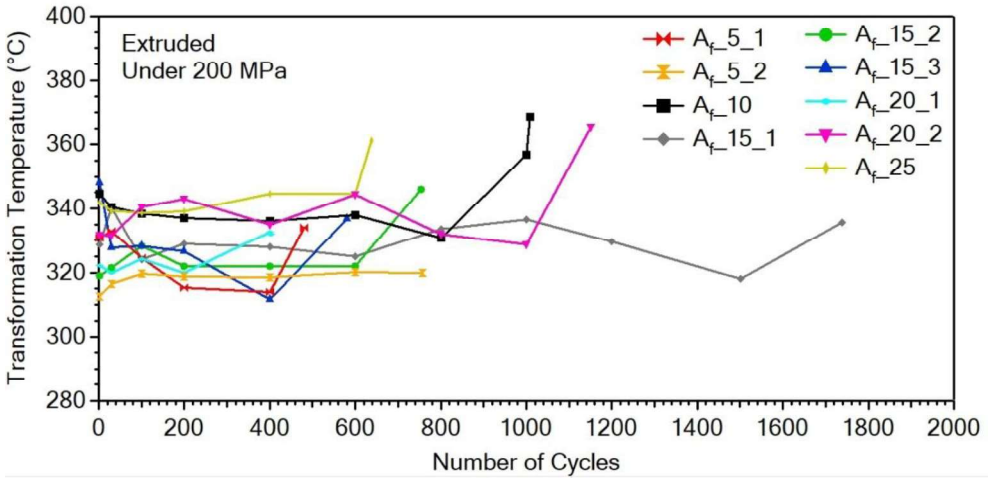

(a)

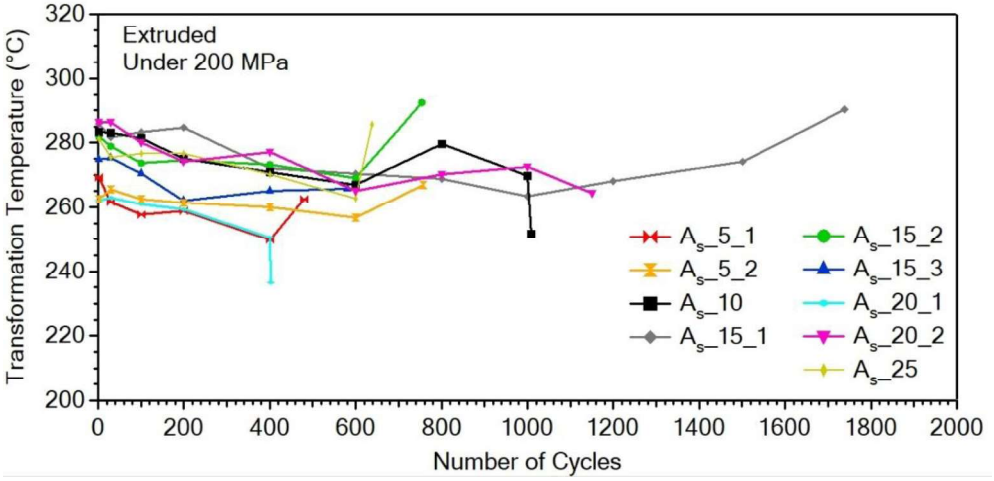
Extruded
Under 200 MPa
Transformation Temperature (°C)
Number of Cycles
320
300
280
260
240
220
200
0
200
400
600
800
1000
1200
1400
1600
1800
2000
A_s_5_1
A_s_5_2
A_s_10
A_s_15_1
A_s_15_2
A_s_15_3
A_s_20_1
A_s_20_2
A_s_25

(b)

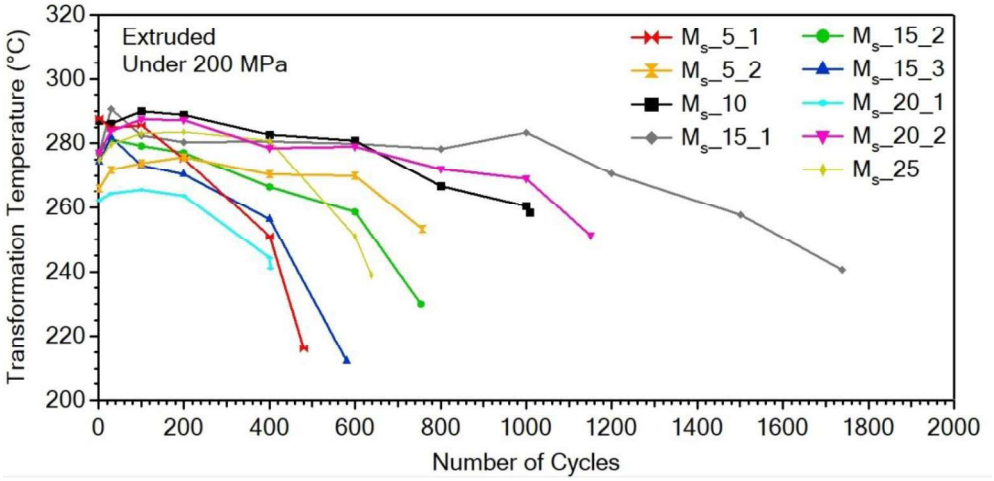
Extruded
Under 200 MPa
Transformation Temperature (°C)
Number of Cycles
320
300
280
260
240
220
200
0
200
400
600
800
1000
1200
1400
1600
1800
2000
M_s_5_1
M_s_5_2
M_s_10
M_s_15_1
M_s_15_2
M_s_15_3
M_s_20_1
M_s_20_2
M_s_25

(c)

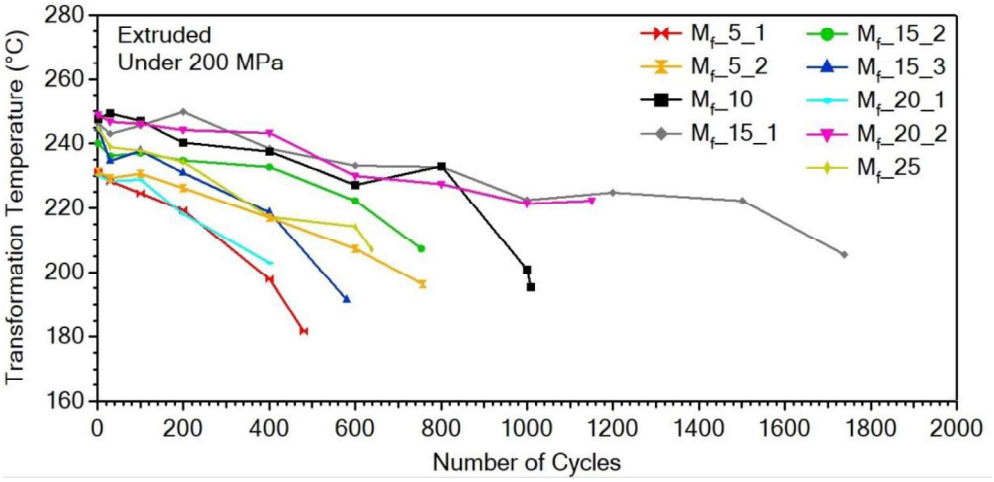
Extruded
Under 200 MPa
Transformation Temperature (°C)
Number of Cycles
280
260
240
220
200
180
160
0
200
400
600
800
1000
1200
1400
1600
1800
2000
M_f_5_1
M_f_5_2
M_f_10
M_f_15_1
M_f_15_2
M_f_15_3
M_f_20_1
M_f_20_2
M_f_25

(d)

Figure 4.1-3. TTs (°C) which were drawn from functional fatigue experiments for the extruded $Ni_{50}Ti_{30}Hf_{20}$ alloy as a function of cycle numbers for 5, 10, 15, 20 and 25°C/s H/C rates; (a) A_f, (b) A_s, (c) M_s and (d) M_f.

The thermal hysteresis (ΔT), actuation (ε_{act}) and accumulated irrecoverable strain ($\varepsilon_{austenite}$) with cycle numbers of the fatigue experiments that were conducted with 5, 10, 15, 20 and 25°C/s H/C rates were drawn and are presented in Figures from 4.1-4.a to 4.1-4.c, respectively. Large internal stress is induced and elastic strain energy of the material may be enhanced with loading of the specimens which facilitates martensitic transformation, so the thermal hysteresis decreased for all experiments at the beginning [127]. Until 200th cycles, the materials exhibited almost stable ΔT behavior for different H/C rates and the ΔT values of samples increased after 200th cycle as shown in Figure 4.1-4.a because the martensite-austenite boundary became immobile by the dislocations with increasing cycle numbers. The lowest ε_{act} values were observed for the first 15°C/s H/C rate test which represented the highest number of cycles and became almost stable along the cycles as represented in Figure 4.1-4.b. The most notable observation from all the ε_{act} results was obtaining dissimilar values from the experiments with the same heating-cooling rates. Additionally, it can be noticed from figure 4.1-4.c that the divergence of $\varepsilon_{austenite}$ was discernable after 200th cycle.

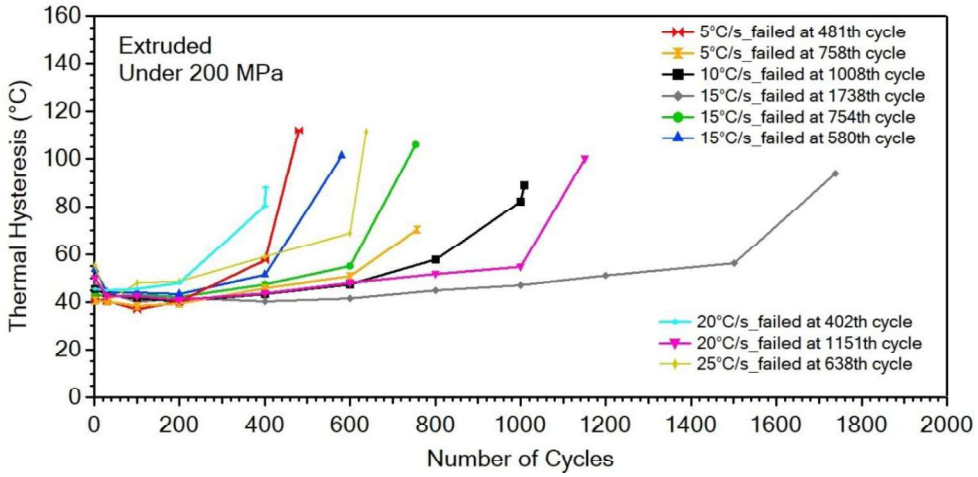

(a)

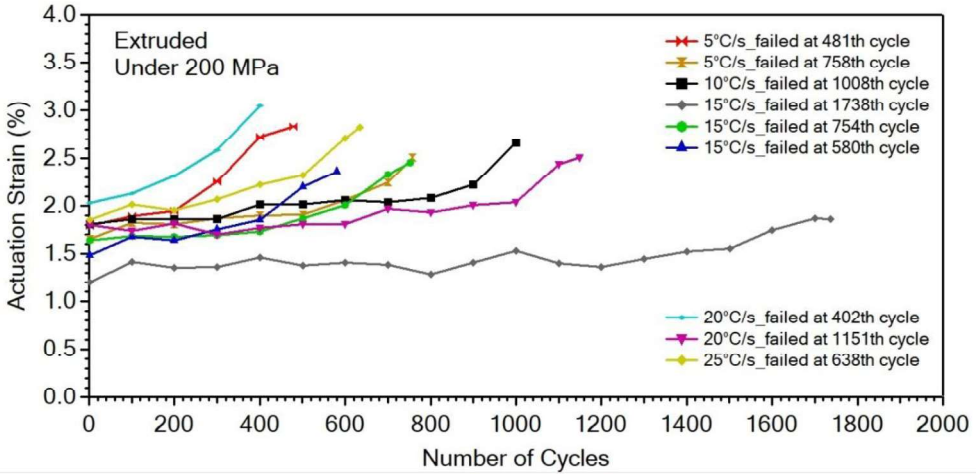

(b)

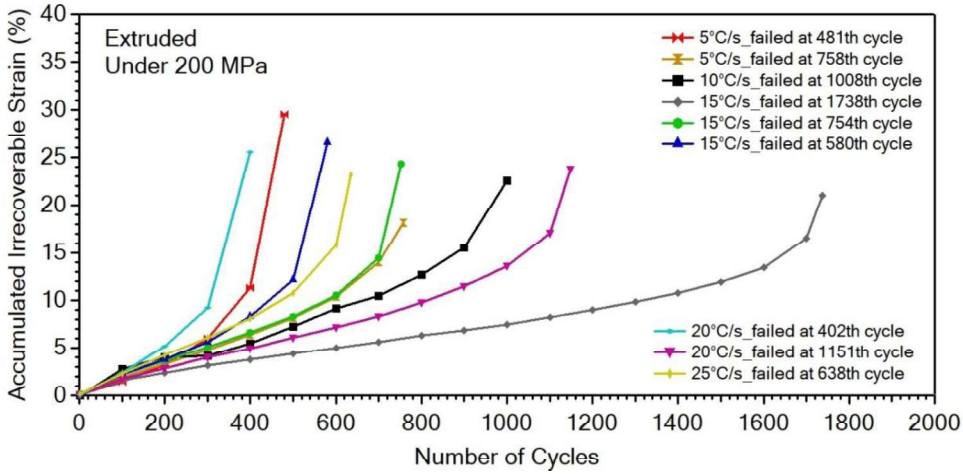

(c)

Figure 4.1-4. (a) ΔT, (b) ε_{act} and (c) $\varepsilon_{austenite}$ evolution with cycle numbers of the randomly selected extruded samples for 5, 10, 15, 20 and 25°C/s H/C rates obtained from the functional fatigue experiments.

It was shown in the previous studies that the shape memory behaviors do not change for the first 100 cycles for the specimens having similar thermal and/or thermomechanical conditions. Similarly, it is the same in the presented study in fact when the first 100 cycles are considered. Nevertheless, the functional fatigue experiments were conducted up to failure. Even though the experiments were performed at the same H/C rate and using the same UCT, different fatigue lives were observed as shown in Table 4.1-2 and

different shape memory behaviors were also obtained as it is presented in Figures 4.1-3 and 4.1-4.

4.1.3. Post-Fatigue Fracture Surface Analysis

Post-fatigue fracture surfaces of the randomly selected hot-extruded samples tested for various H/C rates were analyzed and illustrated in Figures from 4.1-5.a to 4.1-5.d. The fractography examination with Scanning Electron Microscope (SEM) revealed mixed fracture mode of intergranular cracking with rock-candy triple points, transgranular cracking with river pattern and ductile dimples for the samples that were thermally cycled with 5°C/s first experiment, 10°C/s and 15°C/s H/C rates, and sample that was thermally cycled with 25°C/s rate showed mixed of transgranular cracking with river pattern and dimples. The fracture surface examination indicated that the lower H/C rates led to observe more intergranular cracking mode seen in Figures 4.1-5.a to 4.1-5.c while the higher rate caused more transgranular mode as presented in Figure 4.1-5.d. Since the materials were exposed to higher temperature levels for longer time for lower H/C rates such as 5, 10 and 15°C/s, mixed of transgranular cracking, intergranular cracking and ductile dimples were observed for these rates. Necking and high elongation were also seen during thermal cyclic under constant stress tets for the specimens tested at these rates. On the other hand, the highest rate 25°C/s resulted flat fracture surface and more brittle fracture compared to the other rates which can be attributed to the less exposure to higher temperatures.

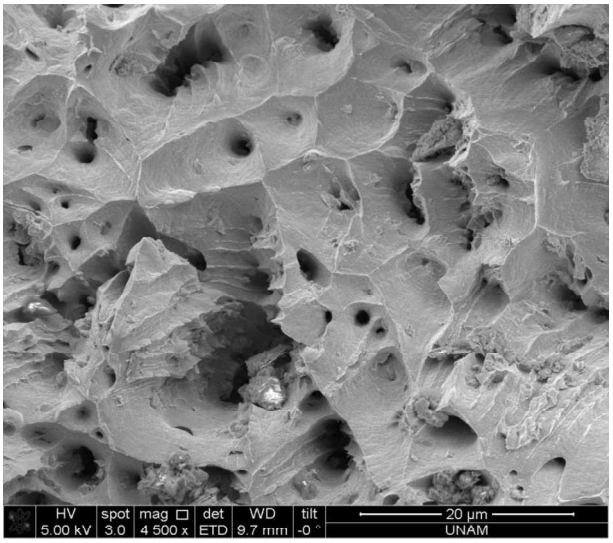
HV spot mag det WD tilt
5.00 kV 3.0 4 500 x ETD 9.7 mm -0 °
20 µm
UNAM

(a)

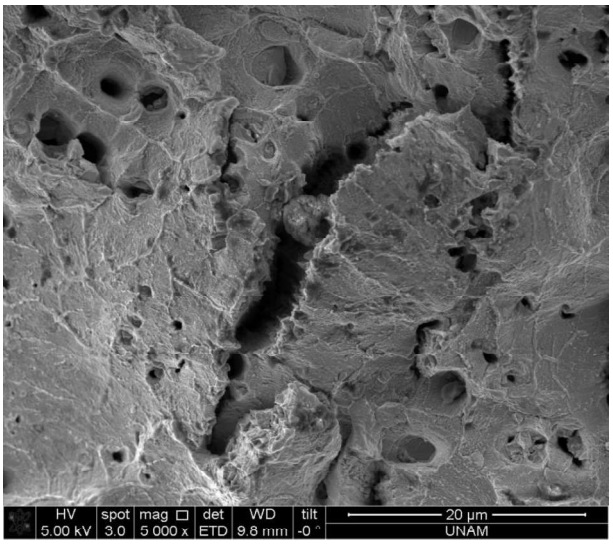
HV spot mag det WD tilt
5.00 kV 3.0 5 000 x ETD 9.8 mm -0 °
20 µm
UNAM

(b)

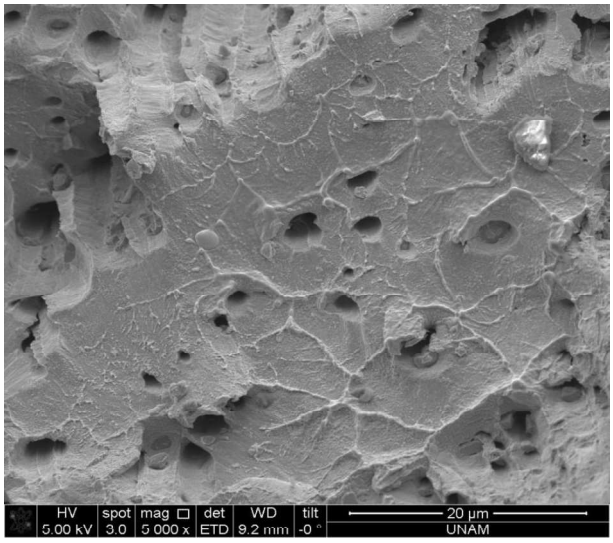

(c)

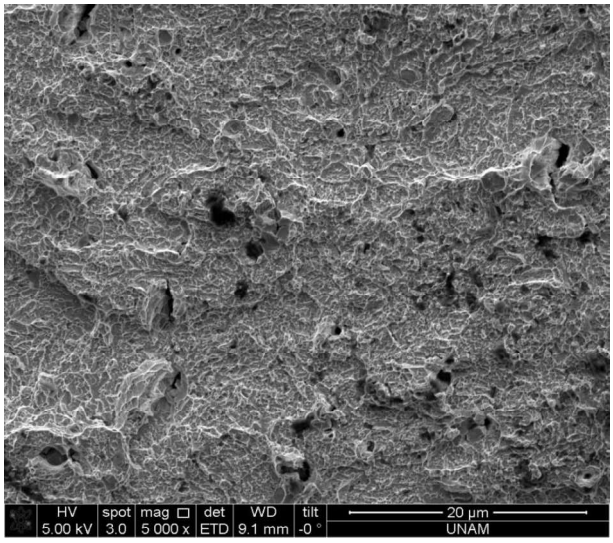

(d)

Figure 4.1-5. Backscattered scanning electron micrographs of the fracture surface of the extruded specimens following failure for the functional fatigue experiment for different H/C rates; (a) 5°C/s first experiment, (b) 10°C/s, (c) 15°C/s first experiment and (d) 25°C/s.

4.2. Temperature Distribution Analysis of Functional Fatigue Test Setup

As explained in the previous sections, the joule heating method was used for heating the specimens during the functional fatigue experiments. DC electric current passes through the samples and they were heated up to desirable temperatures due to the resistivity of the material. The possible change of the conductivity for the different H/C rates was considered and temperature homogeneity was analyzed for steady state and transient conditions. The heating inhomogenity on the test specimen during thermal fatigue test would be another possible reason for obtaining different shape memory properties for the same heating cooling rate. The five points were determined on test specimen from top to bottom as seen in Figure 4.2-1.

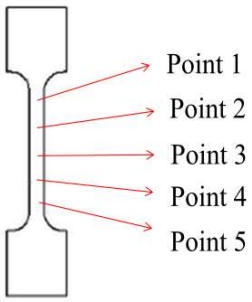

Figure 4.2-1. Schematic illustration of the specimen and 5 points from which the measurements were taken for temperature distribution analysis.

4.2.1. Steady-state condition

The temperatures from 5 points that were shown in Figure 4.2-1 were measured by infrared pyrometer at constant temperatures and the temperature distributions were drawn for each temperature as shown in Figure 4.2-2. The middle section of the specimen, where the point 3 can be seen, reaches the set temperatures which were 150, 200, 250, 300, 350, 400 and 430°C. However, the temperature difference between the set temperature and measured temperature increased as the distance between the middle and the top/bottom parts of gage section of the specimens increased. The highest temperature difference was obtained at the top and bottom part of the gage of the samples. The temperature difference between point 3 and point1/point 5 was observed

to be highest when the temperature was set to the highest values which was 430°C. The lower temperatures, which were measured from point 1 and point 5 are close to the upper and lower grips and the heat loss through the grips with conduction causes this temperature difference during the fatigue test.

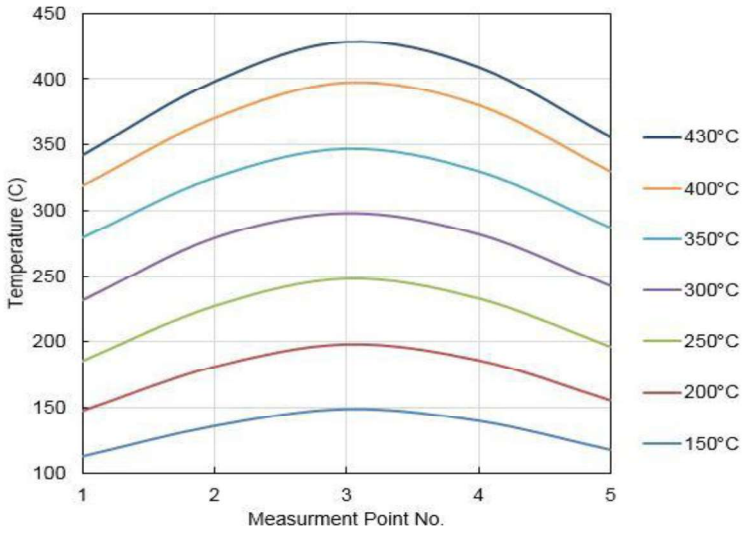

Figure 4.2-2. The results of the temperature distribution for steady state condition through the gage section of the test specimen.

4.2.2. Transient condition

For transient condition temperature distribution analysis, thermal cycling between 150°C and 430°C was utilized on a sample with 5, 10, 15, 20 and 25°C/s H/C rates. Figure 4.2-3 shows the transient condition temperature distribution analysis results for 15°C/s which is the avarage heating cooling rate as an example. Temperature values were collected by two different infrared pyrometers at the same time during thermal cycles. The first pyrometer was fixed and seeing the point 3 which was located on one of the face of the test sample for all thermal cycling experiments as shown in Figure 3.6-2 in the experimental methods section. The second pyrometer was replaced on the other side of test set up and seeing the other face of test sample, and this pyrometer was moved up and down and measured the temperature values from 5 different points through the gage section of the sample during thermal cycling one by one. For example, the second pyrometer was replaced to collect the data from point 1, then thermal cycling

was performed and Figure 4.2-3.a was drawn with the collected data. The straight black lines represent the set temperature values with respect to time that the test set up tries to follow during thermal cycles as much as possible. The red lines represent the temperature values with respect to time collected by the first pyrometer fixed to see the point 3 and these temperatures are called as reference temperatures. The green lines represent the temperature values with respect to time gathered by second pyrometers from 5 different points and called as measured temperatures. The reference and measured temperatures were almost on top of each other for the 3rd point which is representing the mid point of the test sample. The highest divergence was observed for the 1st and 5th points which are representing the top-bottom points of gage section of the sample.

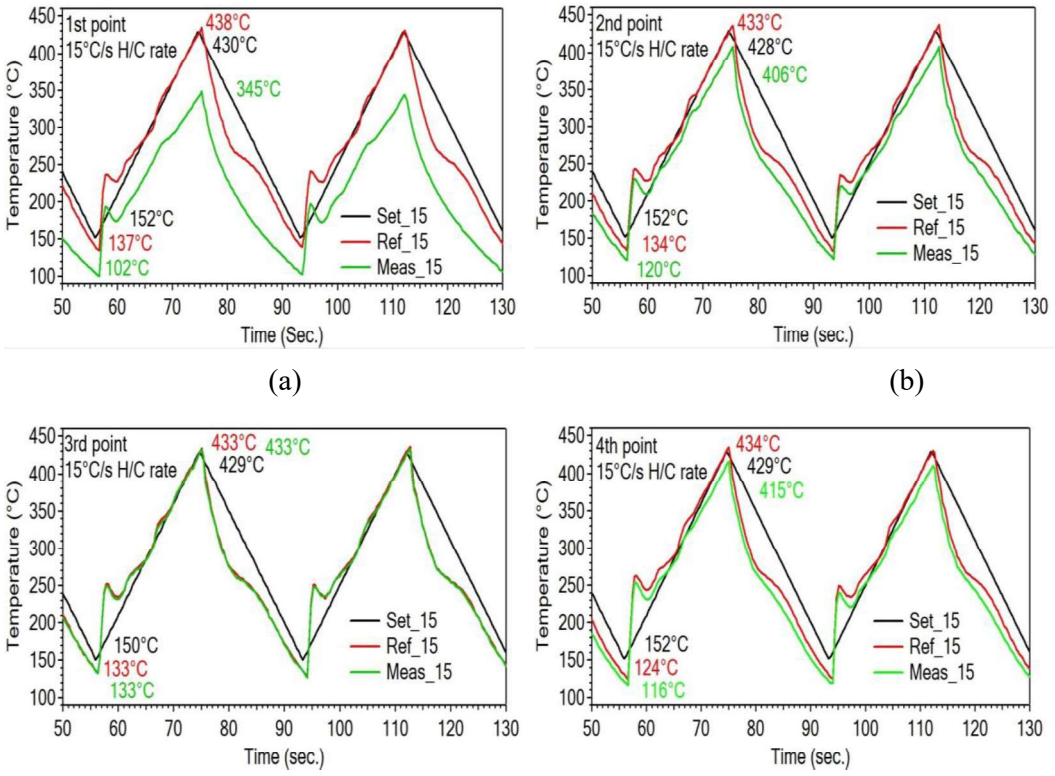

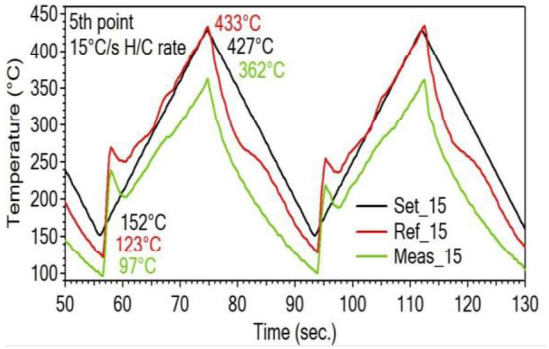

(e)

Figure 4.2-3. Test set temperature, reference temperature and measured temperature comparison for the 5 points through the gage section of the test sample during thermal cycle for 15°C/s heating cooling rate for; (a) point 1, (b) point 2, (c) point 3, (d) point 4 and (e) point 5.

The highest temperature difference between the reference temperatures and measured temperatures during thermal cycling were observed for the top point of the gage section, which is the point 1, in the Figure 4.2-3.a. Therefore, the temperature discrepancy between the mid-top points of gage section during thermal cycling was compared for the 5, 10, 15, 20 and 25°C/s heating cooling rates. The results were represented in Figure 4.2-4. It was observed that the temperature gradients and magnitudes are almost similar for different H/C rates. The highest temperature difference between the points 3 and 1 was observed at the highest temperatures of the thermal cycles while the lowest difference was obtained at the lowest temperatures of the cycles for all H/C rates.

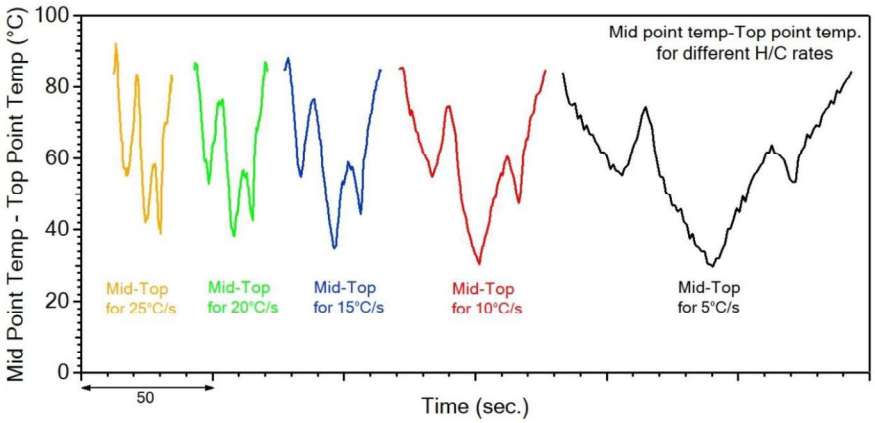

Figure 4.2-4. Temperature difference between the mid and top points of the gage section for different heating cooling rates during thermal cycles.

4.2.3. Infrared Pyrometer Accuracy

The accuracy of the infrared pyrometer was verified with another thermocouple that is attached to the samples which are thermally cycled with very slow rates such as 10°C/min via utilizing the Universal Mechanical Test Machine since the response time to temperature measurement of the thermocouple is very much slower than that of the infrared pyrometer. Therefore, the thermocouple is not able to measure the temperatures instantly when the H/C rates are on the order of °C/s. The thermal cycle was utilized again between 150°C and 430°C, and the surface temp. of the test sample was measured via pyrometer and thermocouple at the same time. Temperature variation between pyrometer controller and thermocouple was about 6°C and the results can be seen in Table 4.2-1. This difference can be accepted as reasonable for two different types of measurement devices.

Table 4.2-1. Temperature measurements with Infrared Pyrometer and Thermocouple.

Temperature Measurements by Thermocouple	**Temperature Measurements by Infrared Pyrometer**
150°C	156°C
206°C	212°C
252°C	258°C

300°C	307°C
351°C	358°C
402°C	409°C
430,5°C	437°C

4.3. Elemental Distribution and Microstructure Analysis

The actuation fatigue behaviors of SMAs are mostly affected by stress amplitude, chemical composition, thermomechanical process history and microstructural evolution, test conditions and surface roughness of test samples as explained in the previous sections [20,23,25]. In the present study, 200 MPa constant stress value was applied in all the actuation fatigue tests and all the specimens were in the same extruded condition. Moreover, the functional fatigue test environment was the same for all the experiments which were conducted using different H/C rates. Although the condition and thermomechanical treatment background of the specimens were the same for all specimens, distinct shape memory properties and actuation fatigue lives were observed for the same H/C rate experiments. Thus, Energy Dispersive Spectrometry (EDS) mapping method was utilized for the elemental distribution analysis of the specimens. The elemental distribution of nickel (Ni), titanium (Ti), hafnium (Hf) and oxygen (O) was obtained by running EDS mapping after conducting functional fatigue test on one of the fatigue specimen and the element maps are presented in Figure 4.3-1. It was seen that the distribution of elements was homogeneous and localization or segregation of elements were not seen through the matrix of the specimen. However, presence of oxygen was also observed in the EDS mappings. Therefore, it can be concluded that chemical composition difference was not the main factor in attaining various SM behaviors such as ΔT, TTs, ε_{act} and $\varepsilon_{austenite}$ and fatigue lives from the actuation fatigue tests that were performed at the same H/C rate.

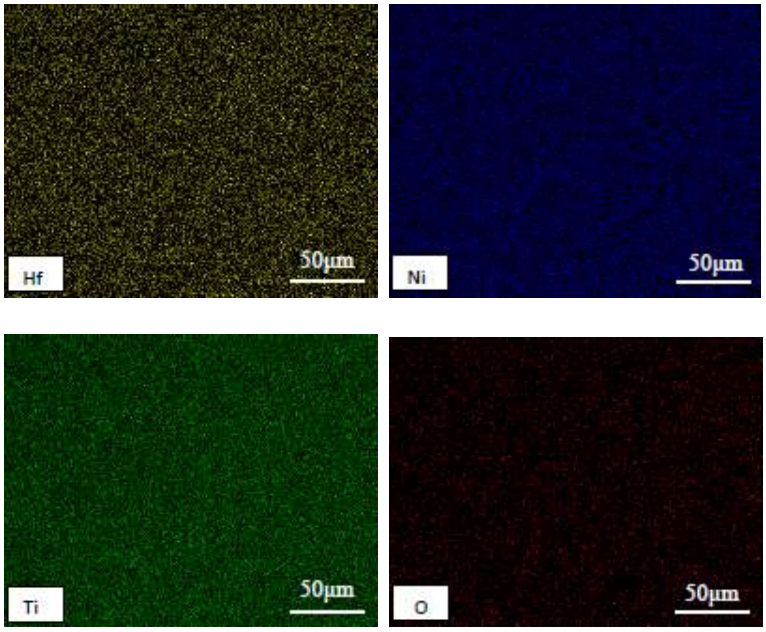

Figure 4.3-1. Energy Dispersive Spectrometry (EDS) mapping images of the hot-extruded $Ni_{50}Ti_{30}Hf_{20}$ HTSMA sample taken after functional fatigue experiment displaying elemental distribution [17].

Additionally, the microstructure of the extruded material was inspected via optical microscope to review the possible oxide formation, deformation variation and flow lines because of hot-extrusion process. Figure 4.3-2 demonstrates the microstructure of the hot extruded sample. Strings of oxides formation were noticeable along grain boundaries as black points through the matrix of the material. The elongated grains with different sizes were also observed leading by deformation variation due to extrusion as shown in the black circles in the presented optical microscope image. As mentioned in the experimental method section, the as-cast NiTiHf was inserted in a mild-steel can and hot-extruded with a 4 to 1 area reduction. The sections close to the edge section of the can represent flow lines and elongated grains. Therefore, it can be concluded that there is a certain deformation variation throughout the cross section of the extruded billet.

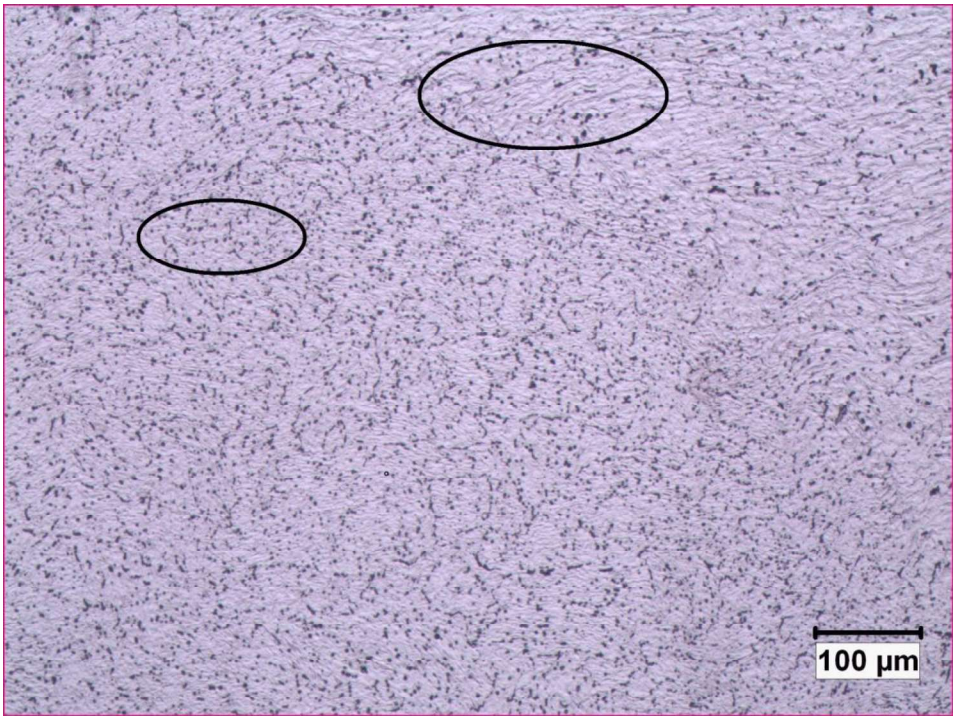

Figure 4.3-2. Optical micrograph image of the extruded $Ni_{50}Ti_{30}Hf_{20}$ HTSMA specimen representing the elongated grains with different sizes and flow lines resulting from deformation variation [17].

4.4. Edge Roughness Control of the Test Sample

As it has been already known that, surface condition of fatigue test specimens is also a substantial parameter for the fatigue lifetime of the materials [128]. Surface roughness is the source of stress concentration on the material and induces crack initiation, and leads to observe early failure. The surfaces of the fatigue test samples are actually polished before the experiments but the side surfaces in other term the edges of the test specimens were not examined via considering the probable influence of surface roughness on the fatigue lifetime. The optical microscope images obtained from the edges of the test specimens before edge grinding were represented in the Figures starting from 4.4-1.a to 4.4-1.c. The edge roughness throughout the gage section of the sample can be seen in the optical images wşth different scales as indicated in the red circles. Figures 4.4-1.d, 4.4-1.e and 4.4-1.f display the images that were obtained after edge grinding/polishing of the same sample. The microcracks due to rough surface were

mitigated by the grinding of the edges. All the functional fatigue tests, which were exhibited previously, were performed without edge grinding of the specimens and the maximum fatigue life in the hot-extruded condition before grinding of the edges was attained as 1738 cycles from the experiment that was run with 15°C/s heating and cooling rate.

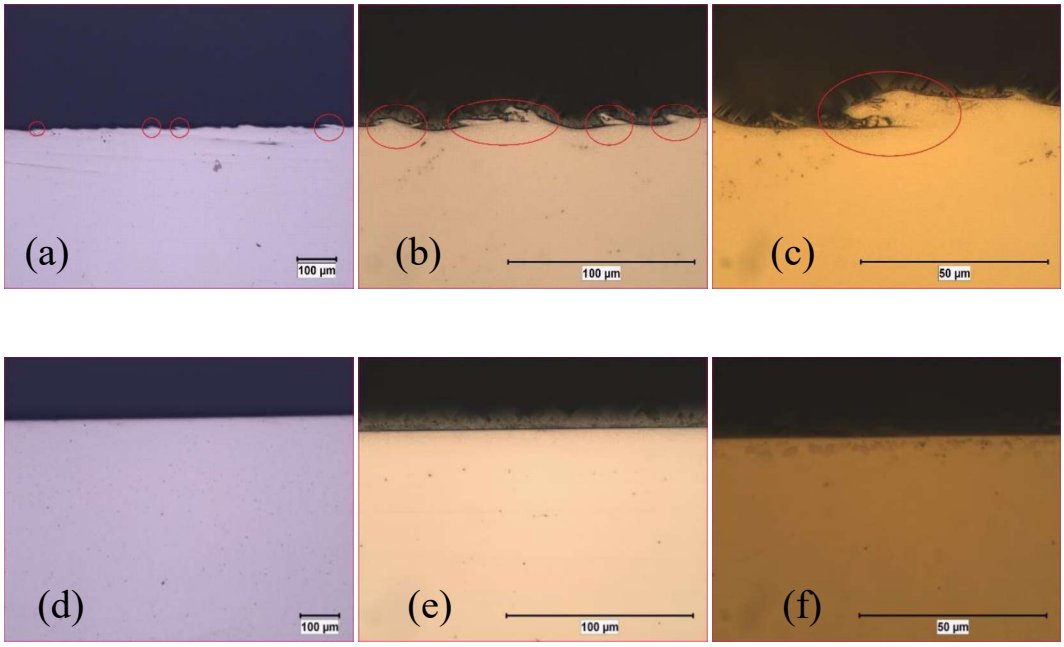

Figure 4.4-1. Optical microscope images of the hot-extruded $Ni_{50}Ti_{30}Hf_{20}$ dog bone shaped specimens representing edge microcracks due to rough surface; (a) - (c) before grinding and (d) - (f) after grinding [17].

4.5. Discussion of Results

It is worth to remind that $Ni_{50}Ti_{30}Hf_{20}$ (at.%) HTSMA was extruded at 900°C for 4:1 area-reduction-ratio. The operation of hot-extrusion was applied to remove the possible microstuctural and chemical inhomogeneities due to casting process. The functional fatigue test specimens were cut from the extruded billet by using WEDM and randomly chosen for fatigue experiments. Thermal cycling under 200 MPa constant stress were performed on these randomly selected extruded specimens for different H/C rates. The ε vs T curves and shape memory properties which were drawn from these curves were

exhibited in the Figures 4.1-2, 4.1-3 and 4.1-4. It was seen that even the H/C rate and the upper cycle temperature (UCT) were the same in the functional fatigue tests, different TTs, thermal hysteresis, actuation and accumulated irrecoverable strain properties were obtained. Additionally, the specimens which were thermally cycled under the same H/C rate and UCT exhibited various fatigue lives such as 1738, 754 and 580 cycles as shown in Table 4.1-2. Because of all these observations, chemical compositional difference analysis via EDS mapping were conducted in order to analyze the distribution of Ni, Ti and Hf elements. Oxygen was also detected in EDS mapping analysis because oxygen affinities of NiTiHf alloys are very high. It was observed in Figure 4.3-1 that the elements distributed homogeneously in the alloy. So it can be concluded that the chemical difference in the samples cannot be the reason in obtaining various SM behaviors and functional fatigue lives in thermal cycling experiments which were conducted under the identical test conditions.

On the other hand, deformation variation induced by hot extrusion which was displayed in Figure 4.3-2 may cause to get various fatigue lives and shape memory behavior from the thermal cycling tests of randomly selected extruded specimens. The elongated grains and flow lines were seen along certain directions but the direction and dimensions of the elongated grains were not the same as shown with the black circles in Figure 4.3-2. The oxides were also determined throughout the microstructure as the black points in different sizes.

Additionally, it is known in the literature that surface roughness is one the main sources to increase the stress concentration and causes to crack initiation and propagation. Since the surface roughness was considered as one of the primary reasons to obtain low functional fatigue life from randomly selected extruded specimens, the side surface polishing of the specimens with edge grinding was taken into consideration in the presented study. Therefore, the edge grinding was conducted on the surface of the fatigue specimens for further investigations to be able to standardize the actuation fatigue experiments.

4.6. Deformation Variation Analysis with Enumerated Samples

The functional fatigue tests were thereafter conducted again on the samples which were edge ground through the gage section. It was suspected that the deformation variation, which was observed in the microstructural analysis of the extruded material, through the cross section of the extruded material may lead to obtain dissimilar SM properties in the studied alloy [28], so the edge ground samples were enumerated before the fatigue experiments as stated in the experimental methods section. As a matter of fact that the fatigue experiment conditions such as experiment setup and parameters were identical for all the tests represented previously, thus it can been expressed that the experiment conditions have been already standardized. To be able to assure the sample standardization in addition to experiment condition standardization, the edge roughness wasmitigated via edge grinding. Additionally, the hot-extruded specimens, which were cut by WEDM, were enumerated along the cross section and then the fatigue experiments were run to examine the influence of edge roughness and deformation variation through the cross section of the hot-extruded billet.

4.6.1. Functional Fatigue Tests of Enumerated Samples

The ε vs T diagrams that were attained from six functional fatigue experiments of the enumerated extruded samples after edge grinding were presented in Figures starting from 4.6-1.a to 4.6-1.f. All these experiments were conducted with 15°C/s heating and cooling rate because the test setup cannot manage thermal cycles properly for higher or lower rates as mentioned in the experimental methods section. It can be deduced from strain vs temperature graphs that the edge ground specimens that were enumerated exhibited relatively higher fatigue lives compared to the randomly selected specimens yet they still showed different functional behaviors. Please note that the numbering the sample system was shown in the Experimental Method section.

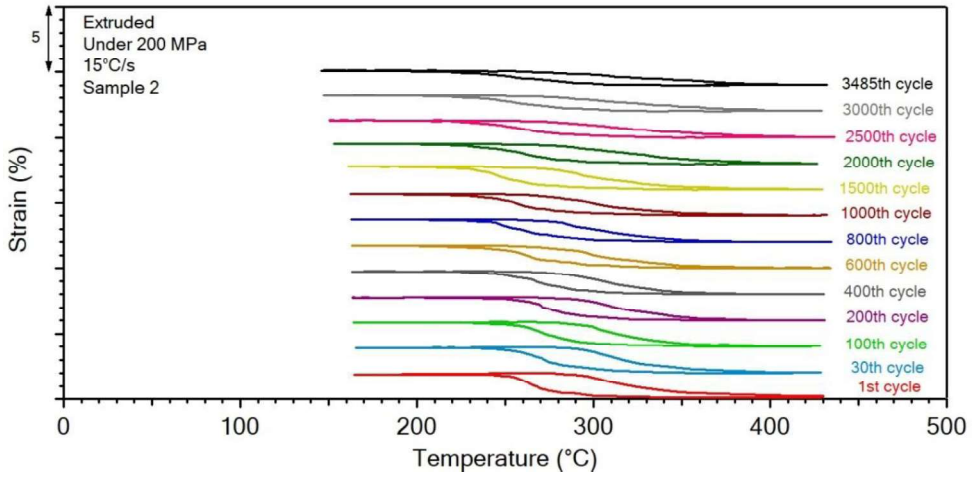
Extruded
Under 200 MPa
15°C/s
Sample 2
5
Strain (%)
3485th cycle
3000th cycle
2500th cycle
2000th cycle
1500th cycle
1000th cycle
800th cycle
600th cycle
400th cycle
200th cycle
100th cycle
30th cycle
1st cycle
0
100
200
300
400
500
Temperature (°C)

(a)

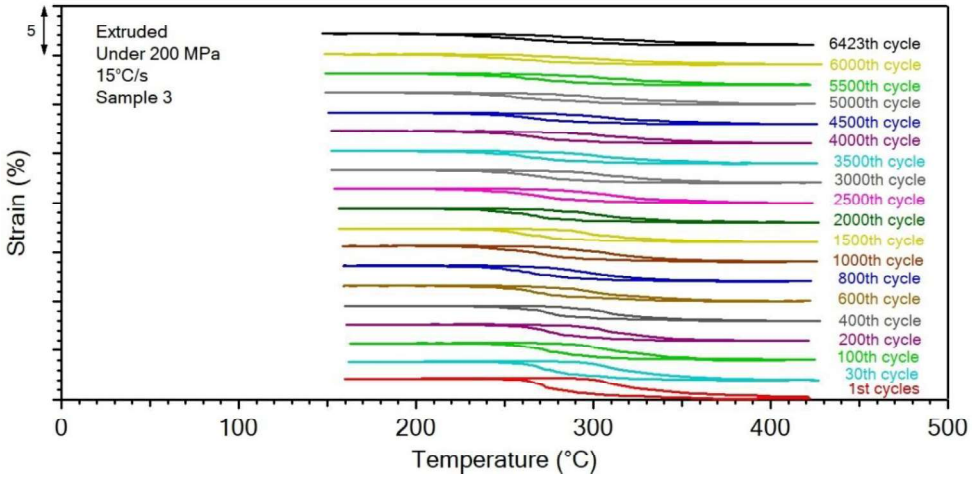
Extruded
Under 200 MPa
15°C/s
Sample 3
5
Strain (%)
6423th cycle
6000th cycle
5500th cycle
5000th cycle
4500th cycle
4000th cycle
3500th cycle
3000th cycle
2500th cycle
2000th cycle
1500th cycle
1000th cycle
800th cycle
600th cycle
400th cycle
200th cycle
100th cycle
30th cycle
1st cycles
0
100
200
300
400
500
Temperature (°C)

(b)

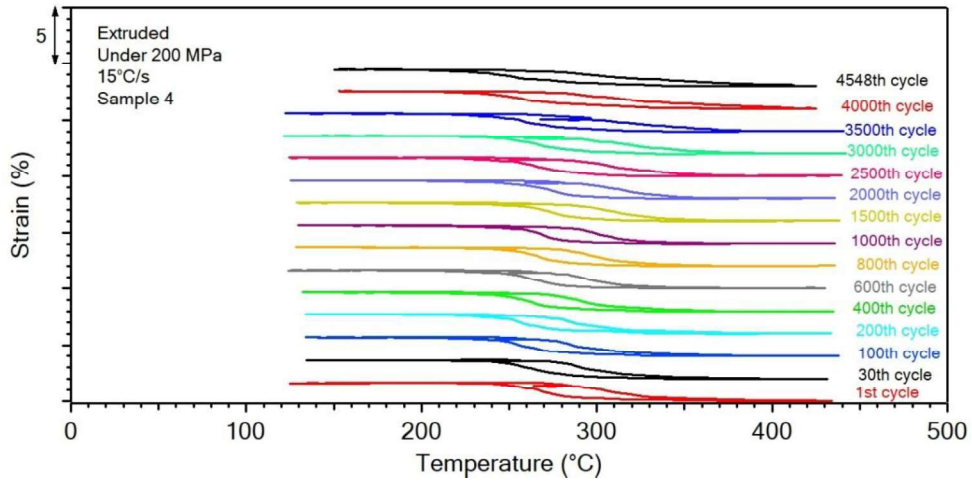
Extruded
Under 200 MPa
15°C/s
Sample 4
5
Strain (%)
4548th cycle
4000th cycle
3500th cycle
3000th cycle
2500th cycle
2000th cycle
1500th cycle
1000th cycle
800th cycle
600th cycle
400th cycle
200th cycle
100th cycle
30th cycle
1st cycle
0
100
200
300
400
500
Temperature (°C)

(c)

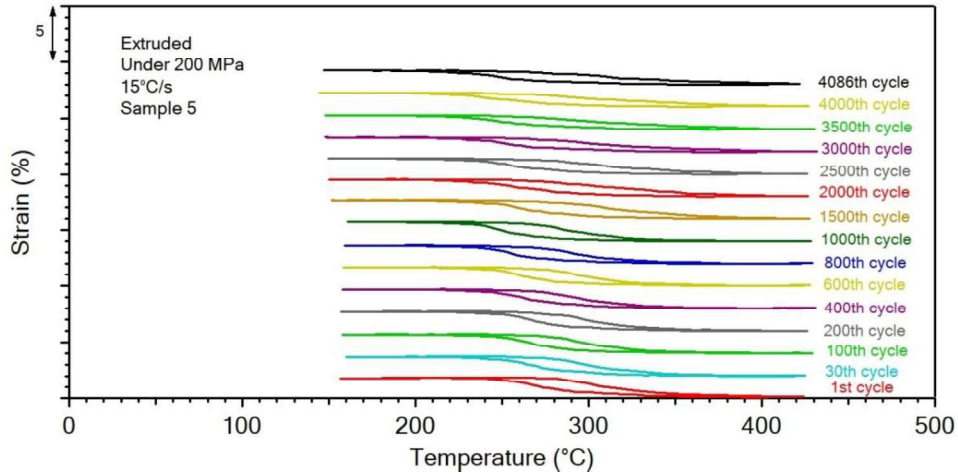
5
Extruded
Under 200 MPa
15°C/s
Sample 5
Strain (%)
4086th cycle
4000th cycle
3500th cycle
3000th cycle
2500th cycle
2000th cycle
1500th cycle
1000th cycle
800th cycle
600th cycle
400th cycle
200th cycle
100th cycle
30th cycle
1st cycle
0
100
200
300
400
500
Temperature (°C)

(d)

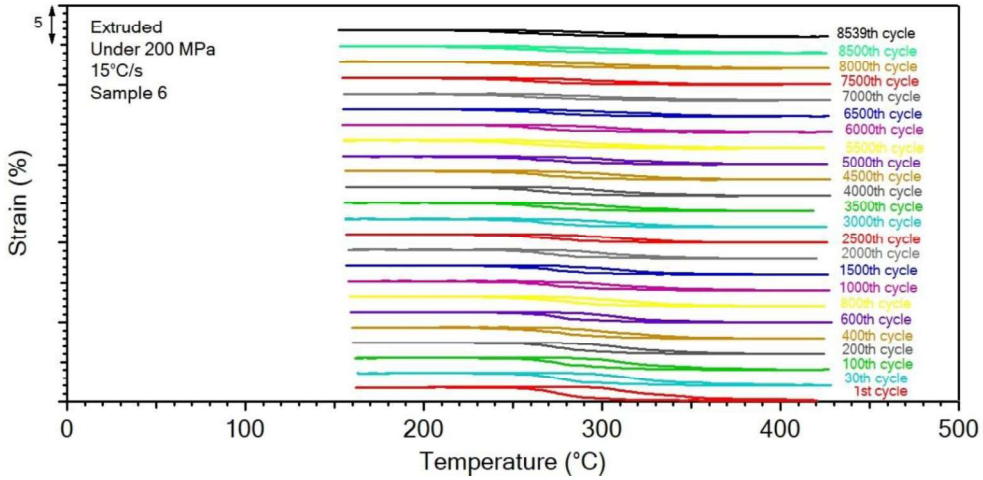
5
Extruded
Under 200 MPa
15°C/s
Sample 6
Strain (%)
8539th cycle
8500th cycle
8000th cycle
7500th cycle
7000th cycle
6500th cycle
6000th cycle
5500th cycle
5000th cycle
4500th cycle
4000th cycle
3500th cycle
3000th cycle
2500th cycle
2000th cycle
1500th cycle
1000th cycle
800th cycle
600th cycle
400th cycle
200th cycle
100th cycle
30th cycle
1st cycle
0
100
200
300
400
500
Temperature (°C)

(e)

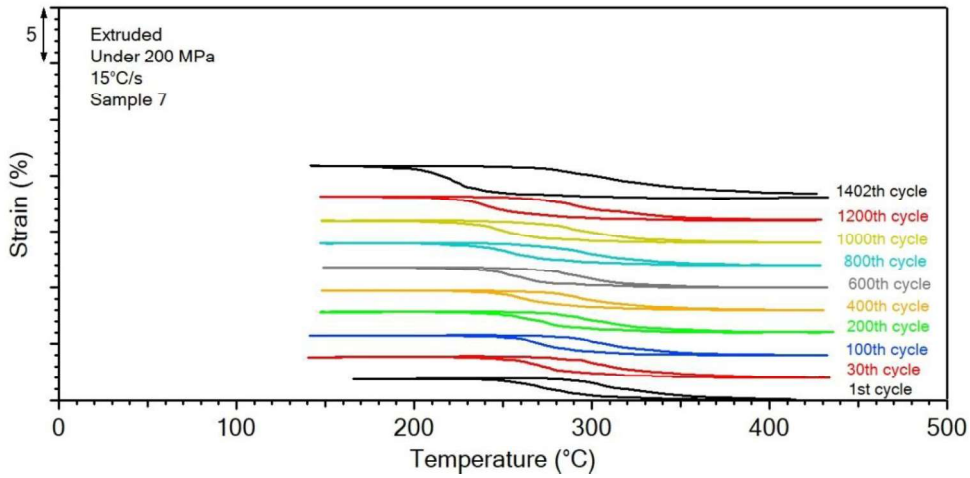
5
Extruded
Under 200 MPa
15°C/s
Sample 7
Strain (%)
1402th cycle
1200th cycle
1000th cycle
800th cycle
600th cycle
400th cycle
200th cycle
100th cycle
30th cycle
1st cycle
0
100
200
300
400
500
Temperature (°C)

(f)

Figure 4.6-1. ε vs T curves attained from the functional fatigue experiments of the enumerated hot-extruded samples after edge grinding; (a) sample 2, (b) sample 3, (c) sample 4, (d) sample 5, (e) sample 6 and (f) sample 7 [17].

Even though six specimens were obtained from the same batch of extruded alloy, it was seen that they showed different fatigue lives as seen in Table 4.6-1 because of the deformation variation throughout the cross section of the hot-extruded material. The lowest fatigue lives were observed for the samples 2 and 7 as 3485 and 1402 cycles, respectively. The samples 3 and 6 exhibited the longest functional fatigue lives as 6423 and 8539 cycles, respectively. The numbers of the symmetrical samples were shown in the experiment methods section but it would be better to remind that the samples 3 and 6 and also the samples 2 and 7 are symmetrical ones considering the cross section of the hot-extruded billet.

Table 4.6-1. Functional fatigue life results attained from functional fatigue tests for 15°C/s H/C rate on the enumerated hot-extruded $Ni_{50}Ti_{30}Hf_{20}$ HTSMA samples [17].

Samples with Numbers	**Functional Fatigue Life**
Sample 2	failed at 3485th cycle
Sample 3	failed at 6423rd cycle
Sample 4	failed at 4548th cycle
Sample 5	failed at 4086th cycle
Sample 6	failed at 8539th cycle
Sample 7	failed at 1402nd cycle

The evolution of M_s and A_f TTs, ΔT, ε_{act} and $\varepsilon_{austenite}$ with the number of cycles of the six enumerated samples from 2 to 7 were represented in Figures starting from 4.6-2.a to 4.6-2.d, respectively. These data were obtained from the ε vs T graphs of the six enumerated samples which were exhibited in Figure 4.6-1. Only A_f and M_s temperatures are shown in Figure 4.6-2.a to clearly display the TTs evolution with the cycle numbers and to be able to prevent complicated presentation of the data in a graph.

It was seen in the Figure 4.6-2.a that the enumerated specimens showed similar A_f and M_s transformation temperatures up to 1000 cycles. After 1000 cycles, M_s temperature decreased and A_f temperature rapidly increased with increasing cycle numbers for the sample 7 which was failed at 1402^{nd} cycle. This was the lowest fatigue life that was observed compared to the other enumerated samples. The second lowest functional fatigue life was 3485 cycles that was obtained for the sample 2 which was the symmetrical sample of the sample 7. The samples 3 and 6 and the samples enumerated as 4 and 5 which were accepted as symmetrical samples via considering their locations where they were obtained from the cross section of the hot-extruded billet. The samples numbered as 4 and 5 presented relatively stable A_f and M_s transformation temperatures and failed at 4548th and 4086th cycles, respectively. The most stable transformation temperatures manner and the highest cycle number were attained with the samples 3 and 6 which were failed at 6423th and 8539th cycles, respectively. Hence, it can be deduced from the evolution of TTs of the symmetrical specimens were observed to be similar; nevertheless, the TTs of all enumerated specimens varied under the same experiment conditions.

As explained in the literature, large internal stress is induced and elastic strain energy increases by loading the samples which promote the reverse transformation [127], so ΔT diminishes with increasing cycle numbers for all the numerated samples at the beginnings as seen in figure 4.6-2.b. The thermal hysteresis values were in close range for all numerated samples as a function of cycle numbers for the first 1000 cycles similarly to the behavior of TTs. While the ΔT of the sample 7 demonstrated rapid increase since the temperature of forward transformation decreased and that of the reverse transformation increased, the samples number 2, 4 and 5 exhibited pretty similar and smooth incremental trend after 1000 cycles. The most stable thermal hysteresis behavior was observed with the samples 3 and 6 likewise to TTs.

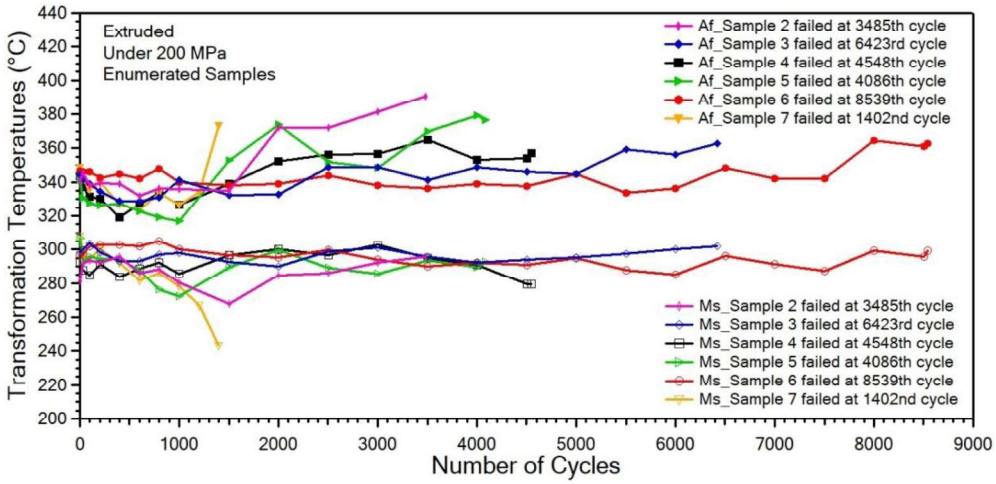
Extruded
Under 200 MPa
Enumerated Samples
Af_Sample 2 failed at 3485th cycle
Af_Sample 3 failed at 6423rd cycle
Af_Sample 4 failed at 4548th cycle
Af_Sample 5 failed at 4086th cycle
Af_Sample 6 failed at 8539th cycle
Af_Sample 7 failed at 1402nd cycle
Ms_Sample 2 failed at 3485th cycle
Ms_Sample 3 failed at 6423rd cycle
Ms_Sample 4 failed at 4548th cycle
Ms_Sample 5 failed at 4086th cycle
Ms_Sample 6 failed at 8539th cycle
Ms_Sample 7 failed at 1402nd cycle
Transformation Temperatures (°C)
Number of Cycles

(a)

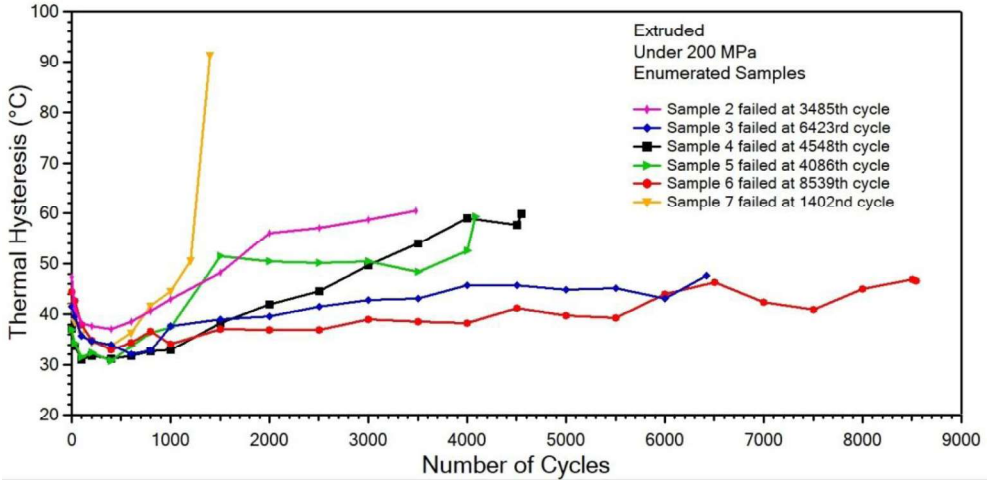
Extruded
Under 200 MPa
Enumerated Samples
Sample 2 failed at 3485th cycle
Sample 3 failed at 6423rd cycle
Sample 4 failed at 4548th cycle
Sample 5 failed at 4086th cycle
Sample 6 failed at 8539th cycle
Sample 7 failed at 1402nd cycle
Thermal Hysteresis (°C)
Number of Cycles

(b)

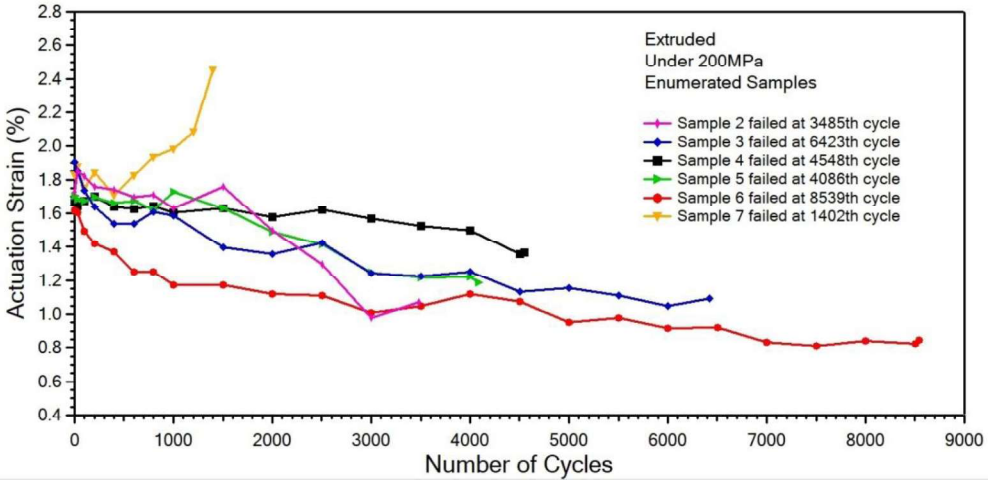
Extruded
Under 200MPa
Enumerated Samples
Sample 2 failed at 3485th cycle
Sample 3 failed at 6423th cycle
Sample 4 failed at 4548th cycle
Sample 5 failed at 4086th cycle
Sample 6 failed at 8539th cycle
Sample 7 failed at 1402th cycle
Actuation Strain (%)
Number of Cycles

(c)

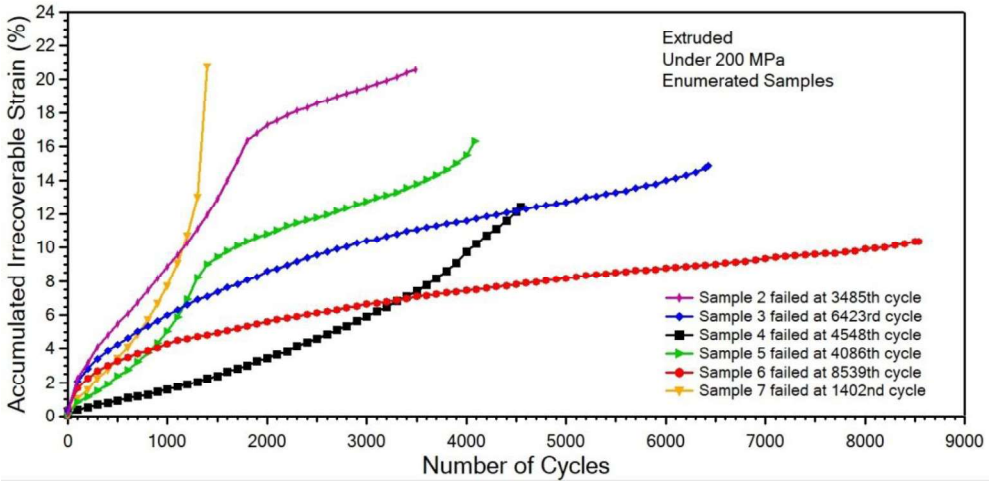

(d)

Figure 4.6-2. (a) M_s and A_f TTs, (b) ΔT, (c) ε_{act} and (d) $\varepsilon_{austenite}$ evolution with the cycle numbers drawn from the functional fatigue tests of six enumerated specimens [17].

Figure 4.6-2.(c) represents the ε_{act} evolution of the enumerated samples and it can be deduced that ε_{act} of sample 7 sharply escalated with the increase cycle numbers and approached to the largest ε_{act} value of about 2.5%. This sample also exhibited the lowest functional fatigue life. Moreover, it is important to state that, the samples were coated with a high-temp. black paint for measuring the temperature values of the specimens correctly by infrared pyrometers as mentioned in the experimental methods section. Sometimes, the black paint peels off the specimen surface with the influence of high temperature which causes the infrared pyrometer to read inaccurate temperature values. So, the specimen can be heated up to elevated temperatures by the reason of the inaccurate temperature measurements which are sent to the PID controller. The drastic increase in ε_{act} might create more expansion-contraction of microcracks which led faster crack-propagation and resulted to decrease in fatigue performance [13]. Stable actuation strain behavior was observed for sample 4 with increasing the number of cycles. Samples 3-5 showed almost stable actuation strain values until 1000^{th} cycle and then decreased discernibly up to failure. However, decreasing actuation strain trend was observed from the beginning up to failure for samples 3 and 6 and sample 6

demonstrated the lowest actuation strain values but the highest actuation fatigue life than that of the other enumerated specimens.

The accumulated irrecoverable strain evolution during thermal cycling with respect to number of cycles for the six enumerated samples were exhibited in Figure 4.6-2.d. The $\varepsilon_{austenite}$ values of all samples continued to increase and did not saturate until the end of the experiments. The $\varepsilon_{austenite}$ of the outermost specimens considering the cross section of the extruded billet which were samples 2 and 7, was accumulated rapidly and presented the largest values. Necking and high elongation were also observed for samples 2 and 7 during heating and cooling cycles under constant stress. Samples 4 and 5 exhibited relatively less accumulated irrecoverable strain and elongation compared to that of the specimens 2 and 7. The lowest elongation after failure was observed for samples 3 and 6 and led to obtain the highest functional fatigue lives.

4.6.2. Microstructural Analysis of Enumerated Samples

Figure 4.6-3 displays the optical microscopic images that were obtained from the cross-sectional areas of the hot-extruded billet from which the 2nd, 3rd, 6th and 7th specimens were sliced for the actuation fatigue tests. It is worth to recall that the sections of the enumerated samples were previously shown in the experimental methods section. It was observed from the exhibited optical microscopic images that for specimens 3 and 6 in Figure 4.6-3.b and Figure 4.6-3.c that the metal flow lines are more distinct and these specimens have homogenous microstructure compared to the samples enumerated with 2 and 7 as seen in Figures 4.6-3.a and d. Since the material was exposed to different deformation magnitudes due to extrusion process and there might be temperature gradient through the cross section during the hot-extrusion process, non-homogeneous microstructure and flow variance along the cross-section of the billet were obtained. Thus, the functional properties of the alloy were eventually affected from these parameters and variations.

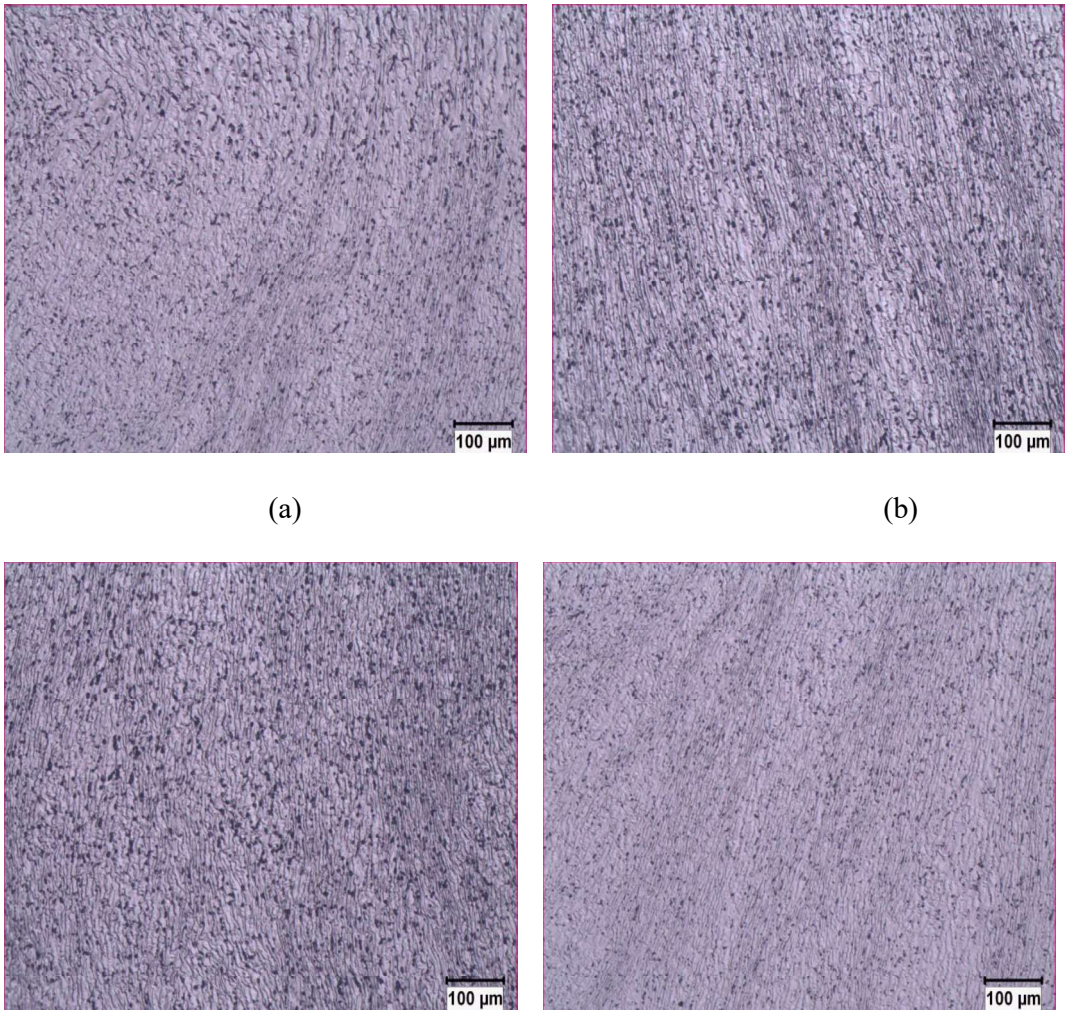

Figure 4.6-3. Optical images which were obtained from the cross-sectional area of the extruded billet where the second, third, sixth and seventh specimens were cut out (a) sample 2, (b) sample 3, (c) sample 6 and (d) sample 7 [17].

4.6.3. Discussion of Results for Enumerated Samples

As mentioned in the edge roughness control of the test sample section, the edges of the randomly selected fatigue specimens were not ground but those of the enumerated dog bone shaped fatigue specimens were ground before functional fatigue tests. The optical microscope images taken from the edges of randomly selected samples without edge grinding and enumerated samples ground before experiments were presented in Figure

4.4-1 which exhibited the influence of edge grinding process. As displayed in Figures 4.4-1.d to Figure 4.4-1.f, smooth edge surfaces were observed for the enumerated specimens and it was seen that the actuation fatigue lives of the material enhanced after edge grinding. This increase was attained without taking the specimen enumeration into account. While sample 7 failed at 1402 cycles, sample 6 exhibited the highest number of cycles that was 8539 cycles. The edges of dog bone shaped randomly selected specimens were not ground, thus the fatigue life cycles were obtained to be as low as 500 cycles such as 481 and 580 cycles. The enhancement in the cycle numbers in fatigue tests was attributed to the reduction in the stress concentration owing to edge roughness by obtaining smooth edges via applying grinding.

Furthermore, Figures 4.6-3.a to Figures 4.6-3.d represent the optical microscope images which were taken from the cross-sectional regions of the extruded billet where the 2^{nd}, 3^{rd}, 6^{th} and 7^{th} fatigue specimens were cut out. Microstructural variation in the hot-extruded billet was determined along the cross section. It is significant to remind that the samples 2 and 7 and the samples 3 and 6 are symmetrical specimens as previously shown in Figure 3.3-1.b. The microstructures of 3rd and 6th samples are relatively finer and homogenous than those of the 2nd and 7th ones. It has been already known that metal alloys with finer and homogenous microstructure result better mechanical properties. Hence, this may led to observe longer fatigue cycles and lower accumulated irrecoverable strain values from specimens 3 and 6 compared to the other numerated specimens.

Even though the fatigue life of the alloys was improved after edge grinding, different SM properties such as TTs, ΔT together with ε_{act} and $\varepsilon_{austenite}$ which were attained from thermal-cycling-experiments of six enumerated specimens were observed depending upon the specimen locations through the cross section of the hot-extruded billet. Both the magnitudes of the shape memory properties and the increment or the decrement trends of the properties with the increase in the cycle numbers were distinct as shown in Figures 4.6-2.a to Figures 4.6-2.d. For example, the decreasing trend in ε_{act} values for 6^{th} sample was seen to be more than that of 2^{nd} , 5^{th} and 7^{th} samples with increasing the cycle numbers. The lowest ε_{act} magnitudes along the thermal cycles were observed for

the 6th sample and the highest fatigue cycle was achieved due to the lowest actuation strain values. Furthermore, the rapid increase in actuation and accumulated irrecoverable strain magnitudes of specimen 7 was observed which was represented in Figures 4.6-2.c and d, and it is important to clarify this unusual behavior. As mentioned previously, the gage section surfaces of all specimens were coated with a HT resistant black paint before functional fatigue tests, thus it could be possible to measure and attain the sample temperature data during thermal cycling experiments. Nevertheless, if this black paint is not sprayed homogenously on the sample surface, it can be stripped since the specimen is exposed to elevated temperatures during experiment. Therefore, the temperature cannot be measured correctly from the surface of the specimen and the thermal cycling rate cannot be close controlled. Due to this lack of control, the specimen can be heated up to a higher temperatures than that of the predetermined upper cycle temperature. It was noticed after running the thermal cycling experiment that the black-paint peeled off from the 7th sample. Hence, 7th sample was likely heated up to higher temperatures than the predetermined upper cycle temperature which caused to obtain higher accumulated strain values because of probable creep deformation at elevated temperatures. Additionally, heating the specimen to higher temperatures than the predetermined UCTs can also be the possible reason for observing higher ε_{act} values due to leading to attain larger volume of martensitic phase transformation.

4.7. The Effect of Annealing Heat Treatment

The enumerated samples which were cut from different locations through the cross sectional area of the hot-extruded billet exhibited dissimilar shape memory properties from the functional fatigue tests. Hence, it can be briefly concluded that hot-extrusion process with 4 to 1 area reduction could not fully overcome the deformation variation of the material. Additionally, induced stress with hot extrusion may not be uniform as well. To tackle with these problems, annealing heat treatment at 550°C-3h was applied to the extruded material to remove the deformation variation and relieve the inhomogeneous stress distribution.

4.7.1. DSC Analysis of Annealed Samples

First of all, stress free TTs of the extruded and annealed samples were gathered with the DSC experiments. Figure 4.7-1 displays the DSC curves of both conditions. The TTs, thermal-hysteresis ($A_f - M_s$) and the ΔH obtained from these curves are represented in Table 4.7-1. M_s,M_f,A_s and A_f TTs and ΔHs of the extruded and annealed samples were nearly the same as it was explicitly shown in the following figure and table.

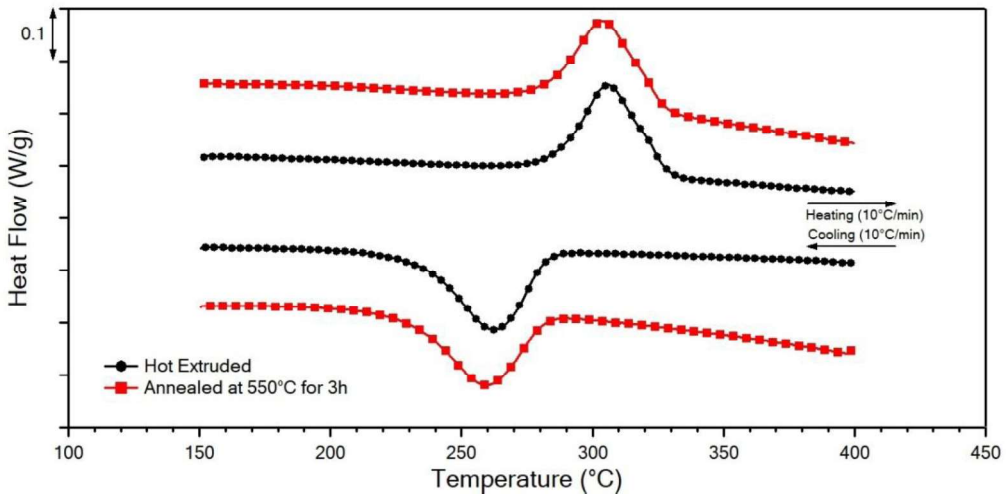

Figure 4.7-1. DSC results of extruded $Ni_{50}Ti_{30}Hf_{20}$ (at.%) and annealed at 550°C for 3h samples [17].

Table 4.7-1. Stress free TTs, ΔT (°C) and ΔH of extruded and annealed specimens taken from DSC graphs [17].

	Hot Extruded	**Annealed**
A_f (°C)	330	328
A_s (°C)	286	281
M_s (°C)	282	282
M_f (°C)	236	229
Thermal Hysteresis	48	46

(A_f-M_s) (°C)		
Transformation Enthalpy (J/g) ($\Delta H_{cooling}$)	26.72	27.39

4.7.2. Functional Fatigue Tests of Annealed Specimens

One fatigue specimen from the outermost section and the other one from the middle section of the hot-extruded billet were cut from the same extruded material and numerated as sample 2 and 5, respectively. It is worth to note that similar to the enumerated extruded samples, edge grinding was conducted to both of the annealed specimens before fatigue experiments. Then, actuation fatigue tests were also performed on both annealed specimens under 200 MPa constant stress level with 15°C/s H/C rates. Thermal cycles were utilized between 150°C and 430°C just as in the previous fatigue experiments and ε vs T graphs of these experiments are presented in Figures 4.7-2.a and b. While sample 2 failed at 11942th cycle, 5th sample that was cut from the mid section of the extruded material failed at 10622th cycle as can be seen in the Figures and highest number of cycles were achieved from these experiments which were conducted on the annealed samples.

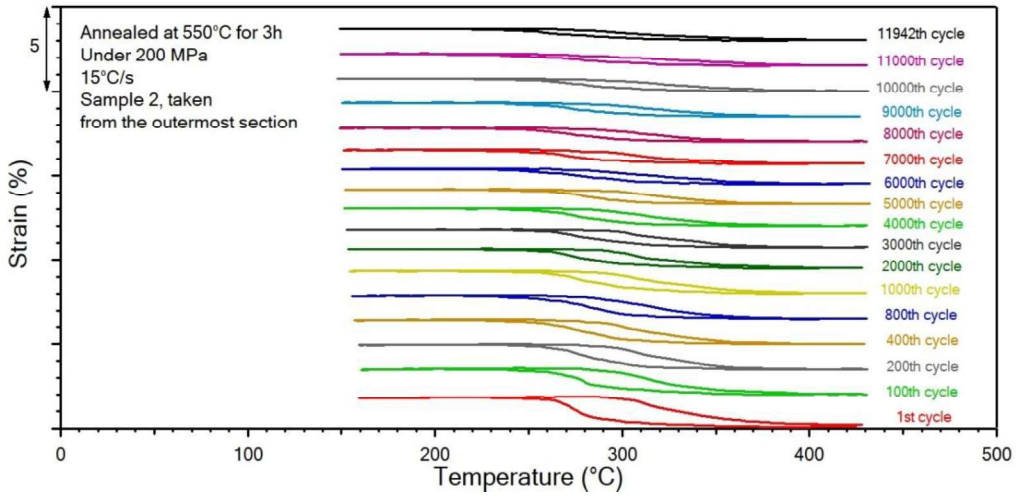

(a)

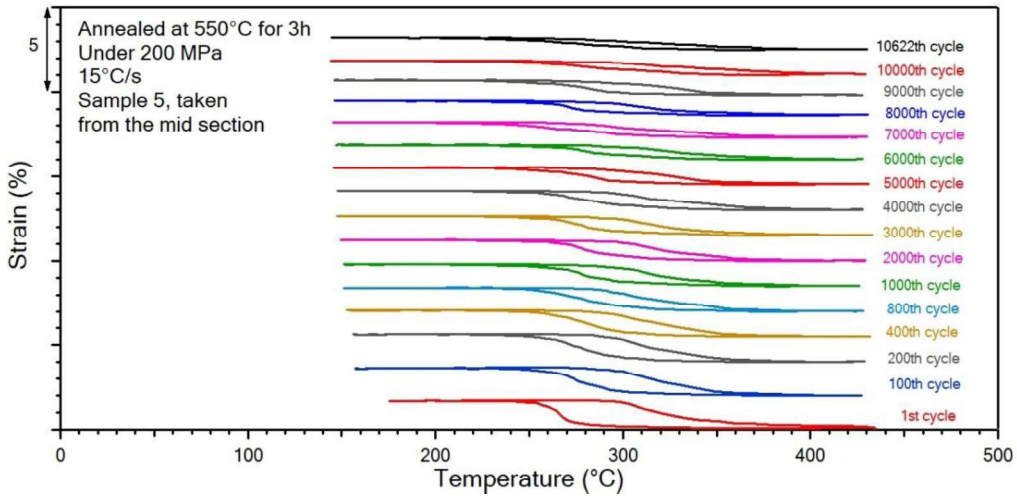

(b)

Figure 4.7-2. ε vs T responses attained from the functional fatigue experiments of the annealed at 550°C-3h samples after edge grinding; (a) sample 2 and (b) sample 5 [17].

Functional fatigue properties of both annealed samples were examined and TTs such as M_s, M_f, A_s and A_f temperatures, ΔT, actuation and accumulated irrecoverable strain evolution with increasing cycle numbers are were illustrated in Figures starting from 4.7-3.a to 4.7-3.d, respectively. A small increase in the A_f and M_s TTs and a small decrease in the A_s and M_f TTs were observed throughout the cycle numbers as illustrated in Figure 4.7-3.a. Thus, it can be concluded that the forward and reverse TTs were nearly stabilized with annealing heat treatment. Another impressive observation is that the TTs of both of the annealed specimens were almost the same with the increment in the cycle numbers. Thermal hysteresis of the annealed specimens decreased at the beginning similar to the previous experiments for the extruded materials and then slightly increased till failure for both of the annealed samples as illustrated in Figure 4.7-3.b. Additionally, thermal hysteresis values of these specimens were considerably the same compared to the enumerated and randomly selected hot-extruded samples.

The ε_{act} magnitudes with increasing the cycle numbers of two annealed specimens were the same as shown in Figure 4.7-3.c. In addition, the ε_{act} of both of the annealed

specimens declined from 1.6% down to about 0.8% values during the thermal cycles under constant stress. Figure 4.7-3.d displays the accumulated irrecoverable strain evolution of two annealed samples and the $\varepsilon_{austenite}$ values increased up to 7.6% and 8.9% for the samples 2 and 5, respectively. Both of the annealed samples exhibited lower $\varepsilon_{austenite}$ strain magnitudes than that of the extruded 6th sample which demostrated the lowest $\varepsilon_{austenite}$ strain among the other enumerated and randomly selected extruded samples and more importantly the higher functional fatigue life than that of all the extruded samples.

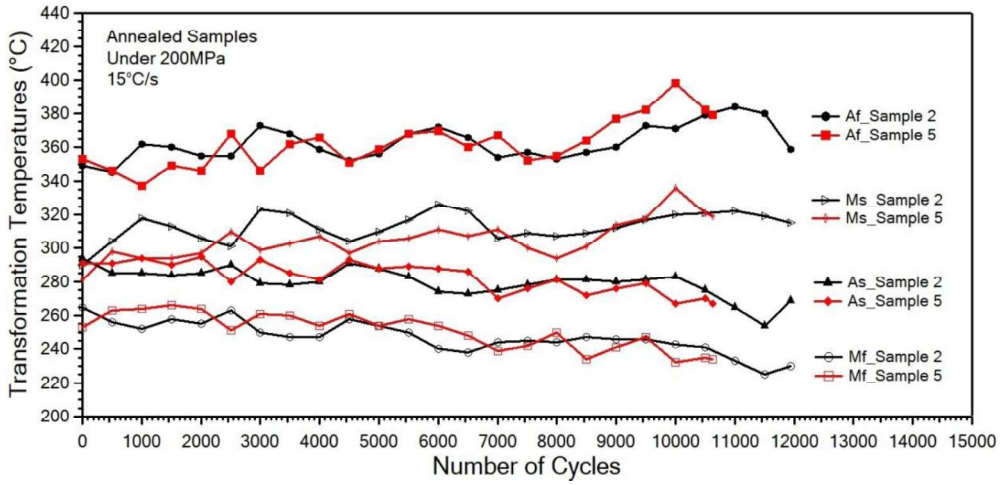

(a)

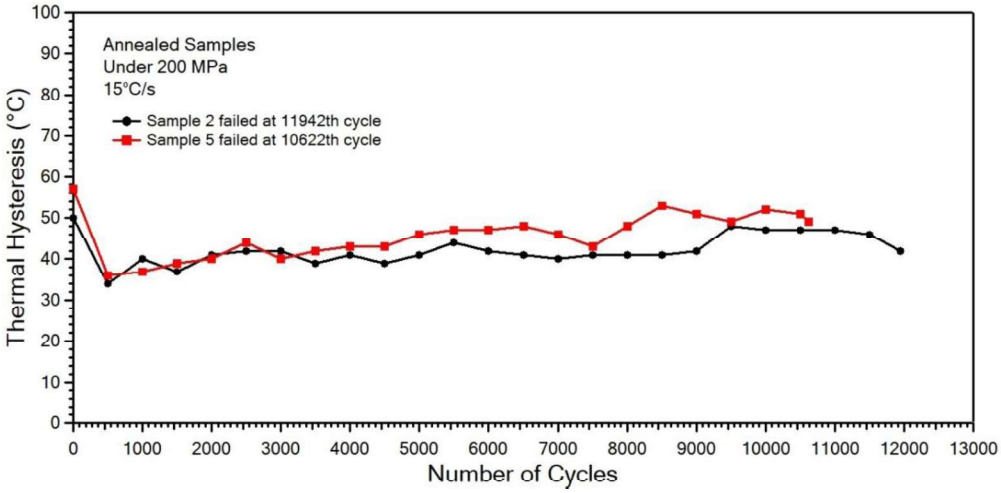

(b)

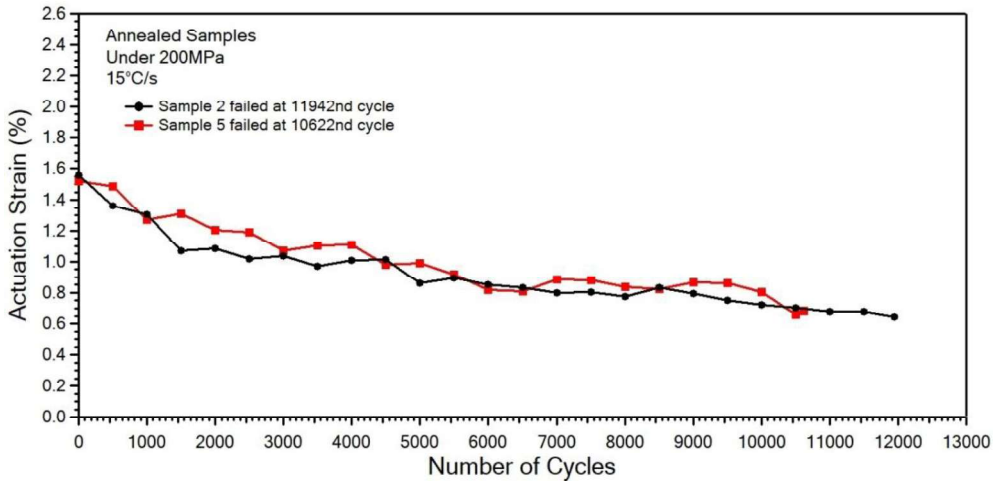

(c)

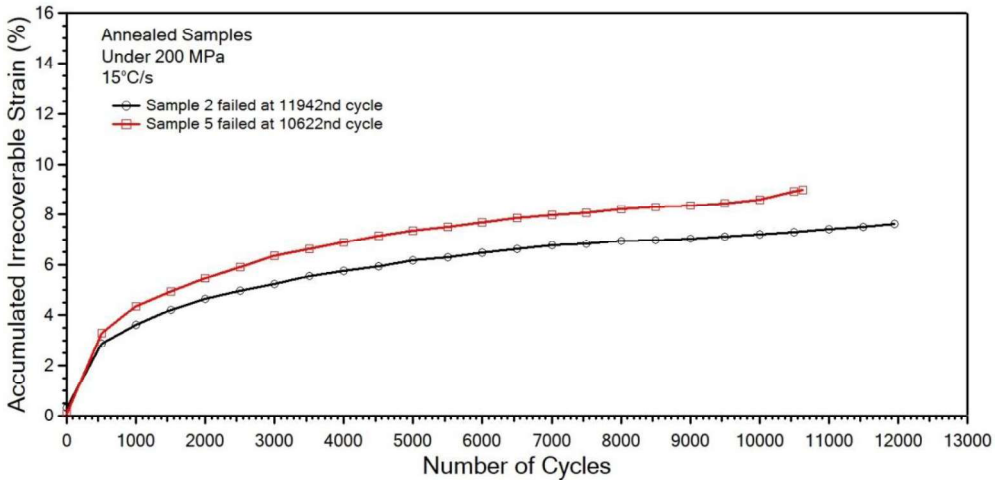

(d)

Figure 4.7-3. (a) TTs, (b) ΔT, (c) ε_{act} and (d) $\varepsilon_{austenite}$ evolution with the cycle cumbers drawn from the functional fatigue tests of two annealed samples [17].

4.7.3. Microstructural Analysis of Annealed Samples

The microstructure of annealed specimens were also analyzed via the optical microscope to figure out the possible reasons for attaining the uniform actuation fatigue properties after applying annealing heat treatment to the extruded material. Optical microscope images which were obtained from annealed samples enumerated with the

numbers 2 and 5 are demonstrated in Figures 4.7-4.a and b, respectively. It can be concluded from the presented micrographs that flow lines disappeared and a homogenous distribution of oxide formation was observed throughout the cross section of the annealed materials. Additionally, as a consequence of the annihilation of residual stresses due to the annealing treatment, the needle-like martensitic structures became apparent as indicated in the black circles.

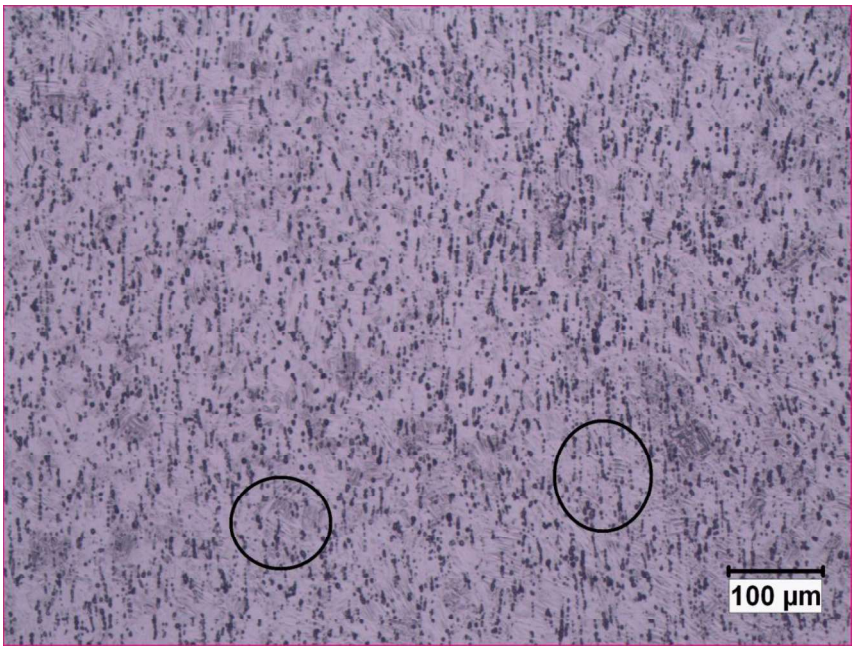

(a)

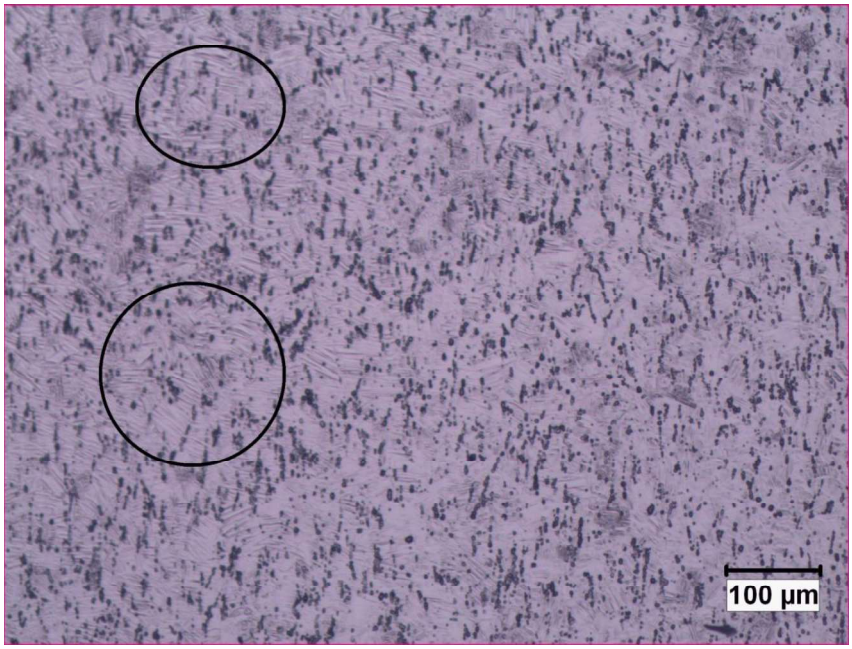

(b)

Figure 4.7-4. Optical micrograph images obtained from (a) annealed specimen 2 and (b) annealed specimen 5 [17].

4.7.4. Post-Fatigue Fracture Surface Analysis of Annealed Samples

Post-fatigue fracture surfaces of the annealed samples were examined by SEM and the fracture surface images are represented in Figures 4.7-5.a and b, respectively. The fractography examination revealed intergranular cracking with rock-candy triple points for the annealed samples. Ductile dimples had been also observed in the fracture surface analysis of the hot extruded samples tested at different H/C rates, however, these dimples were not observed for the annealed samples. It can be concluded that the stress relief and microstructural uniformity after annealing heat treatment at 550°C for 3h leads to increase actuation fatigue lives of the alloy and causes to observe more intergranular cracking. In addition, it is known that there is no precipitation mechanism in equiatomic alloys. On the other hand, some local regions in the material may have higher Ni-content than 50% (at.) and GP zones of H-phase type of precipitates may be formed in the Ni-rich regions at the early stage precipitation with annealing of the hot extruded material. It is likely that these GP zones did not affect TTs of the alloy since

the hot extruded and annealed samples exhibited almost the same stress free TTs, but strengthen the material via hindering dislocation motion during plastic deformation and may lead to observe more intergranular fracture during actuation fatigue experiments.

(a)

(b)

Figure 4.7-5. Backscattered scanning electron micrographs of the fracture surface of the annealed samples after failure during the functional fatigue experiments; (a) annealed sample 2 and (b) annealed sample 5.

4.7.5. Discussion of Results for Annealed Samples

To sum up, since the enumerated samples exhibited the different shape memory properties, annealing heat treatment was applied on the two other fatigue specimens which were cut from the another part of the same extruded billet to be able to overcome these variations. It is worth to mention that both annealed specimens were also virgin specimens taken from another part of the hot-extruded billet. One sample from outermost section and one sample from mid section were chosen considering the sample locations through the cross section of the billet and annealing heat treatment was conducted on these specimens. Almost the same TTs, thermal hysteresis, actuation and $\varepsilon_{austenite}$ magnitudes were observed for both of the annealed specimens as it was represented in the Figures 4.7-2 and 4.7-3. Additionally, TTs stayed almost constant during the thermal cycling experiment from the beginning up to failure. Not only the declining tendency in the actuation strain but also the increasing tendency in the accumulated irrecoverable strain behaviors was almost similar for both of the annealed samples. As shown in Figure 4.7-3.(d), an insignificant variation was seen in the accumulated irrecoverable strain magnitudes for both of the annealed samples with increasing the cycle numbers. Nevertheless, this variation was considerably small compared to the variation that was seen for the enumerated samples. Therefore, it can be deduced that annealing treatment at 550°C-3h provides the rearrangement of dislocation, relieves internal stress and overcomes the deformation variation that was induced during the hot-extrusion process. Figures 4.7-4.a and b displayed the uniform microstructure after annealing treatment and it can be deduced from these microstructure that the flow line formations due to extrusion process was removed and needle-like martensitic structures became clear because of the stress relieve after annealing heat treatment.

Even though annealing heat treated specimens exhibited the highest number of fatigue cycles in the presented study, these cycles are much lower than those of binary NiTi and Ni-rich $Ni_{50.3}Ti_{29.7}Hf_{20}$ HTSMAs. Observing relatively lower fatigue cycles for the equiatomic NiTiHf alloys can be based upon two main reasons. The reason is that the equiatomic NiTiHf alloy that was investigated in this study was heated up to higher

UCT to achieve complete fully austenitic transformation compared to the UCT needed to attain full transformation in binary NiTi and this causes higher plastic deformation due to martensite-austenite phase transformation together with viscoplasticity due to creep and thus premature failure was observed. Additionally, Ni-rich NiTiHf alloys that were studied in the literature are precipitation hardened and so they show longer fatigue lives. It is worth to mention that it is possible to apply age hardening process to the mostly studied Ni-rich $Ni_{50.3}Ti_{29.7}Hf_{20}$ (at.%) alloy and, mechanical and functional properties of this alloy can be enhanced with specific aging treatments by forming nano-scale Ni-rich second phases. Actually, for equiatomic NiTiHf alloy, functional fatigue experiment up to failure were performed for the first time in the present study, thus the functional fatigue lifetimes in this study are not comparable with the lifetimes on Ni-rich NiTiHf alloys that were presented in the literature.

Both annealed samples showed decreasing actuation strain trend and increasing accumulated irrecoverable strain trend with the increase in the cycle numbers as represented in Figures 4.7-3.c and d. The dislocation density accumulates with the cycle numbers and the austenite-martensite phase transformation can be hindered by these transformation induced dislocations which can act as barriers to the martensite-austenite boundary and also partial transformation might be obtained by keeping the UCT constant. Hence, the transforming volume decrease and this can be the reason for the decreasing trend in the ε_{act} and the increasing trend in the $\varepsilon_{austenite}$ magnitudes.

4.8. The Effect of Warm Rolling

Annealing treatment at 550°C-3h was conducted to overcome the deformation variation and so the variation of the SM properties in consequence of hot-extrusion process. After annealing treatment, the stable and similar shape memory properties were observed for the samples which were cut from different cross sections of the extruded billet. On the other hand, it was still observed for the annealed samples that the ε_{act} decreases and accumulated irrecoverable strain ($\varepsilon_{austenite}$) increases with the increment in the cycle numbers. It was decided that the thermal cyclic stability can be further enhanced by enhancing the CSS for dislocation slip and hence, martensite stabilization and plastic

strain formation due to phase transformation can be reduced. This can be provided considering the strengthening mechanisms such as precipitation hardening, grain refinement, solid solution hardening, specific texture formation and work hardening (strain hardening) via increasing the dislocation density [6]. Strain hardening via rolling is the most potential strengthening method to improve the mechanical and SM charactetistics of equiatomic NiTiHf which were examined in detail in the presented study. Since these alloys are known as hard-to-deform material, cold working is not and applicable process and also deformation at ambient temperature without following annealing generally hinders martensitic phase transformation and diminishes to very low temperatures. Besides, strain hardening cannot be attained if the deformation is conducted at higher temperatures due to recrystallization and thus cyclic stability may not be maintained. Hence, the warm rolling operations at about recrystallization temperature of the alloy were applied to observe the influence of the possible enhancement on the SM behaviors and cyclic stability of the material.

Another cylindrical piece was cut from the hot-extruded rod and annealing heat treatment was conducted on this piece at 550°C for 3h before rolling operation. Thereafter, this annealed piece was sliced by WEDM to obtain 1.5 mm thick rolling specimens and the WEDM residue layers were removed via conducting mechanical grinding of the specimens before rolling operation. Since the stable and similar shape memory properties were gained via annealing, the significance of the location of the specimens from the extruded billet regarding the cross section lost its importance. Nevertheless, just to give information, two specimens for rolling process were cut from the mid section of the billet.

4.8.1. Surface Analysis of Warm Rolled Samples

As explained in details in the experimental methods section, the two samples were warm rolled at 600°C and 700°C, respectively, and 5% thickness reduction was achieved for both samples before surface cracks appeared on the rolled samples. The warm-rolled (WR) samples were also mechanically ground again before functional fatigue experiments to eliminate the shallow surface cracks and oxides from the sample

surface. Figure 4.8-1.a, 4.8-1.b and 4.8-1c represent the optical microscope images taken from the surface of the sample that was warm rolled at 600°C, Figures 4.8-1.d, 4.8-.e and 4.8-1.f represent the images for the sample that was rolled at 700°C. Figures 4.8.1.a and d were taken before rolling, 4.8.1.b and e were taken after rolling and the rest of them were taken after surface grinding. For the warm rolled at 600°C sample, there were no surface cracks but a large edge crack was observed after rolling operation as shown in Figure 4.8-1.b. However, this edge crack was out of the gage section of the functional fatigue test specimen. On the other hand, some surface cracks were observed on the sample that was rolled at 700°C with different lengths after the rolling operation as exhibited in Figure 4.8-1.e. These surface cracks were eliminated by mechanical grinding before thermal cycling experiments.

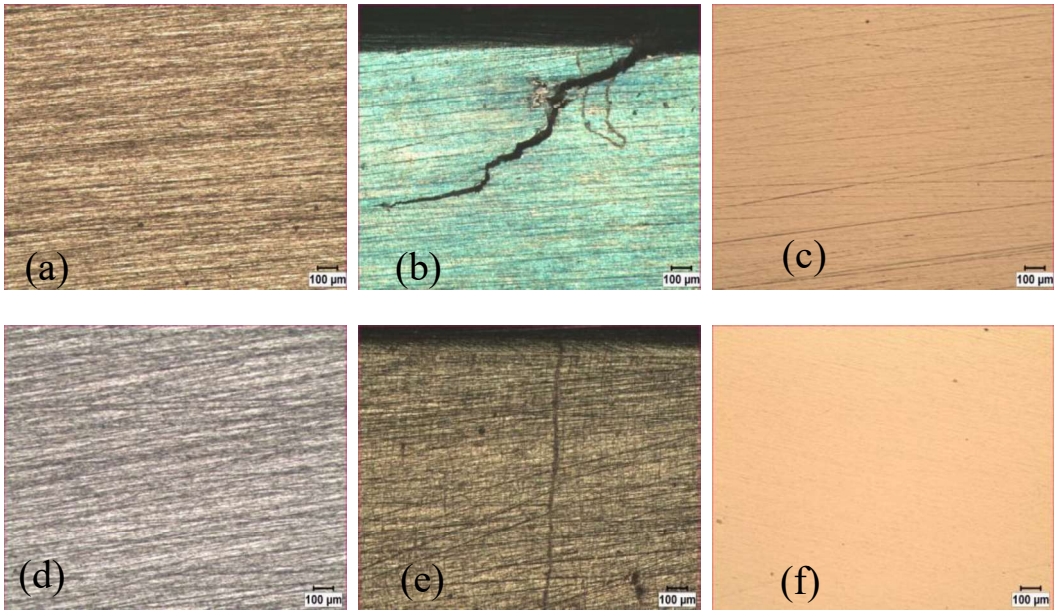

Figure 4.8-1. Optical microscope images taken from the warm rolled at 600°C sample; (a) - (c) before rolling, after rolling and after surface grinding to remove cracks and oxides, respectively, and from the warm rolled at 700°C sample; (d) – (f) before rolling, after rolling and after surface grinding to remove cracks and oxides, respectively.

4.8.2. DSC Analysis of Warm Rolled Samples

The stress free TTs, thermal hysteresis ($A_f - M_s$) and ΔHs of the warm rolled samples were measured by DSC. DSC graphs of both warm rolled samples were illustrated in Figure 4.8-2 and aforementioned values obtained from DSC analysis were summarized in Table 4.8-1. The same TTs, ΔT ($A_f - M_s$) and $\Delta H_{cooling}$ were obtained from both of the WR samples and represented in Figure 4.8-2 and Table 4.8-1.

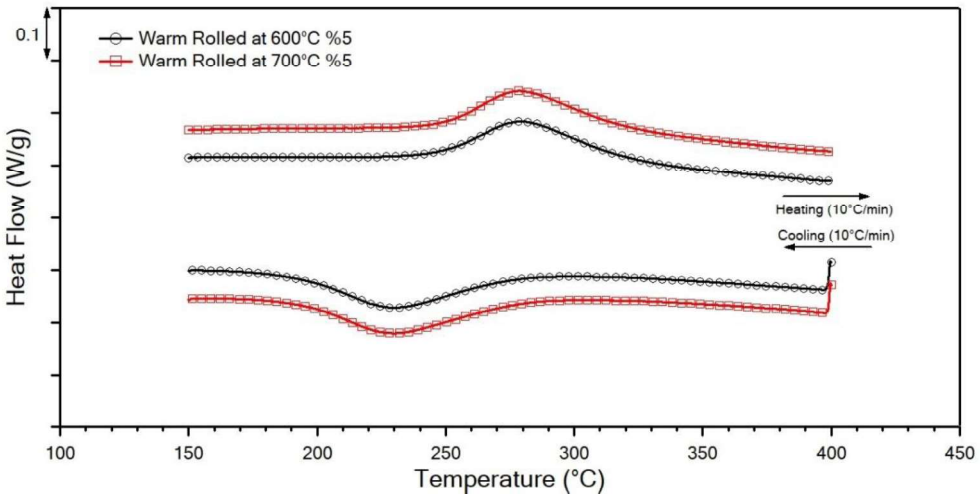

Figure 4.8-2. DSC results of the samples that were warm rolled at 600°C and 700°C with %5 thickness reduction.

Table 4.8-1. Stress free TTs, ΔT (°C) and ΔH of warm rolled samples which were drawn from DSC graphs.

	WR at 600°C for %5	**WR at 700°C for %5**
A_f (°C)	322	322
A_s (°C)	248	249
M_s (°C)	280	282
M_f (°C)	189	189
Thermal Hysteresis (A_f - M_s) (°C)	42	40
Transformation		

Enthalpy (J/g) **($\Delta H_{cooling}$)**	23.83	22.42

4.8.3. Functional Fatigue Tests of Warm Rolled Specimens

Thermal cycling experiments were conducted on both warm rolled samples under 200 MPa constant stress with 15°C/s heating/cooling rate and between 150°C and 430°C. It is substantial to mention that edge grinding was also conducted on warm rolled samples in order to mitigate edge roughness before functional fatigue experiments. The ε vs T graphs of the warm rolled specimens were represented in Figure 4.8-3.a and b. The specimens with 5% thickness reduction that were rolled at 600 and 700°C failed at 7029th and 2247th cycles, respectively, as shown in Figure 4.8-3.

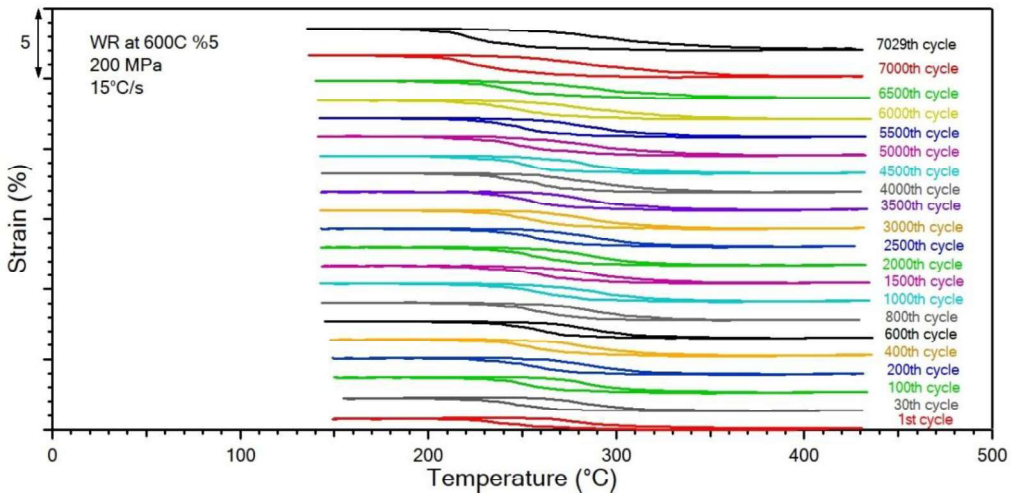

(a)

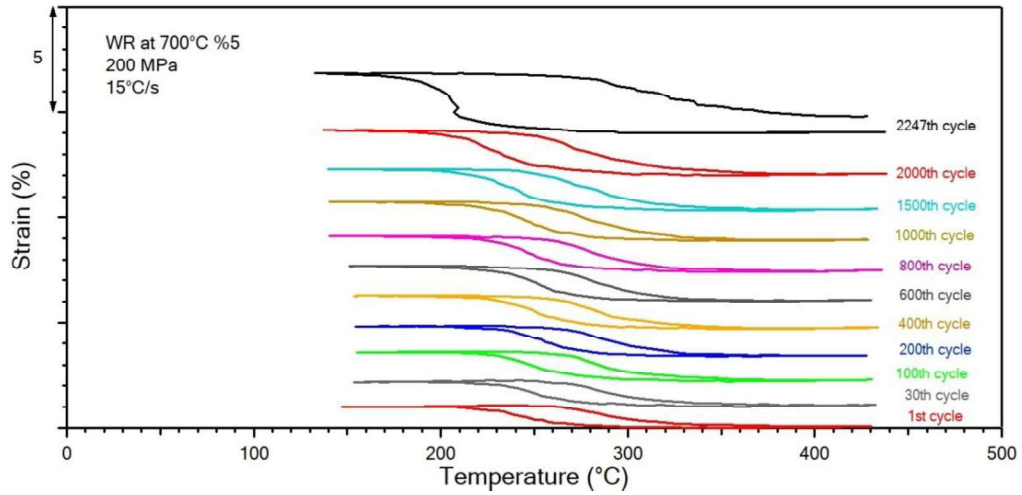

(b)

Figure 4.8-3. ε vs T responses obtained from the functional fatigue experiments of the warm rolled samples with 5% thickness reduction; (a) at 600°C and (b) at 700°C.

The TTs, ΔT, ε_{act} and accumulated strain ($\varepsilon_{austenite}$) responses which were drawn from the ε vs T curves of two warm rolled specimens are illustrated in Figure 4.8-4.a, 4.8-4.b, 4.8-4.c and 4.8-4.d, respectively. Almost stable behaviors of TTs were observed for the sample that WR at 600°C with the number of cycles. A very small change was observed towards failure as illustrated in Figure 4.8-4.a. On the other hand, all TTs of the sample that was rolled at 700°C decreased during thermal cycling except austenite finish (A_f) temperature which were similar with the A_f values of the other warm rolled specimen up to 2000 cycle. The warm rolled samples showed similar thermal hysteresis values and trend for the first 1000 cycles. The specimen that was rolled at 600°C showed stable ΔT at 30°C up to 6000th cycle. However, the ΔT values of the rolled at 700°C sample increased as exihibited in Figure 4.8-4.b.

ε_{act} magnitude of the sample that was rolled at 700°C increased from 0.9% up to approximately 2% with the cycle numbers as displayed in Figure 4.8-4.c. However, even if the increasing actuation strain behavior was observed at the beginning for the the WR at 600°C sample, the stability of ε_{act} was almost obtained between 400 and 6500 cycles at about 1.2% strain. It is important to mention that the initial ε_{act} value of the

rolled at 600°C sample is less than that of the rolled at 700°C sample. The $\varepsilon_{austenite}$ values of the sample that was rolled at 700°C rapidly increased and high elongation and necking were also observed during thermal cyclic. The WR at 600°C specimen exhibited almost linearly increasing accumulated irrecoverable strain from 400 to 6500 cycles and escalated rapidly after 6500 cycles until failure as illustrated in Figure 4.8-4.d.

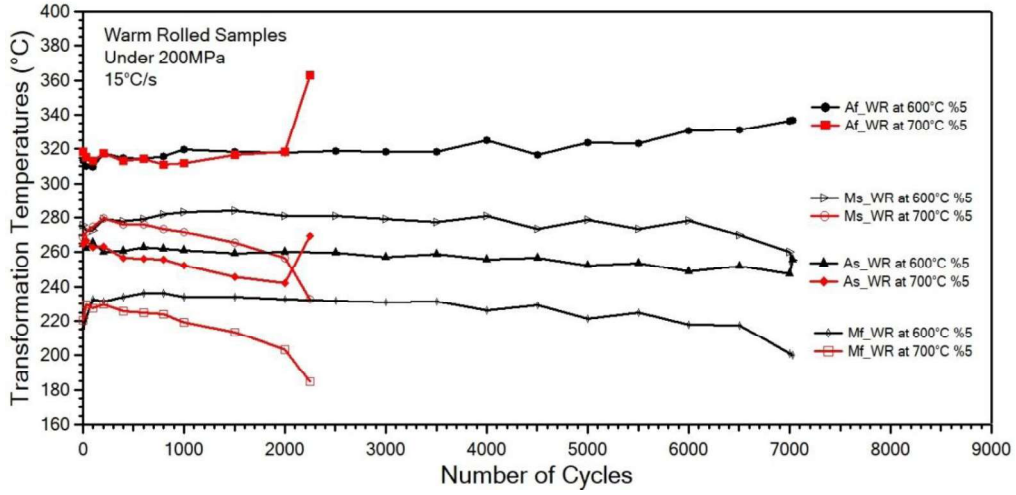

(a)

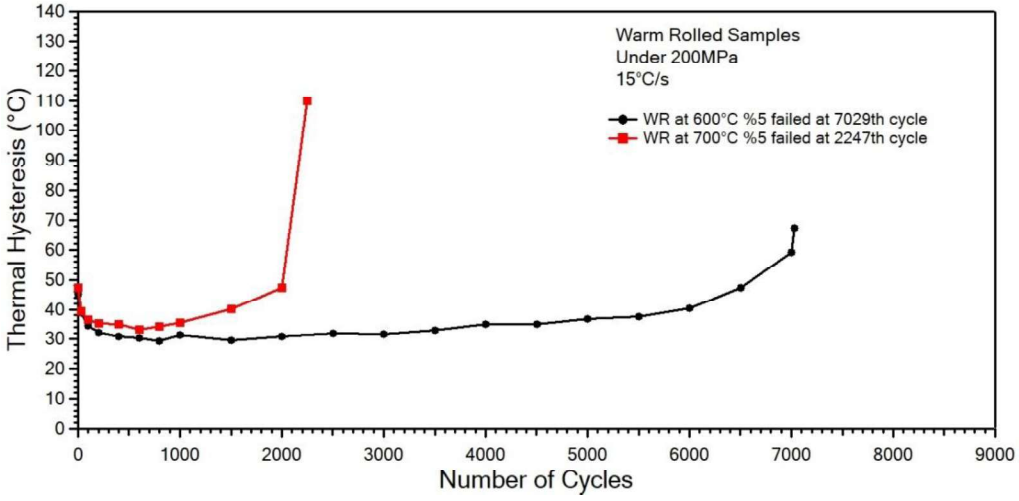

(b)

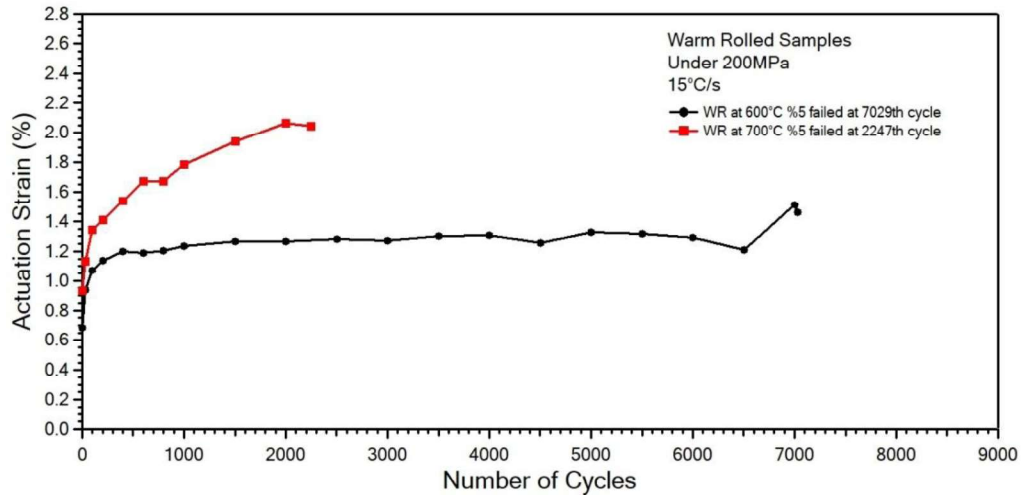

(c)

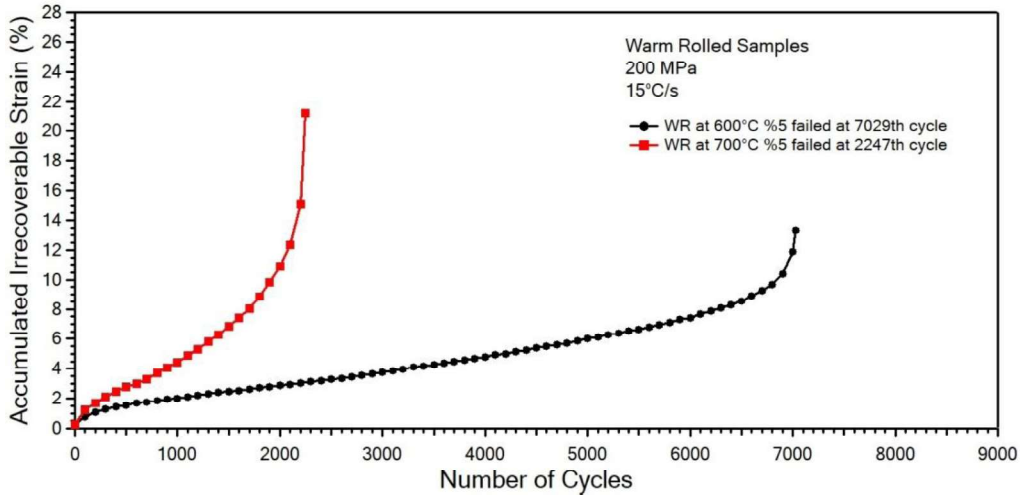

(d)

Figure 4.8-4. (a) TTs, (b) ΔT, (c) ε_{act} and (d) $\varepsilon_{austenite}$ evolution with the cycle numbers drawn from the functional fatigue tests of two warm rolled samples.

4.8.4. Post-Fatigue Fracture Surface Analysis of Warm Rolled Samples

Post-fatigue fracture features of both of the WRed samples were analyzed with SEM and demonstrated in Figures 4.8-5.a and b, respectively. The fractography examination of the WRed samples revealed mixed-mode of transgranular cracking, intergranular cracking and ductile dimples features. The warm rolled at 700°C sample represented

more dimples as represented in the Figure 4.8-5.b compared to the warm rolled at 600°C sample which can be attributed to the possible recrystallization at 700°C [15]. High necking and long elongation were also observed at the end of the thermal cycling under constant stress tests of the warm rolled at 700°C sample. Therefore, it can be concluded the warm rolling at 700°C for 5% thickness reduction was not enough to strengthen the material sufficiently due to the probable dynamic recrystallization at this temperature and led to observe more dimples compared to the sample that was WRed at 600°C.

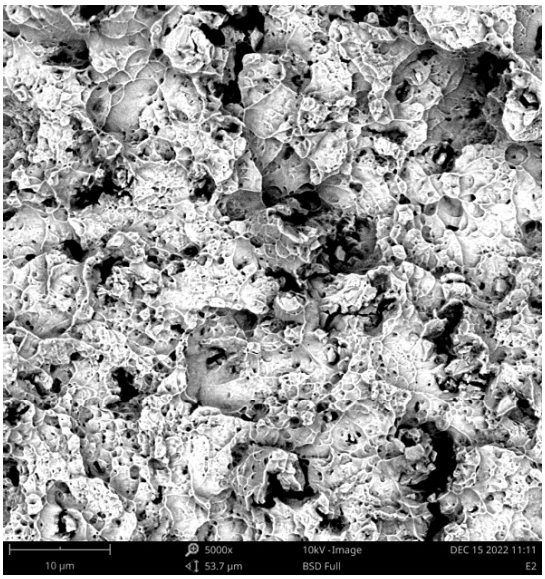

(a)

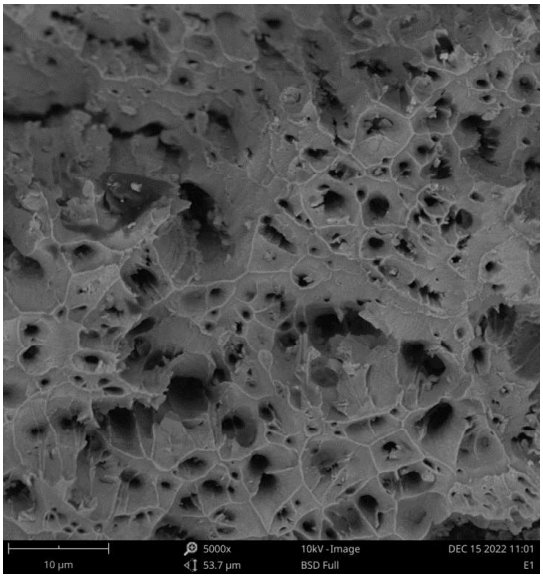

(b)

Figure 4.8-5. Backscattered scanning electron micrographs of the fracture surface of the warm rolled for %5 thickness reduction samples after failure during the functional fatigue experiments; (a) warm rolled at 600°C and (b) warm rolled at 700°C.

4.8.5. Discussion of Results for Warm Rolled Samples

It was observed from the DSC analysis of the warm rolled specimens that the A_s and M_f temperatures decreased after warm rolling operation while the A_f and M_s temperatures stayed almost the same with that of the extruded and annealed conditions. The A_s temperature was observed as 286°C and 281°C for the extruded and annealed samples, respectively, but it was seen that this temperature decreased down to 248°C and 249°C for the warm rolled at 600°C & 700°C samples, respectively. This decrease can be based upon the increasing elastic strain energy after warm rolling operation which facilitates reverse transformation and so austenitic transformation starts earlier. The M_f TTs of the extruded and annealed samples were 236°C and 229°C, respectively, while it was measured as 189°C for both of the warm rolled samples since increasing dislocation density after warm rolling hinders martensitic transformation and overcooling is necessary to complete transformation. Additionally, as expected, the lower transformation enthalpies were observed for two of the warm rolled samples than that of

the extruded and annealed ones due to the increasing dislocation density and the decreasing transforming volume after warm rolling. A small decrease in thermal hysteresis ($A_f - M_s$) values was observed after warm rolling operation. The wider and flattened transformation curves were obtained for the warm rolled samples. Since processing induced dislocations after rolling operation causes martensite stabilization, the transformation occurs in a wider temperature range. A decrease in M_s temperatures of the warm rolled samples was expected after rolling process due to the increment in the dislocation amount, and this increase may inhibit the interphase propagation and martensite nucleation. However, the same M_s temperatures were observed after warm rolling which can be attributed to lower thickness reduction value and less generation of deformation induced dislocations. It is worth to mention that M_s temperature is mostly affected by the amount of dislocations [54].

The sample that was rolled at 600°C showed almost stable transformation temperatures and thermal hysteresis with the cycle numbers until 6000^{th} cycle in functional fatigue tests as exhibited in Figure 4.8-4.a and b. The rolling operation at this temperature probably created homogenously distributed dislocations in the microstructure and the increase in dislocation density suppressed the new dislocation generation with the phase transformation which would cause the instability of the properties. However, the dislocation density could not be increased effectively with the rolling at 700°C because of the possible dynamic recrystallization at this temperature [15], so the TTs decreased and ΔT increased with the increment in the cycle numbers since the dislocation density increased with the phase transformation and inhibited the phase transformation during thermal cycling.

The rapidly increasing actuation strain behavior was observed at the beginning for both of the warm rolled samples as shown in Figure 4.8-4.c. It might be due to the fact that thermal cycling under constant stress causes the rearrangement of existing dislocations which were created after warm rolling of the materials [6]. These rearranged defects support local internal stress fields which promote single variant martensite, and so increase the ε_{act} with the increase in the cycle numbers. The increasing dislocation density leads strain hardening and then the dislocation amount is saturated since the

applied stress was kept constant throughout the cycle. Therefore, the actuation strain magnitudes for the sample that was warm rolled at 600°C saturate after 400 cycles. Additionally, the relatively lower TTs were observed for the rolled samples during thermal cycling. Especially A_f temperature of the WRed at 600°C sample was 50°C less than the A_f temperatures of the annealed ones that were approximately 370°C. The less TTs led to complete transformation and so the stable actuation strain behavior was obtained between 400 and 6500 cycles for the warm rolled at 600°C sample. Then, the increasing actuation strain values were again seen for this sample towards failure due to necking of the test specimen which caused to decrease in the cross section and increase the applied stress promoting more martensite variants favorably aligned and detwinned [4]. The gradually increasing actuation strain trend was obtained for the warm rolled at 700°C sample from the beginning up to failure. This can be attributed to probable formation of more microcracks after rolling operation of this material since the sample was heated at open atmosphere that led to very severe oxidation. The oxidation causes to attain more surface microcrack formations. These cracks might lead to create local internal stress fields and single variant martensite, and also cause more expansion and contraction of cracks which promote an increase in ε_{act} values and a decrease in actuation fatigue life due to faster crack propagation [13].

During the warm rolling of the material at 600°C, homogenously distributed defects might have been obtained throughout the microstructure. Since the sample had already strain hardened after rolling operation, the lower accumulated irrecoverable strain was observed for this sample through the first cycles compared to the annealed samples. Nevertheless, the rolling operation likely caused to form microcracks in the sample and the $\varepsilon_{austenite}$ values for this sample increased faster than that of the annealed samples. Thus, the less fatigue life was obtained for the sample that was rolled at 600°C, which was 7029 cycles than that of the annealed samples, which were about 12.000 cycles. Figure 4.8-4.d exhibited that the irrecoverable strain of the warm rolled at 600°C sample increased rapidly towards the failure due to the high plastic deformation with necking of the sample.

For the sample that was warm rolled at 700°, while the dislocations were induced to the sample during rolling operation, these dislocations were likely annihilated because of dynamic recrystallization and the sample could not be strengthened sufficiently. As a result, the creation of new dislocations and the movement of the defects could not be inhibited during phase transformation in fatigue experiments and the faster plastic deformation occurred. The rapidly increasing accumulated irrecoverable strain magnitudes were observed and the material failed at 2247^{th} cycle which was very low fatigue life compared to that of the annealed samples.

4.9. Hardness Tests

Vickers microhardness tests were utilized throughout the cross section of the samples that were extruded, annealed at 550°C-3h and rolled. Ten measurements were recorded for each material condition and average values were reported in Table 4.9-1. The microhardness of the extruded and annealing treated samples exhibited similar distribution and average values. While the extruded material demonstrated the microhardness average values of 355 Hv, the annealed one exhibited the average values of 356 Hv. It can be deduced that annealing could overcome the deformation variation problem but it did not affect the hardness of the extruded material as seen in the table.

The microhardness values of the WRed at 600°C and 700°C samples were about 400 Hv and 386 Hv, respectively. It can be indicated that less dislocation density was generated by warm rolling operation at 700°C than that of the one at 600°C for the same thickness reduction due to the possible dynamic recrystallization effect at relatively higher temperature.

Table 4.9-1. Vickers Microhardness of the extruded, annealed and warm rolled $Ni_{50}Ti_{30}Hf_{20}$ (at%) HTSMA.

Material Condition	**Hardness (Hv)**
Extruded	355 Hv
Annealed at 550°C for 3h	356 Hv
Warm Rolled at 600°C %5	400 Hv
Warm Rolled at 700°C %5	386 Hv

5. CONCLUSION

In the presented study, the influence of H/C rates to the shape memory properties, surface roughness of the test specimens, temperature distribution of the test set up and chemical composition distribution of the extruded $Ni_{50}Ti_{30}Hf_{20}$ (at.%) HTSMA were first investigated and the following outcomes were obtained from the presented results:

- Although the randomly selected samples from the extruded billet were thermally cycled under 200MPa with the same H/C rate and upper cycle temperature, different SM properties such as TTs, ΔT, ε_{act} and $\varepsilon_{austenite}$ were observed from the functional fatigue experiments. The fatigue lives of the randomly selected samples which were tested for 15°C/s rate were 1738, 754 and 580 cycles. It was seen that there is no any localization or segregation of the element, so the chemical compositional difference in the specimens could not be a reason to observe various shape memory behaviors and fatigue lifetimes. Oxides were also determined in EDS mapping analysis due to oxygen affinity of hafnium. Additionally, the flow lines and elongated grains in difference direction and dimensions were also observed because of deformation variation induced by extrusion process.
- The temperature distribution on the test specimen during thermal cycling was observed as almost the same for different H/C rates.
- Surface roughness of the test specimens caused to obtain very low fatigue lives which were about 500 cycles since the edge cracks can act as stress concentrators which led to premature failure.
- The standardization of the testing and sample conditions is highly important in achieving reliable and consistent actuation fatigue properties of HTSMAs.

Functional fatigue experiments were repeated on the enumerated samples to analyze the effect of deformation variation as a result of hot extrusion process and it can be concluded from the presented study:

- Shape memory properties that were attained from the functional fatigue tests of enumerated samples were exhibited to be different for the same experiment

conditions similar to randomly selected samples but almost similar SM properties were determined for the symmetrical samples considering the location in the cross-section of the hot extruded billet.

- Different actuation fatigue behaviors was attributed to hot extrusion process with 4:1 area reduction leading to microstructural nonuniformity and internal stress together with deformation variation as indicated in Figure 4.6-3.
- Finer and relatively homogenous microstructure was observed for the samples that were enumerated as 3 and 6 as demonstrated in Figures 4.6-3.b and c which caused to observe better SM and mechanical properties.
- The edges of the randomly selected samples were not ground. However, edge grinding was applied to the enumerated dog bone shape samples and removing the surface roughness and very small edge cracks improved the functional fatigue lifetime of the material more than 4 times.
- The rapidly increasing ε_{act} and $\varepsilon_{austenite}$ magnitudes were seen for the sample 7 due to wrong temperature measurement in consequence of peeling off the high temperature black paint and heating the sample to higher UCT. Therefore, it is substantial to achieve accurate temperature measurement during thermal cycling experiments.

Annealing treatment was conducted at 550°C-3h to be able to overcome the deformation variation and internal stress due to hot extrusion process, and one of the outermost sample and one of the mid section sample were fatigue tested. These are the conclusions which were gathered from the presented results:

- Annealing treatment did not alter the stress free transformation temperatures as illustrated in Figure and Table 4.7-1. Nevertheless, annealing provided relieving internal stress, removing the deformation variation and microstructural nonuniformity as can be seen in Figure 4.7-4, hence, annealed specimens exhibited almost the identical shape memory properties, which were obtained from the functional fatigue tests.
- Stable transformation temperature values were obtained with the increase in the cycle numbers in H/C experiments for both of the annealed specimens.

- Annealed samples exhibited less accumulated irrecoverable strain increment than that of randomly selected and enumerated hot extruded samples, and both annealed samples also resulted the longest fatigue lives than that of the other of the other hot extruded $Ni_{50}Ti_{30}Hf_{20}$ (at.%) samples.
- Martensitic structure became distinct as shown in Figure 4.7-4 due to stress relieve with annealing treatment.

Lastly, the warm rolling operations were applied at 600°C and 700°C with 5% thickness reduction following the annealing treatment to enhance the thermal cyclic stability concomitant with the increment of the CSS for dislocation slip and here are the conclusions, which can be gathered from the presented results:

- Almost the same stress free TTs, ΔTs, and ΔHs were obtained for both of WRed samples, and the ΔHs of WRed samples were less than those of the extruded and annealed materials as expected.
- Stability of the shape memory properties with the number of cycles was almost achieved after warm rolling at 600°C while the properties of warm rolled at 700°C sample deteriorated during functional fatigue experiment.
- The increase in the ε_{act} values were observed with the increment in the cycle numbers through the first cycles for both of the warm rolled samples since thermal cycles under stress dictated the rearrangement of dislocation induced with rolling operation. Thus, these defects promoted local internal stress and single variant martensite, and caused to observe the increasing actuation strain trend.

For the warm rolled at 600°C sample, lower $\varepsilon_{austenite}$ values were observed through the first hundreds of cycles but then the increase in the irrecoverable strain values was higher and actuation fatigue life was less than those of the ones seen in thermal cycling experiments of annealed samples possibly due to the microcracks induced during rolling operation.

6. REFERENCES

[1] K. Otsuka, X. Ren, Recent developments in the research of shape memory alloys, Intermetallics. 7 (**1999**) 511–528.

[2] J. Mohd Jani, M. Leary, A. Subic, M.A. Gibson, A review of shape memory alloy research, applications and opportunities, Mater. Des. 56 (**2014**) 1078–1113.

[3] D.J. Hartl, D.C. Lagoudas, Aerospace applications of shape memory alloys, Proc. Inst. Mech. Eng. Part G J. Aerosp. Eng. 221 (**2007**) 535–552.

[4] J. Ma, I. Karaman, R.D. Noebe, High temperature shape memory alloys, Int. Mater. Rev. 55 (**2010**) 257–315.

[5] B. Kockar, I. Karaman, J.I. Kim, Y.I. Chumlyakov, J. Sharp, C.J. (Mike) Yu, Thermomechanical cyclic response of an ultrafine-grained NiTi shape memory alloy, Acta Mater. 56 (**2008**) 3630–3646.

[6] B. Kockar, I. Karaman, J.I. Kim, Y. Chumlyakov, A method to enhance cyclic reversibility of NiTiHf high temperature shape memory alloys, Scr. Mater. 54 (**2006**) 2203–2208.

[7] B. Kockar, K.C. Atli, J. Ma, M. Haouaoui, I. Karaman, M. Nagasako, R. Kainuma, Role of severe plastic deformation on the cyclic reversibility of a $Ti_{50.3}Ni_{33.7}Pd_{16}$ high temperature shape memory alloy, Acta Mater. 58 (**2010**) 6411–6420.

[8] R. Santamarta, R. Arróyave, J. Pons, A. Evirgen, I. Karaman, H.E. Karaca, R.D. Noebe, TEM study of structural and microstructural characteristics of a precipitate phase in Ni-rich Ni-Ti-Hf and Ni-Ti-Zr shape memory alloys, Acta Mater. 61 (**2013**) 6191–6206.

[9] A. Evirgen, F. Basner, I. Karaman, R.D. Noebe, J. Pons, R. Santamarta, Effect of aging on the martensitic transformation characteristics of a Ni-Rich NiTiHf high temperature shape memory alloy, Funct. Mater. Lett. 5 (**2012**) 1250038.

[10] G.S. Bigelow, A. Garg, S.A. Padula, D.J. Gaydosh, R.D. Noebe, Load-biased shape-memory and superelastic properties of a precipitation strengthened high-temperature Ni50.3Ti29.7Hf20 alloy, Scr. Mater. 64 (**2011**) 725–728. https://doi.org/10.1016/j.scriptamat.2010.12.028.

[11] H.E. Karaca, S.M. Saghaian, G. Ded, H. Tobe, B. Basaran, H.J. Maier, R.D. Noebe, Y.I. Chumlyakov, Effects of nanoprecipitation on the shape memory and material properties of an Ni-rich NiTiHf high temperature shape memory alloy, Acta Mater. 61 (**2013**) 7422–7431. https://doi.org/10.1016/j.actamat.2013.08.048.

[12] O. Benafan, R.D. Noebe, S.A. Padula, R. Vaidyanathan, Microstructural response

during isothermal and isobaric loading of a precipitation-strengthened Ni-29.7Ti-20Hf high-temperature shape memory alloy, Metall. Mater. Trans. A Phys. Metall. Mater. Sci. 43 (**2012**) 4539–4552. https://doi.org/10.1007/s11661-012-1297-z.

[13] O. Karakoc, C. Hayrettin, M. Bass, S.J. Wang, D. Canadinc, J.H. Mabe, D.C. Lagoudas, I. Karaman, Effects of upper cycle temperature on the actuation fatigue response of NiTiHf high temperature shape memory alloys, Acta Mater. 138 (**2017**) 185–197.

[14] H.H. Saygili, H.O. Tugrul, B. Kockar, Effect of aging heat treatment on the high cycle fatigue life of $Ni_{50.3}Ti_{29.7}Hf_{20}$ high-temperature shape memory alloy, Shape Mem. Superelasticity. 5 (**2019**) 32–41.

[15] N. Babacan, M. Bilal, C. Hayrettin, J. Liu, O. Benafan, I. Karaman, Effects of cold and warm rolling on the shape memory response of $Ni_{50}Ti_{30}Hf_{20}$ high-temperature shape memory alloy, Acta Mater. 157 (**2018**) 228–244.

[16] O. Akgul, H.O. Tugrul, B. Kockar, Effect of the cooling rate on the thermal and thermomechanical behavior of NiTiHf high-temperature shape memory alloy, J. Mater. Res. 35 (**2020**) 1572–1581.

[17] E. Akin, O. Akgul, H.O. Tugrul, G. Dugan, B. Kockar, Investigating the effect of hot extrusion and annealing to the functional fatigue behavior of Ni50Ti30Hf20high temperature shape memory alloy, Smart Mater. Struct. 30 (**2021**). https://doi.org/10.1088/1361-665X/ac1bee.

[18] T. Umale, D. Salas, B. Tomes, R. Arroyave, I. Karaman, The effects of wide range of compositional changes on the martensitic transformation characteristics of NiTiHf shape memory alloys, Scr. Mater. 161 (**2019**) 78–83.

[19] F.T. Calkins, G.W. Butler, J.H. Mabe, Variable geometry chevrons for jet noise reduction, in: 12th AIAA/CEAS Aeroacoustics Conf. (27th AIAA Aeroacoustics Conf., **2006**: pp. 1–11. https://doi.org/10.2514/6.2006-2546.

[20] D.C. Lagoudas, D.A. Miller, L. Rong, P.K. Kumar, Thermomechanical fatigue of shape memory alloys, Smart Mater. Struct. 18 (**2009**) 085021.

[21] H. Tobushi, T. Hachisuka, T. Hashimoto, S. Yamada, Cyclic deformation and fatigue of a TiNi shape-memory alloy wire subjected to rotating bending, J. Eng. Mater. Technol. Trans. ASME. 120 (**1998**) 64–70.

[22] O. Karakoc, C. Hayrettin, D. Canadinc, I. Karaman, Role of applied stress level on the actuation fatigue behavior of NiTiHf high temperature shape memory alloys, Acta Mater. 153 (**2018**) 156–168.

[23] K.N. Melton, O. Mercier, Fatigue of NiTi thermoelastic martensites, Acta Metall. 27 (**1979**) 137–144.

[24] K. Gall, J. Tyber, G. Wilkesanders, S.W. Robertson, R.O. Ritchie, H.J. Maier,

Effect of microstructure on the fatigue of hot-rolled and cold-drawn NiTi shape memory alloys, Mater. Sci. Eng. A. 486 (**2008**) 389–403.

[25] G. Eggeler, E. Hornbogen, A. Yawny, A. Heckmann, M. Wagner, Structural and functional fatigue of NiTi shape memory alloys, Mater. Sci. Eng. A. 378 (**2004**) 24–33.

[26] J.F. Liu, C. Li, X.Y. Fang, J.B. Jordon, Y.B. Guo, Effect of wire-EDM on fatigue of nitinol shape memory alloy, Mater. Manuf. Process. 33 (**2018**) 1809–1814.

[27] A. Demblon, O. Karakoc, J. Sam, D. Zhao, K.C. Atli, J.H. Mabe, I. Karaman, Compositional and microstructural sensitivity of the actuation fatigue response in NiTiHf high temperature shape memory alloys, Mater. Sci. Eng. A. 838 (**2022**) 142786.

[28] K.K. Kumar, S. Suresh Kumar, Effect of Friction on Extrusion of Non-Ferrous Alloys-Modelling and Simulation, Int. J. Eng. Adv. Technol. 6 (**2017**) 48–56.

[29] T. Furu, O. Sodahl, E. Nes, L. Hanssen, O. Lohne, The influence of the extrusion speed on texture in the surface layer of aluminium profiles investigated by the EBSP technique, Mater. Sci. Forum. 157–162 (**1994**) 1197–1204.

[30] E.D. Sweet, S.K. Caraher, N. V Danilova, X. Zhang, C.A. Limited, Effects of Extrusion Parameters on Coarse Grain Surface Layer in 6xxx Series Extrusions, Proc. 8th Alum. Ext. Sem. Inum Extrus. Technol. Semin. (**2004**) 115–126.

[31] W.H. Van Geertruyden, H.M. Browne, W.Z. Misiolek, P.T. Wang, Evolution of surface recrystallization during indirect extrusion of 6xxx aluminum alloys, Metall. Mater. Trans. A. 36A (**2005**) 1049–1056.

[32] H. Jiang, L. Li, J. Dong, X. Xie, Microstructure-based hot extrusion process control principles for nickel-base superalloy pipes, Prog. Nat. Sci. Mater. Int. 28 (**2018**) 391–398.

[33] V. Ocenasek, P. Sedlacek, The effect of surface recrystallized layers on properties of extrusions and forgings from high strength aluminium alloys, Met. Conf. Proc. (**2011**) 853–860.

[34] B. Roy, J. Das, Strengthening face centered cubic crystals by annealing induced nano-twins, Sci. Rep. 7 (**2017**) 17512.

[35] J. Gubicza, P.H.R. Pereira, G. Kapoor, Y. Huang, S.S. Vadlamani, T.G. Langdon, Annealing-Induced Hardening in Ultrafine-Grained Ni–Mo Alloys, Adv. Eng. Mater. 20 (**2018**) 1800184.

[36] Z.G. Wang, X.T. Zu, Y. Huo, Effect of heating/cooling rate on the transformation temperatures in TiNiCu shape memory alloys, Thermochim. Acta. 436 (**2005**) 153–155. https://doi.org/10.1016/j.tca.2005.06.028.

[37] K. Nurveren, A. Akdoğan, W.M. Huang, Evolution of transformation

characteristics with heating/cooling rate in NiTi shape memory alloys, J. Mater. Process. Technol. 196 (**2008**) 129–134. https://doi.org/10.1016/j.jmatprotec.2007.05.015.

[38] Treppmann D., E. Hornbogen, On the Influence of Thermomechanical Treatments on Shape Memory Alloys, J. Phys. IV Fr. 7 (**1997**) 211–220.

[39] K. Otsuka, C.M. Wayman, Shape memory materials, Cambridge University Press, **1998**.

[40] Funakubo H., Shape Memory Alloys, Gordon and Breach Science Publishers, Amsterdam, **1987**.

[41] Duerig T.W., K.N. Melton, S. D., C.M. Wayman, Engineering Aspects of Shape Memory Alloys, Butterworth-Heinemann, London, **1990**. https://doi.org/10.1179/sur.1991.7.4.299.

[42] T. Saburi, S. Nenno, Reversible Shape Memory in Cu-Zn-Ga, Scr. Metall. 8 (**1974**) 1363–1367.

[43] A. Nagasawa, K. Enami, Y. Ishino, Y. Abe, S. Nenno, Reversible shape memory effect, Scr. Metall. 8 (**1974**) 1055–1060. https://doi.org/10.1016/S0036-9748(74)80003-7.

[44] B. Kockar, Shape Memory Behavior of Ultrafine Grained NiTi and TiNiPd Shape Memory Alloys, PhD Diss. Texas A&M Univ. (**2007**) 181 pp.

[45] X. Ren, K. Otsuka, Universal symmetry property of point defects in crystals, Phys. Rev. Lett. 85 (**2000**) 1016–1019. https://doi.org/10.1103/PhysRevLett.85.1016.

[46] L.C. Chang, T.A. Read, Plastic Deformation and Diffusionless Phase Changes In Metals - The Gold-Cadmium Beta Phase, Trans. AIME. 189 (**1951**) 47–52.

[47] Buehler WJ, G. JW, Wiley RC., Effect of Low-Temperature Phase Changes on the Mechanical Properties of Alloys near Composition TiNi, J. Appl. Phys. 1475 (**1963**) 13–16.

[48] Segui C., C. E., J. Van Humbeeck, Irreversibility in Two-Stage Martensitic transformations of Cu-Al-Ni and Cu-Zn-Al-Mn alloys, Mater. Trans. JIM. 31 (**1990**) 375–380.

[49] T. Tadaki, M. Tokoro, K. Shimizu, Thermoelastic Nature and Crystal Structure of The Cu-Zn Martensite Related to The Shape Memory, Trans Jap Inst Met. 16 (**1975**) 285–296. https://doi.org/10.2320/matertrans1960.16.285.

[50] R. Dasgupta, A look into Cu-based shape memory alloys: Present scenario and future prospects, J. Mater. Res. 29 (**2014**) 1681–1698. https://doi.org/10.1557/jmr.2014.189.

[51] S.W. Husain, P.C. Clapp, The intergranular embrittlement of Cu-AI-Ni β-phase

alloys, J. Mater. Sci. 22 (**1987**) 2351–2356. https://doi.org/10.1007/BF01082115.

[52] Sakamoto H, K. Shimizu, Experimental Investigation on Cyclic Deformation and Fatigue Behavior of Polycrystalline Cu-Al-Ni Shape Memory Alloys above Ms, Trans. Japan Inst. Met. 27 (**1986**) 592–600.

[53] K. Otsuka, X. Ren, Physical metallurgy of Ti-Ni-based shape memory alloys, Prog. Mater. Sci. 50 (**2005**) 511–678.

[54] S. Miyazaki, K. Otsuka, Deformation and Transition Behavior Associated with the R-phase in Ti-Ni Alloys, Metall. Trans. A,. 17 A (**1986**) 53–63. https://doi.org/10.1007/BF02644442.

[55] Massalski TB, Okamoto H, Subramanian PR, Kacprzak L, Binary alloys phase diagrams, in: ASM Int., 2nd editio, Materials Park (OH), **1990**: p. 2874.

[56] K. Otsuka, T. Kakeshita, Science and technology of shape-memory alloys: New developments, MRS Bull. 27 (**2002**) 91–98. https://doi.org/10.1557/mrs2002.43.

[57] W. Tang, Thermodynamic Study of the Low-Temperature Phase B19 ' and the Martensitic Transformation in Near-Equiatomic Ti-Ni Shape Memory Alloys, 28 (**1997**) 537–544.

[58] K. Gall, H. Sehitoglu, Y.I. Chumlyakov, Y.L. Zuev, I. Karaman, The Role of Coherent Precipitates in Martensitic Transforamtions in Single Crystals, 39 (**1998**) 699–705.

[59] J. Khalil-Allafi, A. Dlouhy, G. Eggeler, Ni4Ti3-precipitation during aging of NiTi shape memory alloys and its influence on martensitic phase transformations, 50 (**2002**) 4255–4274.

[60] A. Evirgen, I. Karaman, R. Santamarta, J. Pons, C. Hayrettin, R.D. Noebe, Relationship between crystallographic compatibility and thermal hysteresis in Ni-rich NiTiHf and NiTiZr high temperature shape memory alloys, Acta Mater. 121 (**2016**) 374–383.

[61] E.P. George, C.T. Liu, J.A. Horton, C.J. Sparks, M. Kao, H. Kunsmann, T. King, Characterization, processing, and alloy design of NiAl-based shape memory alloys, Mater. Charact. 39 (**1997**) 665–686. https://doi.org/10.1016/s1044-5803(97)00149-6.

[62] J.H. Yang, C.M. Wayman, On the formation mechanism of Ni5Al3 in NiAl-base alloys: Part II. Kinetics, Intermetallics. 2 (**1994**) 121–126. https://doi.org/10.1016/0966-9795(94)90006-X.

[63] K. Adachi, C.M. Wayman, Transformation behavior of nearly stoichiometric Ni-Mn alloys, Metall. Trans. A. 16 (**1985**) 1567–1579. https://doi.org/10.1007/BF02663013.

[64] E.L. Semenova, Y. V. Kudryavtsev, Structural phase transformation and shape

memory effect in ZrRh and ZrIr, J. Alloys Compd. 203 (**1994**) 165–168. https://doi.org/10.1016/0925-8388(94)90729-3.

[65] K. Otsuka, K. Oda, Y. Ueno, M. Piao, T. Ueki, H. Horikawa, The shape memory effect in a Ti50Pd50 alloy, Scr. Metall. Mater. 29 (**1993**) 1355–1358. https://doi.org/10.1016/0956-716X(93)90138-I.

[66] B.H. Chen, H.F. Franzen, Phase transitions and heterogeneous equilibria in the TaRu homogeneity range, J. Less-Common Met. 157 (**1990**) 37–45. https://doi.org/10.1016/0022-5088(90)90404-8.

[67] Z.R. He, J.E. Zhou, Y. Furuya, Effect of Ta content on martensitic transformation behavior of RuTa ultrahigh temperature shape memory alloys, Mater. Sci. Eng. A. 348 (**2003**) 36–40. https://doi.org/10.1016/S0921-5093(02)00641-X.

[68] P.G. Lindquist, C.M. Wayman, Engineering Aspects of Shape Memory Alloys, in: Duerig T.W. (Ed.), Butterworth-Heinemann Ltd., London, **1990**: pp. 58–68.

[69] D. Golberg, Y. Xu, Y. Murakami, K. Otsuka, T. Ueki, H. Horikawa, High-temperature shape memory effect in Ti50Pd50 - xNix (x = 10, 15, 20) alloys, Mater. Lett. 22 (**1995**) 241–248. https://doi.org/10.1016/0167-577X(94)00256-8.

[70] Y. Xu, S. Shimizu, Y. Suzuki, K. Otsuka, T. Ueki, K. Mitose, Recovery and recrystallization processes in Ti-Pd-Ni high-temperature shape memory alloys, Acta Mater. 45 (**1997**) 1503–1511. https://doi.org/10.1016/S1359-6454(96)00267-4.

[71] K.C. Atli, I. Karaman, R.D. Noebe, A. Garg, Y.I. Chumlyakov, I. V. Kireeva, Improvement in the shape memory response of Ti50.5Ni 24.5Pd25 high-temperature shape memory alloy with scandium microalloying, Metall. Mater. Trans. A Phys. Metall. Mater. Sci. 41 (**2010**) 2485–2497. https://doi.org/10.1007/s11661-010-0245-z.

[72] D. Golberg, Y. Xu, Y. Murakami, S. Morito, K. Otsuka, T. Ueki, H. Horikawa, Characteristics of Ti50Pd30Ni20 high-temperature shape memory alloy, Intermetallics. 3 (**1995**) 35–46. https://doi.org/10.1016/0966-9795(94)P3684-G.

[73] G.S. Bigelow, S.A. Padula, A. Garg, D. Gaydosh, R.D. Noebe, Characterization of ternary NiTiPd high-temperature shape-memory alloys under load-biased thermal cycling, Metall. Mater. Trans. A Phys. Metall. Mater. Sci. 41 (**2010**) 3065–3079. https://doi.org/10.1007/s11661-010-0365-5.

[74] O. Rios, R. Noebe, T. Biles, A. Garg, A. Palczer, D. Scheiman, H.J. Seifert, M. Kaufman, Characterization of ternary NiTiPt high-temperature shape memory alloys, Smart Struct. Mater. 2005 Act. Mater. Behav. Mech. 5761 (**2005**) 376. https://doi.org/10.1117/12.599608.

[75] R. Noebe, S. Draper, D. Gaydosh, A. Garg, B. Lerch, N. Penney, G. Bigelow, S. Padula, J. Brown, Effect of thermomechanical processing on the microstructure,

properties, and work behavior of a Ti50.5Ni29.5Pt20 High-temperature shape memory alloy, SMST-2006 - Proc. Int. Conf. Shape Mem. Superelastic Technol. (**2008**) 409–426. https://doi.org/10.1361/cp2006smst4O9.

[76] S.F. Hsieh, S.K. Wu, A Study on Ternary Ti-rich TiNiZr Shape Memory Alloys, Mater. Charact. 41 (**1998**) 151–162. https://doi.org/10.1016/s1044-5803(98)00032-1.

[77] Z. Pu, H. Tseng, K. Wu, Martensite Transformation and Shape Memory Effect of NiTi-Zr High Temperature Shape Memory Alloys, Proc. SPIE. 2441 (**1995**) 171–178.

[78] A.M. Pérez-Sierra, J. Pons, R. Santamarta, I. Karaman, R.D. Noebe, Stability of a Ni-rich Ni-Ti-Zr high temperature shape memory alloy upon low temperature aging and thermal cycling, Scr. Mater. 124 (**2016**) 47–50. https://doi.org/10.1016/j.scriptamat.2016.06.029.

[79] A. Evirgen, I. Karaman, J. Pons, R. Santamarta, R.D. Noebe, Role of nano-precipitation on the microstructure and shape memory characteristics of a new Ni50.3Ti34.7Zr15 shape memory alloy, Mater. Sci. Eng. A. 655 (**2016**) 193–203. https://doi.org/10.1016/j.msea.2015.12.076.

[80] Han S, Zou W, Jin S, Zhang Ze, Yang D, The Studies of The Martensite Transformations in a Ti36.5Ni48.5Hf15 Alloy, Scr. Metall. Mater. 32 (**1995**) 1441–1446.

[81] X.L. Meng, W. Cai, L.M. Wang, Y.F. Zheng, L.C. Zhao, L.M. Zhou, Microstructure of stress-induced martensite in a Ti-Ni-Hf high temperature shape memory alloy, Scr. Mater. 45 (**2001**) 1177–1182. https://doi.org/10.1016/S1359-6462(01)01147-2.

[82] D.R. Angst, P.E. Thoma, M.Y. Kao, The Effect of Hafnium Content on the Transformation Temperatures of Ni 49 Ti 51-x Hf x . Shape Memory Alloys , J. Phys. IV. 05 (**1995**) C8-747-C8-752. https://doi.org/10.1051/jp4/199558747.

[83] D. AbuJudom, P.E. Thoma, M.-Y. Kao, D.R. Angst, High Transformation Temperature Shape Memory Alloy, US Patent 5.114.504, **1992**.

[84] H.E. Karaca, E. Acar, H. Tobe, S.M. Saghaian, NiTiHf-based shape memory alloys, Mater Sci Technol. 30 (**2014**) 1530–1544.

[85] M. Zarinejad, Y. Liu, T.J. White, The crystal chemistry of martensite in NiTiHf shape memory alloys, Intermetallics. 16 (**2008**) 876–883. https://doi.org/10.1016/j.intermet.2008.04.004.

[86] X.L. Meng, Y.F. Zheng, Z. Wang, L.C. Zhao, Shape memory properties of the Ti36Ni49Hf15 high temperature shape memory alloy, Mater. Lett. 45 (**2000**) 128–132. https://doi.org/10.1016/S0167-577X(00)00091-4.

[87] Y.Q. Wang, Y.F. Zheng, W. Cai, L.C. Zhao, The Tensile Behavior of

Ti36Ni49Hf15 High Temperature Shape Memory Alloy, Acta Metall. 40 (**1999**) 1327–1331.

[88] F. Dalle, E. Perrin, P. Vermaut, M. Masse, R. Portier, Interface mobility in Ni49.8Ti42.2Hf8 shape memory alloy, Acta Mater. 50 (**2002**) 3557–3565.

[89] P.E. Thoma, J.J. Boehm, The effect of hafnium and thermal cycling on the transformation temperatures of NiTi-based shape memory alloys, Mater. Res. Soc. Symp. - Proc. 604 (**2000**) 221–226. https://doi.org/10.1557/proc-604-221.

[90] S. Besseghini, E. Villa, A. Tuissi, Ni-Ti-Hf shape memory alloy: Effect of aging and thermal cycling, Mater. Sci. Eng. A. 273–275 (**1999**) 390–394. https://doi.org/10.1016/s0921-5093(99)00304-4.

[91] P. Olier, J.C. Brachet, J.L. Bechade, C. Foucher, G. Guénin, Investigation of Transformation Temperatures, Microstructure and Shape Memory Properties of NiTi, NiTiZr and NiTiHf Alloys, J. Phys. IV. 05 (**1995**) C8-741-C8-746. https://doi.org/10.1051/jp4/199558741.

[92] X.L. Meng, Y.F. Zheng, Z. Wang, L.C. Zhao, Effect of aging on the phase transformation and mechanical behavior of Ti36Ni49Hf15 high temperature shape memory alloy, Scr. Mater. 42 (**2000**) 341–348. https://doi.org/10.1016/S1359-6462(99)00347-4.

[93] P.E. Thoma, J.J. Boehm, Effect of composition on the amount of second phase and transformation temperatures of NixTi90-xHf10 shape memory alloys, Mater. Sci. Eng. A. 273–275 (**1999**) 385–389. https://doi.org/10.1016/s0921-5093(99)00303-2.

[94] M.M. Javadi, M. Belbasi, M.T. Salehi, M.R. Afshar, Effect of aging on the microstructure and shape memory effect of a hot-rolled NiTiHf alloy, J. Mater. Eng. Perform. 20 (**2011**) 618–622. https://doi.org/10.1007/s11665-011-9885-4.

[95] K.S. Suresh, D.I. Kim, S.K. Bhaumik, S. Suwas, Evolution of microstructure and texture in Ni49.4Ti 38.6Hf12 shape memory alloy during hot rolling, Intermetallics. 42 (**2013**) 1–8. https://doi.org/10.1016/j.intermet.2013.04.009.

[96] E. Acar, H.E. Karaca, H. Tobe, R.D. Noebe, Y.I. Chumlyakov, Characterization of the shape memory properties of a Ni 45.3Ti39.7Hf10Pd5 alloy, J. Alloys Compd. 578 (**2013**) 297–302. https://doi.org/10.1016/j.jallcom.2013.06.030.

[97] H.E. Karaca, E. Acar, B. Basaran, R.D. Noebe, Y.I. Chumlyakov, Superelastic response and damping capacity of ultrahigh-strength [1 1 1]-oriented NiTiHfPd single crystals, Scr. Mater. 67 (**2012**) 447–450. https://doi.org/10.1016/j.scriptamat.2012.05.044.

[98] X.L. Meng, W. Cai, K.T. Lau, L.C. Zhao, L.M. Zhou, Phase transformation and microstructure of quaternary TiNiHfCu high temperature shape memory alloys, Intermetallics. 13 (**2005**) 197–201.

https://doi.org/10.1016/j.intermet.2004.07.044.

[99] S.F. Hsieh, S.K. Wu, Martensitic transformation of Ti50.5-XNi49.5ZrX/2Hfx/2(X=0-20 at.%) shape memory alloys, Mater. Sci. Forum. 45 (**2000**) 143–152.

[100] D. Canadinc, W. Trehern, H. Ozcan, C. Hayrettin, O. Karakoc, I. Karaman, F. Sun, Z. Chaudhry, On the deformation response and cyclic stability of Ni50Ti35Hf15 high temperature shape memory alloy wires, Scr. Mater. 135 (**2017**) 92–96. https://doi.org/10.1016/j.scriptamat.2017.03.025.

[101] C.C. Wojcik, Properties and heat treatment of high transition temperature Ni-Ti-Hf alloys, J. Mater. Eng. Perform. 18 (**2009**) 511–516. https://doi.org/10.1007/s11665-009-9357-2.

[102] M. Belbasi, M.T. Salehi, Influence of chemical composition and melting process on hot rolling of nitihf shape memory alloy, J. Mater. Eng. Perform. 23 (**2014**) 2368–2372. https://doi.org/10.1007/s11665-014-1006-8.

[103] H.O. Tugrul, H.H. Saygili, M.S. Velipasaoglu, B. Kockar, Comparison of the transformation behavior of cold rolling with aging and hot extrusion with aging processed Ni50.3Ti29.7Hf20 high temperature shape memory alloy, Smart Mater. Struct. 28 (**2019**) 105029. https://doi.org/10.1088/1361-665X/ab39f3.

[104] X.L. Meng, W. Cai, Y.F. Zheng, L.C. Zhao, Phase transformation and precipitation in aged Ti-Ni-Hf high-temperature shape memory alloys, Mater. Sci. Eng. A. 438–440 (**2006**) 666–670. https://doi.org/10.1016/j.msea.2006.01.099.

[105] D.R. Coughlin, P.J. Phillips, G.S. Bigelow, A. Garg, R.D. Noebe, M.J. Mills, Characterization of the microstructure and mechanical properties of a 50.3Ni-29.7Ti-20Hf shape memory alloy, Scr. Mater. 67 (**2012**) 112–115. https://doi.org/10.1016/j.scriptamat.2012.03.036.

[106] S.M. Saghaian, H.E. Karaca, H. Tobe, A.S. Turabi, S. Saedi, S.E. Saghaian, Y.I. Chumlyakov, R.D. Noebe, High strength NiTiHf shape memory alloys with tailorable properties, Acta Mater. 134 (**2017**) 211–220. https://doi.org/10.1016/j.actamat.2017.05.065.

[107] B.C. Hornbuckle, T.T. Sasaki, G.S. Bigelow, R.D. Noebe, M.L. Weaver, G.B. Thompson, Structure-property relationships in a precipitation strengthened Ni-29.7Ti-20Hf (at%) shape memory alloy, Mater. Sci. Eng. A. 637 (**2015**) 63–69. https://doi.org/10.1016/j.msea.2015.03.123.

[108] X.L. Meng, W. Cai, Y.D. Fu, Q.F. Li, J.X. Zhang, L.C. Zhao, Shape-memory behaviors in an aged Ni-rich TiNiHf high temperature shape-memory alloy, Intermetallics. 16 (**2008**) 698–705. https://doi.org/10.1016/j.intermet.2008.02.005.

[109] S.M. Saghaian, H.E. Karaca, H. Tobe, J. Pons, R. Santamarta, Y.I. Chumlyakov, R.D. Noebe, Effects of Ni content on the shape memory properties and microstructure of Ni-rich NiTi-20Hf alloys, Smart Mater. Struct. 25 (**2016**) 1–11. https://doi.org/10.1088/0964-1726/25/9/095029.

[110] X.L. Meng, W. Cai, F. Chen, L.C. Zhao, Effect of aging on martensitic transformation and microstructure in Ni-rich TiNiHf shape memory alloy, Scr. Mater. 54 (**2006**) 1599–1604. https://doi.org/10.1016/j.scriptamat.2006.01.017.

[111] F. Yang, D.R. Coughlin, P.J. Phillips, L. Yang, A. Devaraj, L. Kovarik, R.D. Noebe, M.J. Mills, Structure analysis of a precipitate phase in an Ni-rich high-temperature NiTiHf shape memory alloy, Acta Mater. 61 (**2013**) 3335–3346. https://doi.org/10.1016/j.actamat.2013.02.023.

[112] S.M. Saghaian, H.E. Karaca, M. Souri, A.S. Turabi, R.D. Noebe, Tensile shape memory behavior of Ni50.3Ti29.7Hf20 high temperature shape memory alloys, Mater. Des. 101 (**2016**) 340–345. https://doi.org/10.1016/j.matdes.2016.03.163.

[113] O. Karakoc, A. Demblon, R.W. Wheeler, D.C. Lagoudas, I. Karaman, Effects of testing parameters on the fatigue performance nitihf high temperature shape memory alloys, AIAA Scitech 2019 Forum. 175 (**2019**) 107–120. https://doi.org/10.2514/6.2019-0416.

[114] O. Karakoc, C. Hayrettin, A. Evirgen, R. Santamarta, D. Canadinc, R.W. Wheeler, S.J. Wang, D.C. Lagoudas, I. Karaman, Role of microstructure on the actuation fatigue performance of Ni-Rich NiTiHf high temperature shape memory alloys, Acta Mater. 175 (**2019**) 107–120. https://doi.org/10.1016/j.actamat.2019.05.051.

[115] O. Karakoc, K.C. Atli, O. Benafan, R.D. Noebe, I. Karaman, Actuation fatigue performance of NiTiZr and comparison to NiTiHf high temperature shape memory alloys, Mater. Sci. Eng. A. 829 (**2022**) 142154. https://doi.org/10.1016/j.msea.2021.

[116] M. Ekiciler, B. Kockar, Crack growth behavior during actuation cycling of hot extruded and annealed Ni50Ti30Hf20 high temperature shape memory alloys, Smart Mater. Struct. 31 (**2022**) 1–12.

[117] P.C.C. Monteiro, L.L. Silva, T.A. Netto, M.A. Savi, Experimental investigation of the influence of the heating rate in an SMA actuator performance, Sensors Actuators, A Phys. 199 (**2013**) 254–259. https://doi.org/10.1016/j.sna.2013.05.016.

[118] Y.Q. Zhang, S.Y. Jiang, Y.N. Zhao, M. Tang, Influence of cooling rate on phase transformation and microstructure of Ti-50.9%Ni shape memory alloy, Trans. Nonferrous Met. Soc. China (English Ed. 22 (**2012**) 2685–2690. https://doi.org/10.1016/S1003-6326(11)61518-5.

[119] Y. Motemani, M. Nili-Ahmadabadi, M.J. Tan, M. Bornapour, S. Rayagan, Effect

of cooling rate on the phase transformation behavior and mechanical properties of Ni-rich NiTi shape memory alloy, J. Alloys Compd. 469 (**2009**) 164–168. https://doi.org/10.1016/j.jallcom.2008.01.153.

[120] M. Schikorra, L. Donati, L. Tomesani, A.E. Tekkaya, Microstructure analysis of aluminum extrusion: Grain size distribution in AA6060, AA6082 and AA7075 alloys, J. Mech. Sci. Technol. 21 (**2007**) 1445–1451.

[121] H.C. Lin, S.K. Wu, Chou T.S, Kao H.P., The Effects of Cold Rolling on the Martensitic Transformation of an Equiatomic TiNi Alloy, 39 (**1991**) 2069–2080.

[122] Frick C.P., O. A.M., Tyber J., Maksound A.E.M., H.J. Maier, L. Y., K. Gall, Thermal processing of polycrystalline NiTi Shape Memory Alloys, Mater. Sci. Eng. A. 405 (**2005**) 34–49.

[123] D.A. Miller, D.C. Lagoudas, Influence of cold work and heat treatment on the shape memory effect and plastic development of NiTi, Mater. Sci. Eng. A. 308 (**2001**) 161–175. https://doi.org/10.1016/S0921-5093(00)01982-1.

[124] M. Belbasi, M.T. Salehi, S.A.A.A. Mousavi, S.M. Ebrahimi, A study on the mechanical behavior and microstructure of NiTiHf shape memory alloy under hot deformation, Mater. Sci. Eng. A. 560 (**2013**) 96–102. https://doi.org/10.1016/j.msea.2012.09.039.

[125] O. Karakoc, K.C. Atli, A. Evirgen, J. Pons, R. Santamarta, O. Benafan, R.D. Noebe, I. Karaman, Effects of training on the thermomechanical behavior of NiTiHf and NiTiZr high temperature shape memory alloys, Mater. Sci. Eng. A. 794 (**2020**) 139857.

[126] H.H. Saygili, The development of a fatigue test machine to investigate the functional fatigue life of high temperature shape memory alloys and the determination of the functional fatigue life of these alloys, Master's Thesis, Hacettepe University, **2018**.

[127] H.J.M. and Y.C. H. Sehitoglu, R. Hamilton, Hysteresis in NiTi alloys, J.Phys. IV Fr. 115 (**2004**) 3–10.

[128] W.L. Xiao, H.B. Chen, Y. Yin, Effects of surface roughness on the fatigue life of alloy steel, Key Eng. Mater. 525–526 (**2013**) 417–420.

7. APPENDIX

APPENDIX 1 – Publications

E. Akin, O. Akgul, H.O. Tugrul, G. Dugan, B. Kockar, Investigating the effect of hot extrusion and annealing to the functional fatigue behavior of Ni50Ti30Hf20high temperature shape memory alloy, Smart Mater. Struct. 30 (2021). https://doi.org/10.1088/1361-665X/ac1bee.

APPENDIX 2 – Conference Presentations

Erhan Akın, Benat Kockar. “Functional fatigue behavior of hot extruded and annealed $Ni_{50}Ti_{30}Hf_{20}$ high temperature shape memory alloy” *12th European Symposium on Martensitic Transformations in ANKARA/TURKEY (ESOMAT’22), September 5-9 2022.*